Photoacoustic Remote Sensing (PARS) Microscopy

by

Kevan Lewis Bell

A thesis submitted in partial fulfillment of the requirements for the degree of

Doctor of Philosophy
in
Biomedical Engineering

Department of Electrical and Computer Engineering

University of Alberta

Abstract

Photoacoustic imaging systems have proven to be power tools for visualizing optical absorption contrast within highly turbid media such as biological tissues. They provide high chromophore specificity *in vivo* due to the dramatic optical absorption contrast which exists between biological targets. This allows for non-ionizing label-free visualization of a wide range of targets such as hemoglobin, melanin, DNA, RNA, lipids, and cytochrome to name a few. Moreover, these devices can utilize exogenous labelling to further extend contrast and functional imaging capabilities. However, conventional photoacoustic techniques require acoustic coupling to the sample to read out generated acoustic signals. This contact can be highly undesirable for a variety of imaging targets, particularly *in situ*. This motivated the created of a non-contact photoacoustic modality which is the focus of this dissertation. This novel modality which is known as photoacoustic remote sensing (PARS) microscopy, is a cellular-scale photoacoustic imaging technique which is capable of providing optical diffraction-limited resolutions while maintaining centimeter-scale working distance from the sample. Given that the approach is in its infancy, work here focuses on developing physical models which describe the underlying physical processes behind the non-contact

detection. These models aim to describe the time-evolution of the PARS detection process for simple geometries known to be relevant to optics and photoacoustics. As well, new PARS-based embodiments are described which use these models to further extend system capabilities in terms of acquisition rates and axial resolution performance at deeper penetration depths in scattering tissue. Finally, experimental work into a second generation architecture for PARS is investigated which focuses on fiber tetherable optics, and real-time multiplex imaging. The capabilities of the PARS technique to operate within challenging biological samples makes it an exciting area of research which may provide an entire new field of imaging devices to the research and clinical fields.

Preface

Some components of this thesis arise from collaborative efforts between the author and other parties as summarized below. Chapter 3 was published as [1] (K. L. Bell, P. Hajireza, W. Shi, and R. J. Zemp, "Temporal evolution of low-coherence reflectrometry signals in photoacoustic remote sensing microscopy," Applied optics, vol. 56, no. 18, pp. 5172-5181, 2017), and Chapter 4 was published as [2] (K. Bell, P. Hajireza, and R. Zemp, "Scattering cross-sectional modulation in photoacoustic remote sensing microscopy," Optics letters, vol. 43, no. 1, pp. 146-149, 2018). For both of these works, I was responsible for developing analytical models for representing the time-evolution of underlying physical processes behind PARS detection. This built upon work presented in the first report of the device [3]. I was also responsible for conducting experimental work related to these publications and was the primary authour of the manuscript. Chapter 5 is currently under submission to Optics Letters [Submitted April 3, 20129]. I was responsible for co-designing the optical system, proposing and testing the new spectral unmixing process and algorithm, conducting experiments, coding of data acquisition, processing, and image reconstruction, and was the primary authour of the manuscript. Chapter 6 was published as [4] (K. L. Bell, P. Hajireza, and R. J. Zemp, "Coherence-gated photoacoustic remote sensing microscopy," Optics express, vol. 26, no. 18, pp. 23 689-23 704, 2018). I was responsible for developing analytical models for representing the new coherence-gated PARS detection process, testing these models with simulations and was the primary authour of the manuscript.

The research project, of which this thesis is a part, received research

ethics approval from the University of Alberta Research Ethics Board, AUP00001170, Molecular Imaging with Photoacoustics and Ultrasound.

Acknowledgments

The authour would like to acknowledge the help from his colleagues and collaborators which facilitated this and related work. These include but are not limited to Parsin Haji Reza, Wei Shi, Robert Paproski, Logan Snider, Nathaniel Haven, and Pradyumna Kedarisetti. As well, the authour would like to acknowledge the help and mentorship he has received from his graduate supervisor Roger Zemp, and other mentors including but not limited to Abdulhakem Elezzabi and Neda Nazemifard. The authour would also like to acknowledge student funding support received through his undergraduate and graduate studies from the natural science and engineering research council of Canada, Alberta innovates, and the University of Alberta. Finally, the authour would like to acknowledge funding sources for projects: Natural Sciences and Engineering Research Council of Canada (NSERC) (355544-2008, 375340-2009, RGPIN-2018-05788, STPGP 39644, STPGP 494293-16); Terry Fox Foundation (01237, 019240); Canadian Cancer Society (CCS) (2011-700718); Alberta Innovates—Health Solutions (AIHS) (201201154); Alberta Cancer Board (23728); Leaders Opportunity Fund of the Canada Foundation for Innovation (CFI) (18472); Alberta Advanced Education & Technology, Ministry of Advanced Education and Technology (AET) (URSI09007SEG); and CIHR (PS 153067).

Contents

List of Figures

List of Symbols

A_e	Specific optical absorption
a	Scattering particle radius
a_m	Mie theory scattering coefficient
b_m	Mie theory scattering coefficient
$b(z)$	A-scan envelope-detected difference signal (Ch. 6)
c_m	Multi-layer theory scattering coefficient
C_p	Specific heat capacity at constant pressure
C_v	Specific heat capacity at constant volume
c	Speed of light in vacuum
d_c	Characteristics size of heated region
$\mathbf{D}_{m-1}^{-}\mathbf{D}_{m}^{+}$	The transmission-reflection matrix between regions $m-1$, and m
d_m	Multi-layer theory scattering coefficient
$E_s(\nu, t)$	Reflected complex electric field spectrum (Ch. 6)
E_{s_0}	Incident electric field amplitude on the sample (Ch. 6)
$E_r(\nu, t)$	Reference arm complex electric field spectrum (Ch. 6)
E_R	Reflected the electric field amplitude from reference arm (Ch. 6)
$H(\mathbf{r}, t)$	Heating function
$H(\mathbf{x}, t)$	Heating function (Ch. 6)
$\mathcal{H}(z)$	Heaviside step function
$h_{E,int}(\mathbf{x}, \mathbf{x'})$	shifted normalized electric field of a focused interrogation beam (Ch. 6)

$H^n_{i,j,k}$	Discreet heating function at location i, j, k and time n (Ch. 6)
$h_{OCT}(\mathbf{x}, \mathbf{x'})$	OCT point-spread function (Ch. 6)
$h_{OCT,LSI}(\mathbf{x})$	Linear shift-invariant approximation of the OCT point-spread function (Ch. 6)
$h_{PARS,int}(\mathbf{x}, \mathbf{x'})$	PARS point-spread function (Ch. 6)
ΔI	Change in optical intensity
$I_{ex}(\mathbf{x}, t)$	Intensity distribution describing the excitation (Ch. 6)
$\Delta I(\nu, t)$	Reflectivity spectrum (Ch. 6)
k	Wavenuber
k_m	Mean wavenumber in region m
L_m	Thickness of region m
ℓ_s	Scattering depth variable (Ch. 6)
$\Delta\ell_r$	Reference pathlength (Ch. 6)
$\bar{n}^*(z, t)$	Approximate equivalent linear refractive index profile(Ch. 6)
$n_0(\mathbf{r})$	Static refractive index profile (Ch. 3)
$n_0(\mathbf{x})$	Static refractive index profile (Ch. 6)
n_b	Refractive index of background surrounding optical scatterer
n_m	Refractive index of medium m
δn_m	Perturbation of the refractive index in medium m
n_s	Refractive index of optical scatterer
NA	Numerical aperture
$p(\mathbf{r}, t)$	Pressure field
$p(\mathbf{x}, t)$	Pressure field (Ch. 6)
p_0	Initial pressure
$p_0(\mathbf{r})$	Initial pressure distribution
$p^n_{i,j,k}$	Discreet pressure at location i, j, k and time n (Ch. 6)
$\mathbf{P}_m$	Optical propagation matrix through medium m
$R(z)$	Radius of curvature of the wavefront (Ch. 6)
R'	Perturbed planar intensity reflectivity

$r_{m-1,m}$	Fresnel amplitude reflection coefficient between regions $m-1$, and m
$r_s(\ell_s, t)$	A SD-OCT reflectivity envelope in depth (Ch. 6)
R_s	Static planar intensity reflectivity
R_{zz}	Axial autocorrelation function (Ch. 6)
$\hat{r}_{s,i}(\ell_s)$	Stationary reflectivity distribution (Ch. 6)
ΔR	Intensity reflectivity modulation
Δr_I	Pertubation in the intensity reflection coeffient (Ch. 6)
$S_{OCT}(\mathbf{x})$	OCT signal distribution (Ch. 6)
$S_{OCT,LSI}(\mathbf{x})$	Linear shift-invariant approximation of the OCT signal distribution (Ch. 6)
$S_{PARS}(\mathbf{x})$	PARS signal distribution (Ch. **??**)
t	time variable
$\mathbf{T}$	Optical transfer matrix
$t_{m-1,m}$	Fresnel amplitude transmission coefficient between regions $m-1$, and m
v_s	Speed of sound
$w(z)$	Depth-dependent beam waist (Ch. 6)
x	Size parameter
z_f	Focal depth (Ch. 6)
z_R	Rayleigh (Ch. 6)
$\mathbf{x}$	Spacial coordinate vector (Ch. 6)
α	Weiner deconvolution filter parameter
α_{th}	Thermal diffusivity
β	Thermal coefficient of volume expansion
Γ	Grüneisen parameter
ϵ	Elasto-optic coefficient
η_{th}	Thermal conversion efficiency
κ	Isothermal compressibility
$\phi(\mathrm{x})$	Local phase (Ch. 6)
$\Phi(\mathbf{r}, t)$	Fluence rate distribution
$\Phi(\mathbf{x}, t)$	Fluence rate distribution (Ch. 6)
ϕ_0	Excitation focal fluence

λ	Optical wavelength
$\mu_{ex}(\mathbf{r})$	Optical absorption of the excitation wavelength
ν	Optical frequency (Ch. 3, 4, 6)
$\rho^2(\mathbf{x}, \mathbf{x'})$	Square of the radial spatial coordinate (Ch. 6)
ρ_m	Mass density
$\sigma_{s,ML}$	Scattering cross-section for multi-layer scattering theory
$\sigma_{s,Mie}$	Scattering cross-section for Mie scattering theory
$\sigma_{s,Ray.}$	Scattering cross-section for Rayleigh scattering theory
$\Delta\sigma_s$	Change in scattering cross-section
$\psi(z)$	Guoy phase (Ch. 6)
$\Psi(z)$	Depth regions of equal phase (Ch. 6)
∇	Gradient operator
∇^2	Laplacian

Chapter 1

Introduction

Photoacoustic imaging techniques provide access to optical absorption contrast which is useful for both biological targets and a wide variety of non-destructive testing applications. The optical absorption spectrum of a sample encodes molecular information which can be leveraged for both structural recovery and functional information mapping. Much of the community focus to date has revolved around biological targets which take advantage of photoacoustics' excellent contrast specificity and its ability to overcome the optical diffusion limit through acoustic signal recovery. Popular endogenous targets have included DNA for visualization of cell nuclei [18, 19] and hemoglobin for functional and structural recovery of blood vessels [6]. Other strong endogenous chromophores have been investigated such as melanin [20], cytochrome [21] and lipids [22] to name a few. To complement these targets, a range of exogenous targets and chromophores such as gold nanoparticles/nanorods [23] and dyes [24] have also been investigated. As well, conventional photoacoustics provide a highly scalable platform capable of sub-millimeter lateral resolutions centimeters down in scattering tissue, and optical-diffraction-limited resolutions at superficial depths.

However, conventional photoacoustic techniques bring with them a major drawback to their implementation. Since they require acoustic coupling to the sample to read generated photoacoustic signals, physical contact is required through an acoustic coupling medium such as water or ultrasound

gel. This leads to a variety of potential complications in both logistical implementation of co-aligned acousto-optic beam paths, and complications with *in situ* targets where the physical contact may be highly impractical. These limitations motivate the development of a non-contact photoacoustic modality. Although several approaches have been examined, and will be covered in the following section, the first method which approaches the capabilities of contact-based devices comes from photoacoustic remote sensing microscopy (PARS) [3].

PARS replaces the acoustic detection with a secondary probe beam which senses photoacoustic signals. The underlying mechanism for this device is a primary focus of this thesis and will be heavily discussed in the following chapters. In brief, a nanosecond excitation pulse is absorbed by a target chromophore which creates a small but sudden rise in temperature and, in turn, a large pressure rise. This thermo-elastic expansion gives rise to photoacoustic initial pressure and is common to all photoacoustic techniques. With PARS, the pressures are detected directly through their elasto-optic modulation of the local optical properties. This is accomplished by focusing a secondary probe beam at the excitation spot, the reflections of which from the excitation location are rapidly modulated due to the build up of pressures. As is discussed in the first report [3] the back-reflected intensity resulting from these modulations is relatively linear with the optical absorbance of the sample, providing optical absorption contrast. Moreover, this linear relationship opens the potential for linear multiplex imaging as has been used in photoacoustics for mapping of blood oxygen saturation *in vivo* for example.

Early investigations into this method also suggested that PARS could provide similar performance in terms of sensitivity to conventional optical-resolution photoacoustic systems, while improving in other areas of performance. These efforts demonstrated high lateral resolutions approaching the optical diffraction limit. Unlike conventional optical-resolution systems which require bulky acousto-optic beam splitters for reflection-mode operations, the all-optical nature of PARS has permitted the use of conventional focusing optics with high numerical apertures. As is demonstrated in more

recent PARS publications [25] this has indeed approached the aperture-defined diffraction limit (690 nm in this example). Another interesting consequence of the architecture was also investigated in [25]. Although the excitation wavelength must be selected with consideration given to the desired target chromophores, the detection wavelength must simply be partially scattered by the target region. This leaves the interogation wavelength selection substantially more open. In particular, if maximizing penetration depth is of priority, the detection wavelength can be chosen as a deeply-penetrating short-wave infrared. In tissues this may mean that the transport mean-free path is 5 times that of the excitation. Very much akin to acoustic-resolution photoacoustic modalities which allow for defocusing of the excitation at the target region, PARS can permit the same degradation with the recovered resolution still defined by optical diffraction (that of the detection) rather than acoustic diffraction (from generated photoacoustic signals). These capabilities have already demonstrated *in vivo* visualization of red blood cells [3].

These capabilities lay the groundwork for an impressive new field of research surrounding the PARS mechanism and related imaging techniques. The high lateral resolution is appropriate for recovering cellular-scale structural information. The potential for linear multiplex imaging has demonstrated to be efficacious for *in vivo* functional mapping of blood oxygen saturation [25]. The ability to maintain cellular-scale resolution deep in tissue may permit the study of microbiology in its endogenous state. These technical capabilities are well complimented by the vast variety of endogenous contrast provided in biological systems which have already been well described in literature for conventional photoacoustic devices. However, at the start of this thesis work, very little was well understood regarding the underlying PARS mechanism. The first report only suggested a simple two-state explanation of the mechanism which was sufficient in providing an intuitive image of the underlying physics but consisted of highly idealized arguments which required further investigation.

This brings about the first focus of this manuscript, to provide an improved physical model of the PARS mechanism. This involved expanding the

one-dimensional two-state model to a time-dependent evolution in several geometries. Next followed improvements in the architecture of the initial apparatus into a fiber tetherable modality capable of real-time functional imaging. Finally, a new modality is investigated where coherence gating techniques common to optical coherence tomorography (OCT) are added to improve potential axial performance and volumetric imaging speeds over the original implementations.

1.1 Summary of Contributions

The contributions of the authour with regards to peer-reviewed publications are as follows:

- The first report of the PARS mechanism and the first report of a PARS imaging apparatus [3] (P. Hajireza, W. Shi, K. Bell, R. J. Paproski, and R. J. Zemp, "Noninterferometric photoacoustic remote sensing microscopy," Light: Science & Applications, vol. 6, no. 6, p. e16278, 2017). The author's contributions included work on analytical model, producing and testing analytical approximations, coding experimental acquisitions and reconstructions, conducting experiments, analyzing data and authoring the manuscript.

- Work relating to the deep imaging capabilities of a PARS microscope and the first report of functional imaging with PARS in mapping *in vivo* blood oxygen saturation [25] (P. H. Reza, K. Bell, W. Shi, J. Shapiro, and R. J. Zemp, "Deep noncontact photoacoustic initial pressure imaging," Optica, vol. 5, no. 7, pp. 814-820, 2018). The author's contributions included coding experimental acquisitions and reconstructions, conducting experiments, analyzing data and authoring the manuscript.

- The first work dedicated to the time-evolution of the PARS mechanism relating to the PARS mechanism in one dimension interacting with an absorbing planar medium, with the first theoretical description of PARS signal linearity with the optical absorption [1] (K. L.

Bell, P. Hajireza, W. Shi, and R. J. Zemp, "Temporal evolution of low-coherence re ectrometry signals in photoacoustic remote sensing microscopy," Applied optics, vol. 56, no. 18, pp. 5172-5181, 2017). The author's contributions included design of analytical model, producing and testing analytical approximations, coding and performing simulations, designing experiments, conducting experiments, and authoring the manuscript.

- The second work dedicated to the time-evolution fo the PARS mechanism relating to the PARS mechanism interacting with a spherical absorbing scattering particle. This also provided a physical model for the non-linear signal behavior observed in sub-wavelength scattering particles [2] (K. Bell, P. Hajireza, and R. Zemp, "Scattering cross-sectional modulation in photoacoustic remote sensing microscopy," Optics letters, vol. 43, no. 1, pp. 146-149, 2018). The author's contributions included design of analytical model, producing and testing analytical approximations, coding and performing simulations, designing experiments, conducting experiments, and authoring the manuscript.

- An investigation into a potential imaging modality which uses the PARS mechanism to provide optical absorption contrast while implementing coherence gating techniques used in optical coherence tomography to potentially improve dpeth resolution performance and improve volumetric imaging rates [4] (K. L. Bell, P. Hajireza, and R. J. Zemp, "Coherence-gated photoacoustic remote sensing microscopy," Optics express, vol. 26, no. 18, pp. 23 689-23 704, 2018). The author's contributions included design of analytical model, producing and testing analytical approximations, coding and performing simulations, and authoring the manuscript.

- Experimental work on improving upon the original PARS architecture. This included producing a fiber-teatherable imaging head and implementing a real-time functional imaging capability which was demonstrated *in vivo* "in submission". The author's contributions included

design of analytical model, producing and testing analytical approximations, coding and performing simulations, and authoring the manuscript.

The authour has also been involved in the following conference presentations/proceedings

- Initial report of discovery of a non-contact photoacoustic modality prior to determination of physical mechanism [26] (P. H. Reza, K. Bell, W. Shi, and R. J. Zemp, "Multi-scale photoacoustic remote sensing (pars)(conference presentation)," in Photons Plus Ultrasound: Imaging and Sensing 2016, vol. 9708. International Society for Optics and Photonics, 2016, p. 97082F). The author's contributions included coding experimental acquisitions and reconstructions.

- Second report of the discovery now with knowledge of the underlying mechanism. Further capabilities of the modality such as functional imaging is shown [27] (P. H. HajiReza, K. L. Bell, W. Shi, and R. J. Zemp, "Noninterferometric deep optical resolution photoacoustic remote sensing microscopy (conference presentation)," in Photons Plus Ultrasound: Imaging and Sensing 2017, vol. 10064. International Society for Optics and Photonics, 2017, p. 1006420). The author's contributions included coding experimental acquisitions and reconstructions, conducting experiments and analyzing data.

- Conference talk regarding the time-evolution of the PARS signals in a simple one-dimensional geometry. [28] (K. L. Bell, P. H. Reza, W. Shi, and R. J. Zemp, "Temporal evolution of low-coherence reflectometry signals in photoacoustic remote sensing microscopy (conference presentation)," in Photons Plus Ultrasound: Imaging and Sensing 2017, vol. 10064. International Society for Optics and Photonics, 2017, p. 1006422). The author's contributions included design of analytical model, producing and testing analytical approximations, coding and performing simulations.

- Conference talk regarding the time-evolution of the PARS signals for a simple spherical scattering absorbing particle [29](K. L. Bell, P. H.

Reza, , and R. J. Zemp, "Spherical scatterer cross section modulation in photoacoustic remote sensing microscopy (conference presentation)," in European Conference on Biomedical Optics, 2017). The author's contributions included design of analytical model, producing and testing analytical approximations, coding and performing simulations.

- Experimental investigation into testing the acquisition rate limits of a PARS microscope. This work also presented an analogue circuit for processing PARS signals which significantly reduced bandwidth and computational load [30] (L. Snider, K. Bell, P. Reza, and R. J. Zemp, "Toward wide-field highspeed photoacoustic remote sensing microscopy," in Photons Plus Ultrasound: Imaging and Sensing 2018, vol. 10494. International Society for Optics and Photonics, 2018, p. 1049423). The author's contributions included coding experimental acquisitions and reconstructions, conducting experiments, analyzing data and authoring the proceeding.

- Conference talk regarding the newly thought of coherence-gated photoacoustic remote sensing (CG-PARS) technique. [31] (K. L. Bell, P. Hajireza, and R. Zemp, "Coherence-gated photoacoustic remote sensing microscopy (conference presentation)," in Photons Plus Ultrasound: Imaging and Sensing 2018, vol. 10494. International Society for Optics and Photonics, 2018, p. 1049422). The author's contributions included design of analytical model, producing and testing analytical approximations, coding and performing simulations.

- Conference talk regarding the first report of an ultraviolet-excitation PARS microscope capable of visualizing DNA contrast in cells and tissue sample [32] (N. J. Haven, K. L. Bell, P. Kedarisetti, P. H. Reza, J. D. Lewis, and R. J. Zemp, "Label-free non-contact imaging of cell nuclei using ultraviolet photoacoustic remote sensing microscopy (conference presentation)," in Photons Plus Ultrasound: Imaging and Sensing 2019, vol. 10878. International Society for Optics and Photonics,

2019, p.108781X). The author's contributions included coding experimental acquisitions and reconstructions, conducting experiments and analyzing data.

1.2 Organization of Thesis

This thesis is organized as follows:

- Chapter 2: A literature and background review for the photoacoustic field and relevant non-contact, and all-optical photoacoustic techniques. As well, a brief background is included regarding optical coherence tomography has the information will be relevant to topics discussed in Chapter 6.

- Chapter 3: A simple one-dimensional planar model of the PARS mechanism. Particular focus is given towards the time-evolution of the detected signals, and relevant system parameters. Appropriate approximations are presented which significantly reduce computational time in this simulation.

- Chapter 4: A simple three-dimensional model of the PARS mechanism for a scattering and absorbing spherical particle. Again, focus is given to the time-evolution of the scattering cross-section of the particle. Approximations are constructed and found to be valid within certain sample parameter regions, however some of the more complex non-linear behaviour requires the use of the more complex model. This non-linearity seen in sub-wavelength particles is corroborated with experiments.

- Chapter 5: A second-generation PARS architecture is investigated looking at producing a device with has a fiber-tetherable scan head, and is capable of real-time functional imaging. Phantom and *in vivo* experiments are conducted and found to be reasonably accurate.

- Chapter 6: A new PARS-base modality is considered which takes ideas from optical coherence tomography. By integrating low-coherence in-

terferometry, this new coherence-gated PARS (CG-PARS) is simulated to examine potential system considerations and feasibility of the technique.

- Chapter 7: A concluding chapter summarizing the findings of the thesis topics.

Chapter 2

Background and Literature Review

Optical absorption presents a powerful imaging contrast in clinical, biological and industrial imaging. Photoacoustic (PA) techniques represent a promising family of modalities for observing this contrast. These systems use the thermo-elastic effect, commonly known in the field as simply the photoacoustic effect, first noted by Alexander Graham Bell in 1880 [33]. Here Bell remarked that an audible sound was made when sunlight was periodically introduced to a solid, and related this audible cue to the optical absorption of the target. The effect is attributed to a rapid local heating in the medium which causes rapid expansion. This rapid expansion then in turn develops into an outward propagating acoustic signal. In photoacoustics, this rapid heating is produced through the use of a short pulsed excitation beam with pulse widths commonly in the nanosecond regime. As well, rather than audible sounds, generated acoustic signals generally fall within the ultrasound regime and are read out using ultrasound transducers acoustically coupled to the sample. Since the acoustic signal strength is directly proportional to the heating effect, it is also proportional to the amount of absorbed optical energy. This means that for a given excitation fluence, and within a reasonable pulse energy range, the acoustic signal strength is linear to the optical absorption at the excitation wavelength. To generalize,

an optical absorber with large absorbance will produce a greater signal than one with little to no absorbance meaning that the technique provides optical absorption contrast.

Previous optical absorption imaging techniques relied on monitoring the transmission of photons. Well-known examples would include X-ray imaging, or transmission mode microscopies which illuminate the sample from the opposite side from the detection. The optical absorption is then inferred by assuming dark regions related to increased photon extinction yielding a negative signal. However, in the case of X-rays, or any optical transmission measurement of optical absorption, the sample is required to be reasonably thin such that photons may pass completely through it, and must provide sufficiently low optical scattering to transmitted photons such that the photon extinction measured is roughly equal to the photon absorption. In the case of photoacoustics, since only the acoustic signals are required for detection a sample does not need to be optically thin and indeed optical absorption detection can even be provided in reflection-mode for acoustically thick samples. Moreover, this technique provides a positive detection signal such that larger optical absorption produces a stronger signal.

In this chapter some general background of PA techniques is presented. This includes a brief overview of the field as a whole, following the current challenges to be faced. This culminates in the development of the first PARS techniques aiming to overcome these challenges, acting as a transmission into the more dense discussion in the following chapters.

Photoacoustic imaging

Optical imaging modalities present a powerful tool set for visualizing molecular contrast by encoding molecular information within the optical scattering and optical absorption spectra. However, for the very same reason that optical wavelengths provide excellent contrast, they are also highly scattering and attenuating within turbid and absorbing media. This problem is especially evident within biological tissues where optical scattering is highly prevalent. This has generally limited optical techniques to either low pene-

tration depths (< 1 mm) such that they operated within the ballistic photon range, or resolution is sacrificed to provide improved depth such as in diffuse optical tomography (> 1 cm) [34]. To fill this gap comes photoacoustic imaging with the aim of improving the penetration depth of optical contrast while maintaining more relevant resolution.

PA modalities fire short optical pulses into the sample where chromophores will absorb the optical energy, converting it to heat and pressure via the photoacoustic effect. This rapid pressure rise produces outward propagating acoustic waves which can be read out at the sample surface. Unlike the photons used for excitation, the acoustic waves suffer negligible attenuation and scattering within the biological tissue. This allows for acoustic focusing to provide resolution beyond the optical diffusion limit. This concept has proven to be quite powerful providing a highly scaleable process by appropriate selection of the optical and acoustic components. Optical focusing enables optical-resolution (< 500 nm) at superficial depths (< 1 mm). At greater depths where optical focusing cannot be maintained acoustic-resolution PA imaging has achieved sub-millimeter resolution (720 μm) down to 7 cm [6].

Endogenous optical-absorption contrast is quite prevalent *in vivo*. By careful selection of excitation wavelengths, photoacoustics have demonstrated label-free visualization of blood [35], lipids [22], DNA [36], melanin (melanoma) [37, 38], and some procedure-related elements such as inserted brachytherapy seeds localization [39] and needle localization [40]. They have been used in longitudinal characterization of tumour vasculature [41], and used in the visualization of breast cancers [42–44] and prostate cancer [6]. Intravascular photoacoustic endoscopy has been used in the characterization of lipid-rich Aortic plaques [45, 46]. Photoacoustics have also been used to perform *in vivo* virtual flow cytometry tracking circulating tumour cells [17, 37].

Sensitivity to optical absorption also enables functional imaging approaches such as spectral unmixing. Here, absorption contrast between multiple chromophore species provides additional information which can enable visualization of relative concentration. One popular target for the technique has been the spectral unmixing of oxy- and deoxyhemoglobin to provide

blood oxygen saturation mapping (Fig. 2.1). This enables quantification of localized oxygen saturation and oxygen metabolism (through the addition of ultrasound flow measurement), both of which are desirable for clinicians to aid in diagnosis and prognosis of areas such as staging of tumours [47], monitoring of wound healing [48], characterizing reperfusion [49], and monitoring brain activity [50]. In addition to endogenous contrasts, exogenous agents may still be added to label desired tissues as with other optical techniques, enabling yet further improved contrast and greater opportunity for signal multiplexing. This opens up a wide range of optical functional imaging capabilities scalable to beyond the optical ballistic regime, while still providing superior resolution performance over competing techniques such as diffuse optical tomography, nuclear emission tomography, and fluorescence molecular tomography.

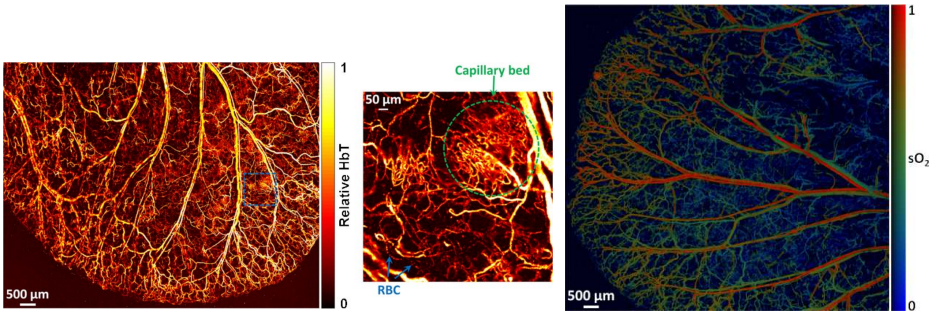

Figure 2.1: (Left) An optical-resolution photoacoustic image of vasculature within a mouse ear with a (Middle) zoomed in section. (Right) Blood oxygenation mapping within a mouse ear [5].

Photoacoustic devices commonly fit into one of three categories which characterizes their respective resolution and penetration depth performance. At superficial depth within the ballistic optical regime where optical focusing can be maintained exists optical-resolution photoacoustic microscopy (OR-PAM). Here the excitation pulses are focused within the sample and the returning acoustic waves are collected via a focused- or unfocused transducer (Fig. 2.1) [5]. Systems are commonly constructed with an acousto-optic beam splitter to combine and separate acoustic and optic signals. To be considered an optical resolution system, the resolution must derive pri-

marily from a focused excitation beam (Fig. 2.2a). Though not required, a co-focused transducer further improves device performance. This provides micron-scale visualizations. The approach is excellent for characterization of microvasculature and cellular-scale phenomenon. By taking advantage of DNA absorption with UV light, UV versions of OR-PAM have even been able to recover cellular structure with sub micron-resolution [36, 51]. This opens up the capability of performing virtual histology which may yet revolutionize clinical oncology practices.

Beyond the ballistic optical regime, a focused transducer is capable of providing resolution despite a multiply scattered excitation pulse. Since resolution is now defined through acoustic focusing, the approach is appropriately named acoustic-resolution photoacoustic microscopy (AR-PAM). Greater penetration depths are achieved with tens of microns lateral resolution. Penetration depth and resolution are primarily determined by the bandwidth of the ultrasound transducer used for detection where the primary limit involves acoustic attenuation which is larger at higher frequencies. For example a low penetration, high-resolution embodiment may provide 44 μm lateral resolution, 28 μm axial resolution at a penetration depth of 4.8 mm using a 50 MHz transducer [52]. In comparison a low-frequency embodiment using a 5 MHz ultrasound transducer has been characterized with 590 μm lateral resolution at a penetration depth of 10.3 mm [7]. These systems commonly feature an unfocused illumination with a focused transducer (Fig. 2.2b)

Finally, for operation within the centimeter penetration depth range a tomographic approach similar to conventional ultrasound is used, commonly known as photoacoustic tomography (PAT). This embodiment is traditionally implemented with an ultrasound transducer array to which a large pulsed excitation source has been added. Unlike the previous two methods, PAT is capable of acquiring full 2D scans (commonly referred to as B-scans) with a single excitation event allowing for rapid frame rates over large regions. In much the same way as it is with ultrasound imaging, the resolution performance of PAT is solely defined by the physical properties of the array such as the width of the array, the size and spacing of the trans-

ducer elements, the number of transducer elements, and the bandwidth of the individual elements. PAT has been demonstrated down to 7 cm penetration depths [6], where now the fundamental limit occurs due to optical absorption. Since the surface optical fluence is limited by ANSI skin exposure standards, this in turn limits the available excitation energy at depth within the sample. PAT devices commonly feature an unfocused illumination along with an ultrasound transducer array such as a linear array (Fig. 2.2c) or a ring array (Fig. 2.2d)

However, there are several issues with conventional PA approaches. One of these comes from the bandwidth available from an individual transducer element which is generally limited away from its central frequency. Another involves the desire for large apertures, which becomes an issue when considering two dimensional arrays in terms of complexity and cost associated with fabrication and the required processing electronics. As well, since transducer arrays are generally opaque (with some exceptions [53]), photoacoustic imaging (PAI) at superficial depths in reflection-mode must deal with the logistics of passing excitation light around the transducers. This has been generally handled in the past by several methods including an acousto-optic beam splitter which can redirect the acoustic waves onto the transducer which has been positioned off to the side [5]. However this approach means that components must be placed in both the optical and acoustic pathways which increases propagation distance and reduces the effective aperture of both the optical focusing objective and the focused transducer. An AR-PAM approach has involved the use of a ring mirror which is used to focus the light around the transducer element [54]. In addition to these issues, it would be desirable to improve upon the bandwidth sensitivity of the detectors. It would also be beneficial if detection could be done in a completely non-contact method as this would greatly increase potential applications for the modality in many situations where acoustic coupling is undesirable or impractical [55–57]. Other forms of acoustic transducers have been investigated to overcome some of these limitations.

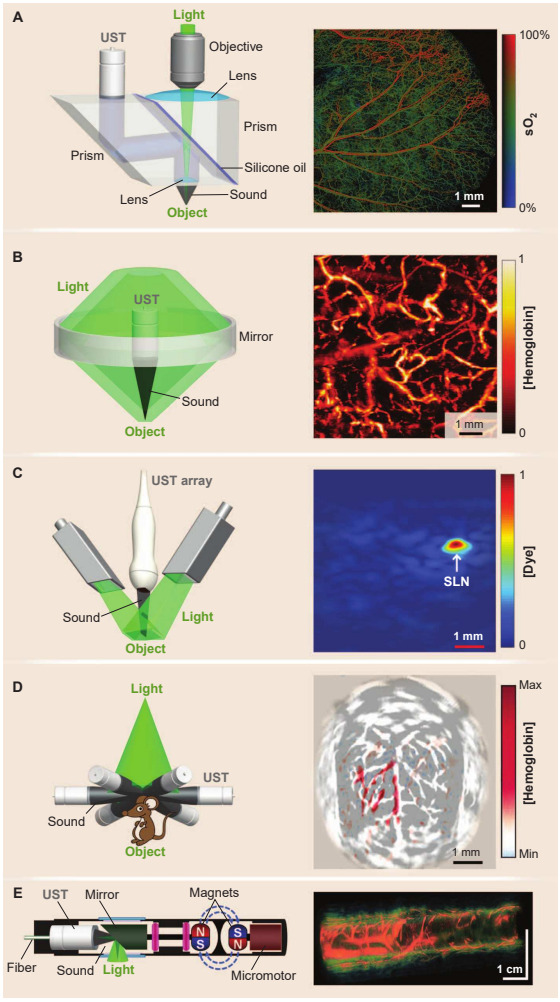

Figure 2.2: Various photoacoustic modality embodiments described in [6]. (a) An OR-PAM device used in [5] which utilizes an acousto-optic beamsplitter, a focused optical excitation and a focused transducer.(b) An AR-PAM device used in [7] which uses an unfocused optical illumination surrounding a focused transducer. (c) A common implementation of a PAT, which uses an unfocused illumination and an ultrasound array. (d) A PAT system which uses a ring-array transducer to provide a full receive aperture. (e) An endoscopic embodiment which features a tight layout.

2.1 Fabry-Pérot Etalons

Surface-coupled optical resonators have proved to be a popular choice for optical detection of ultrasound. Recently, perhaps the most prominent results

have come from Fabry-Pérot etalon structures which have demonstrated exquisite *in vivo* imaging capabilities. This approach is relatively old with publications dating back to at least 1973 [58]. These devices can be used to form either an acoustic-resolution system through the use of a non-focused excitation beam providing deep penetration, or an optical-resolution system by focusing the excitation beam. Detection involves acoustic coupling of an etalon structure with the sample where traveling acoustic waves interact with the resonator which in turn perturbs the intensity of both back-reflected and transmitted light. One benefit of this approach is that it allows for decoupling of the effective aperture size and element size. Unlike a piezoelectric device which would require element dimensions on the order of a few tens of micrometers for proper bandwidth sensitivity at superficial depths, the element size no longer plays such a role, and any desired step size can be generated through appropriate raster scanning of the interrogation light or sample.

The structures have come in the form of both high- and low-finesse embodiments. Here the low-finesse suggests that there are only two primary reflections for interference of the back reflected light where one reflection comes from the backside of the sensing material, and the other comes from the front of the medium which is in acoustic contact with the sample. This technique was particularly popular in the past for fiber based systems [59–61]. For these devices the back reflected intensity can easily be described as the sum of these two electric fields such that

$$I_{tot} = |E_1 + E_2|^2 = |E_1|^2 + |E_2|^2 + 2E_1E_2\cos\phi \tag{2.1}$$

where E_1, E_2 are the electric fields from the front and back of the detection element respectively, and E_2 will be of the form $E_2 = a_2E_1\exp i\phi$ where a_2 represents the relative attenuation and ϕ represents the total phase difference accrued. The modulations in the cosine turn which are detected as an AC signal will encode acoustic information. Two examples of fiber based endoscopic devices which utilize one of these low-finess detectors include [60] which reported an acoustic noise floor of 15 kPa over a 25 MHz bandwidth

and [61] which improved to a 2.3 kPa value. Both of these devices were implemented with a 250 μm fiber providing a small form factor.

For a high-finess system the most simple example consists of a single transparent layer between two highly reflective mirrors, though more complicated structures have been examined. Unlike the low-finess embodiment, this will result in a great deal of accumulated interference interactions in the back reflected beam, which will ideally improve the detector sensitivity. Here the expression for the back reflected intensity from the structure is not quite so straightforward, and requires the use of a more refined approach such as the transfer-matrix method [62]. Regardless of the exact structure used, there exists a reasonable sensitivity to the internal path lengths in the sensing element. By acoustically coupling such a device to the sample, acoustic waves propagating into the etalon can cause subtle changes to the thicknesses and optical properties of the internal layer. This results in subtle changes of the path length and the phase which are then amplified due to the high-finesse structure, shifting the resonant wavelength. This shift can then be related back to the photoacoustic signal.

One issue which becomes immediately apparent when using a high-finess detector is that for backward mode operation the device needs to be optically transparent to the excitation wavelength. This is to allow for the excitation beam to pass through the sensor unimpeded while the probe beam is still required to interact with it. An example of this is demonstrated in [8](Fig. 2.3). Here the authors present a Fabry-Pérot sensor which is optically transparent in the range from 590-1200 nm, and highly reflective in the range from 1500-1650 nm allowing for backward-mode operation. This features a thin polymer (Parylene C) transparent film situated between dielectric dichroic mirrors composed of 8 alternating $\lambda/4$ layers of ZnS and Na_3AIF_6 with a wedged polymethylmethacrylate (PMMA) backing. This device was characterized as having a 38 μm lateral resolution with a 15 μm vertical resolution at superficial depths, with imaging quality maintained down to 5.5 mm in a $\mu_s' = 10cm^{-1}$ scattering liquid. Of the two Parylene thicknesses examined, the 38 μm device proved to be more sensitive with a measured noise equivalent pressure of 0.21 kPa over a 20 MHz measurement bandwidth. Although

this is still quite poor compared with conventional piezoelectric devices in used today, when considering the equivalent element dimensions and detection bandwidth this optical detection is more than two orders of magnitude lower than a piezoelectric receiver. In addition, this optical transparency allows for the sensor to be placed right at the sample surface providing a very large effective aperture for imaging when compared with conventional techniques.

The same group has demonstrated *in vivo* imaging using this Fabry-Pérot sensor in two longitudinal studies [9,41]. In the earlier publication [41] longitudinal imaging of two types of human colorectal tumor xenographs (LS174T, SW1222) from 7-12 days post-inoculation. This allowed for tracking of growth in both the tumors themselves and the development of new blood vessels surrounding them. In the latter work [9], the progress of Tyr-expressing K562 cells were monitored in the flank of a nude mouse over a 26 day period (Fig. 2.4). This capability can be invaluable to pre-clinical applications requiring smaller total sample sizes when investigating animal models. Likewise, in clinical applications this could provide the ability to track the progress of a disease and the effectiveness of treatments further improving prognosis.

These dichroic architectures have also been implemented in front-view and side-view orientations on an optical fiber [63]. The Fabry-Pérot style of sensor seems to be well suited for this, as both style of imaging devices were implemented on 250 μm fibers providing a wide range of potential applications. These fiber implementations have also demonstrated higher sensitivity with reported equivalent noise pressures of around 8 Pa over a 20 MHz bandwidth. The same group later demonstrated *ex vivo* ultrasound imaging using one of these fibers along with a small transducer element both of which were contained inside of a larger 0.84 mm tube [64]. Later, an improved version of the fiber sensor demonstrated small improvements to sensitivity in a smaller package (175 μm outer diameter) [65].

Another approach towards a Fabry-Pérot sensor with tunable optical properties is presented in [66]. Here the etalon structure is constructed from alternating layers of Parylene C with porous nanostructured thin films con-

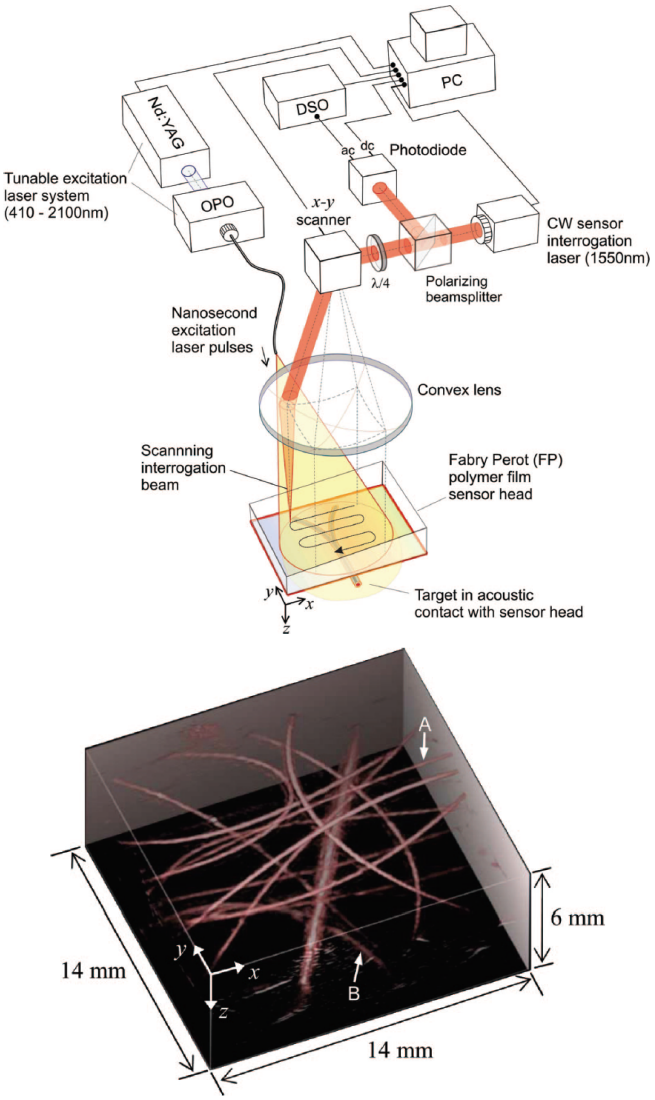

Figure 2.3: (top) A schematic highlighting key components of a simple Fabry-Pérot based PAT system [8]. A nanosecond pulsed excitation is provided by a tunable OPO laser system and diffusely illuminates the target. A second continuous-wave (CW) 1550nm laser provides a probe beam source. The detection path is focused on to a small region of the Fabry-Pérot, and is scanned across the device emulating a 2D array. (Bottom) A phantom image taken from the above device of several dye filled tubes ranging in size from 62 μm to 300 μm in diameter.

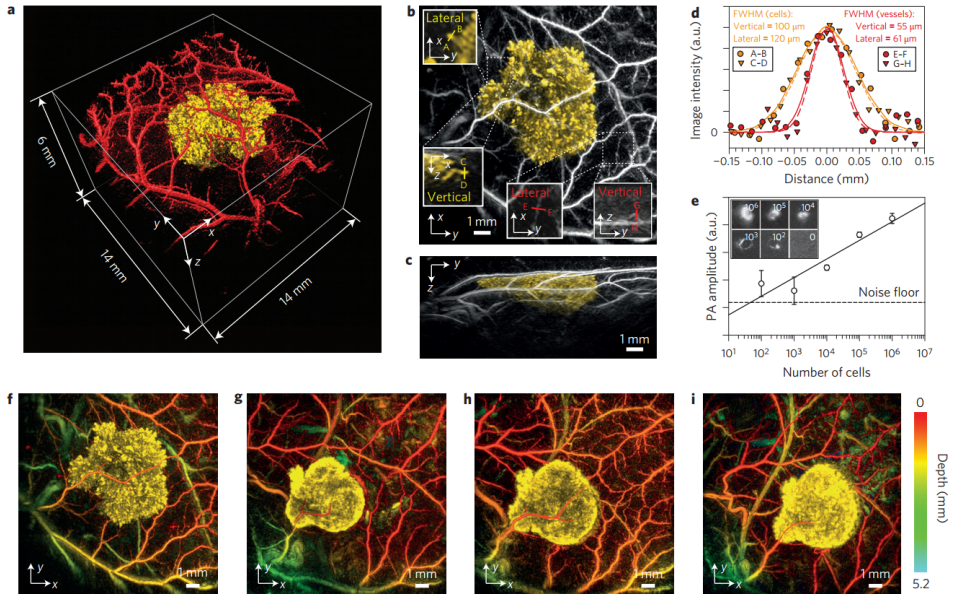

Figure 2.4: (a) A 3D volume representation of Tyr-expressing K562 cells in the flank of a nude mouse, where tumor cells are visible in yellow, with the surrounding vasculature in red. (b-c) Shows an en-face projection, and B-scan of the region shown in (a). (f-l) show en-face projections of the same region at various stages of growth [9].

sisting of TiO_2 deposited through glancing angle deposition (GLAD) (Fig. 2.5). These GLAD layers provided the means of finely tuning the exact optical properties such that a lower wavelength could be used in the pass-band of the device for a more desirable optical absorption contrast. These particular structures were developed such that they were transparent to the 532 nm excitation light and highly reflective to the 1550 nm interrogation beam. These devices also demonstrated superior sensitivity over the dichroic sensors reporting a 80 Pa sensitivity over a 18 MHz bandwidth, and superior lateral resolution of around 7 μm. Later work from the group demonstrated these GLAD structures *in vivo* by imaging the capillary networks of a chorioallantoic membrane (CAM) of a five-day-old chicken embryo model [10](Fig. 2.5).

One common issue facing tomographic imaging involves the so called limited view problem. Since the effective aperture of the detector array can not progress towards infinity, information from the sides of ultrasonic sources cannot be properly reconstructed with a single planar detector. In an attempt to get around this problem while still using linear transducer arrays, groups have tried adding acoustic reflectors at key locations around the sample to effectively create a virtual array with promising results [67,68], however for most real world applications this is far from an ideal solution. Another approach, involves the addition of a second Fabry-Pérot detector array which demonstrated excellent results in phantoms [69] and with *ex vivo* imaging of a mouse head [11, 70](Fig. 2.6) with lateral resolutions of around 40 μm. This approach appears to favor the Fabry-Pérot detector as the addition of a second optical path does not involve the same level of complexity as compared to doubling the total number of transducer elements along with all the extra associated electronics.

2.2 Split ring resonators

Although the Fabry-Pérot optical resonators provide significant advantages such as the ability to create large virtual arrays, other resonators styles have also been examined. One such example are split ring resonators. These

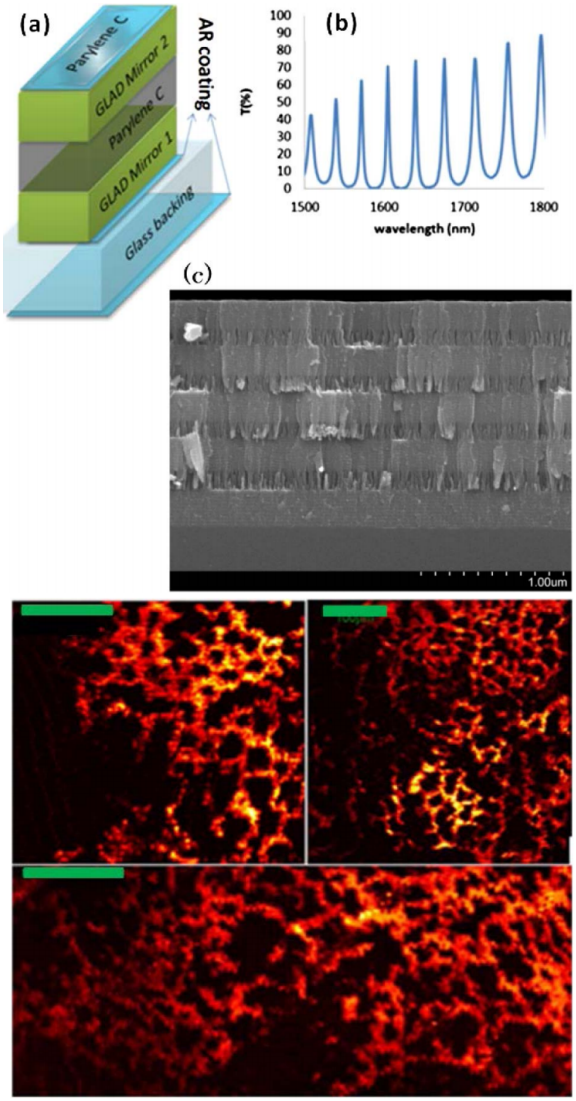

Figure 2.5: (Top)(a) shows a systematic outline for the GLAD Fabry-Pérot sensor, with its respective transmissions spectrum (b), and a representative scanning electron microscope image of the structure (c) where the various layers are clearly visible. (Bottom) *In vivo* images from the CAM of a five-day-old chicken embryo model showing the capillary beds [10]. (scale bars are 100 μm)

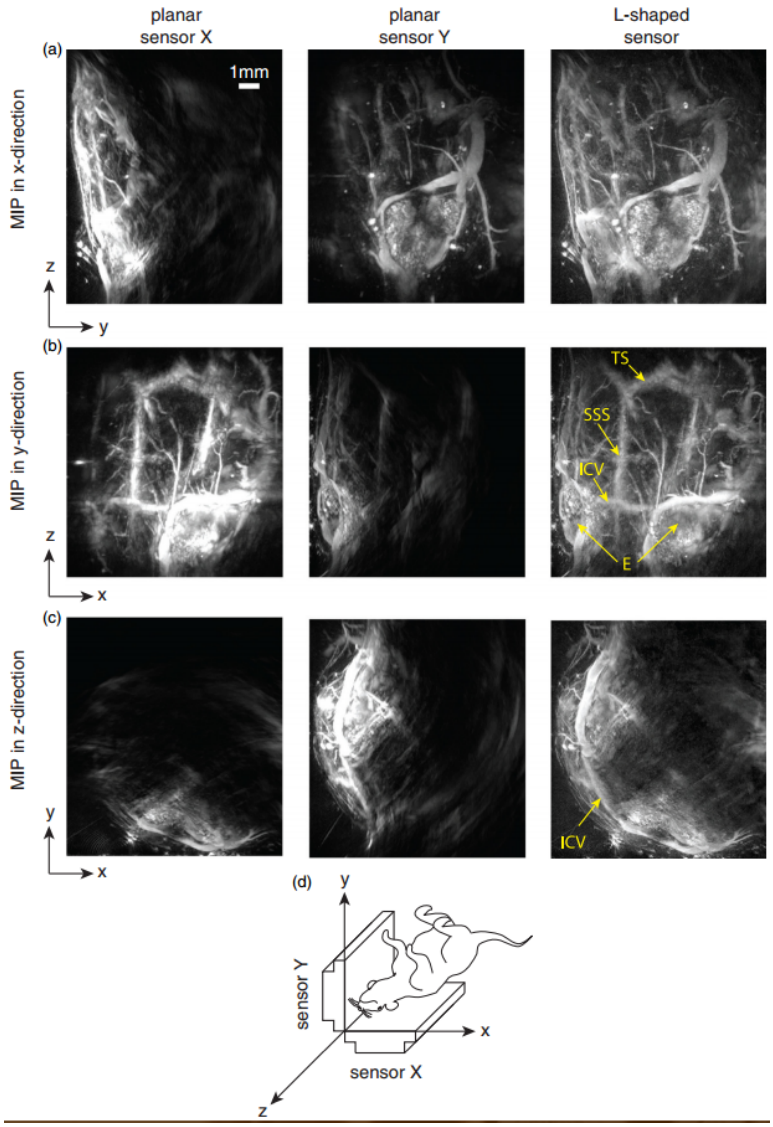

Figure 2.6: *Ex vivo* images of a mouse head. (a-c) shows three different orientations for the orthogonal sensor pairs, along with a schematic of the layout (d). In the images several major vessels and structures are visible including the transverse sinus (TS), superior sagittal sinus (SSS), inferior cerebral vein (ICV), and the retia of the eyes (E) [11].

generally involve ring shaped wave guides printed on a substrate which is acoustically coupled to the sample, and are characterized by extremely high Q factors on the order of 10^5. As with the Fabry-Pérot, the acoustic pressure waves cause small deformations in the resonator which results in modulations of the transmitted optical intensity at a given wavelength. This is thought to primarily arise from pressure-induced effective refractive index changes in the polymer waveguide such that the sensitivity of the device is primarily represented by

$$s = \frac{dT}{dP} = \frac{dn_{eff}}{dP}\frac{d\lambda_r}{dn_{eff}}\frac{dT}{d\lambda_r} \tag{2.2}$$

Where T is the observed transmission through the waveguide at a given resonant wavelength λ_r, P is pressure, and n_{eff} is the effective refractive index. This theoretical sensitivity can also be linked to the Q-factor of the device following $S = A\lambda_r Q$ where A is a device-specific parameter determined by the materials and geometry used, and Q is the Q-factor.

These have demonstrated improved sensitivity over larger etalons with noise equivalent pressures of 29 Pa reported from an early device featuring a 60 μm diameter ring [71] where fabrication is detailed in [72]. Using a focused excitation, a lateral resolution of 5 um and axial resolution of 8 um was achieved. A later effort in [12] fabricated an optically transparent ring resonator using a fused quartz substrate with a total thickness of only 250 μm allowing for backward mode operation (Fig. 2.7). This group also reported an improved sensitivity with a noise-equivalent pressure of 6.8 Pa over a 140 MHz bandwidth. Owing to its extremely high bandwidth a group reported axial resolution to be 5.3 μm. Here the ring resonator device was positioned above the sample inside a common water tank, and the excitation light was focused on to the sample through the device.

Given their high sensitivity there has also been recent work looking at using whispering gallery mode resonators in an air-coupled orientation [73] which may be able to overcome the significant impedance mismatch resulting from air coupling and the high attenuation of ultrasound in air. Here the authors demonstrated an extremely high Q-factor ($\approx 10^7$) with extremely

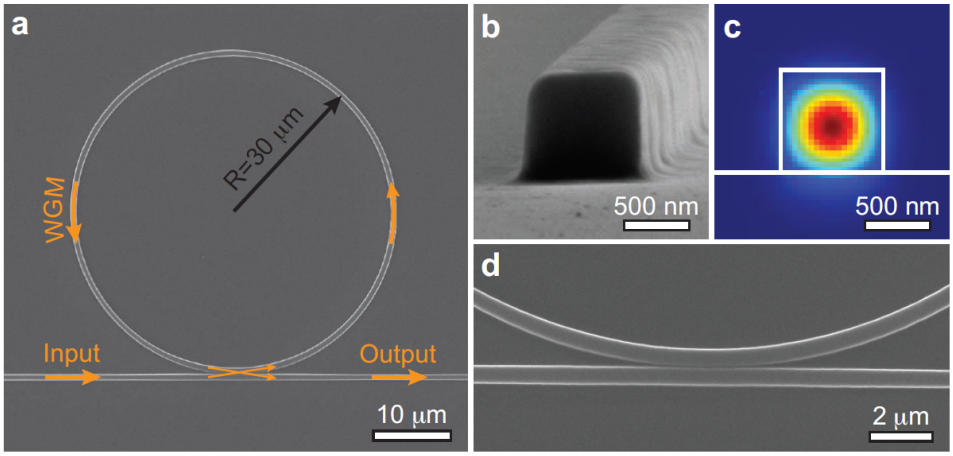

Figure 2.7: (a) SEM image of the 30 μm radius ring resonator used in [12] where (b) shows the waveguide cross section which features a side length of 800 nm. (c) highlights the calculated electric field inside the waveguide. (d) shows a zoomed in image of the coupling region of the device.

low noise-equivalent pressures in air of 215 mPa at 50 kHz and 41 mPa 800 kHz. Rather than sensing pressure due to changes in the effective refractive index of the resonator, this device operates on mechanical deformation. However the signal-to-noise was still relatively poor with values of 28 and 7 at 50 kHz and 800 kHz respectively.

2.3 Long-Range Interferometry

Although the resonator approaches provide excellent sensitivity they still have one of the same fundamental issues which existed from more conventional detection methods, in that acoustic coupling with the sample is still required. For non contact detection of ultrasonic signals air-coupled piezoelectric transducers have been examined with notably poor sensitivity [74]. Interferometric approaches have been generally making use of long- or short-coherence interferometric detection using a secondary probe beam, which is reflected off the sample and compared with a reference path. When the two beams are recombined their electric fields are summed providing sensitiv-

ity to both amplitude and phase modulations. Particle displacement has been commonly detected through both Michelson or Mach-Zehnder interferometers [75, 76], while surface velocity has been detected using confocal Fabry-Pérot interferometers [77, 78]. Much of the older efforts have made use of free space interferometers, however more modern implementations favor the use of fiber based devices. In general, this approach can be rather problematic due to the added complexity of adding a reference beam. In particular for low-coherence systems this may require additional considerations including the effects of dispersion and undesired movement in the referenced path.

An example of a Mach-Zehnder embodiment [13] demonstrated transmission mode imaging with lateral resolution better than 300 μm. Here the detection beam was split where both the sample and referenced paths pass through the water bath which encompasses the sample. The sample pathway is positioned at a point just outside of the sample such that it will be affected by outward propagating acoustic waves. The sample itself is then rotated and scanned along its axis to provide a full tomographic data set (Fig. 2.8). The obvious issue with this approach is that it involves a water bath and as such does not represent a true non-contact detection.

Some multi-modal devices featured interferometric photoacoustic detection sharing some of the same optical path as a time-domain optical coherence tomography (TD-OCT) system. For example [79, 80] utilizes a Mach-Zehnder interferometer separate from the OCT detection path. Trimodal systems have also been described with the addition of fluorescent imaging capabilities [81]. An early paper for an all-in-one device is described by [82] in which a small amount of oil is placed at the top of the sample to provide a strong reflecting surface. Here the probe beam consists of a short-coherence SWIR source provided by a super luminescent diode (SLD) which is processed by the same Michelson interferometer used by the OCT system. This provides a short-coherence interferometry system which can exclude extraneous noise from other surfaces in the sample which would be normally present from a long-coherence detection, and depth encoding is provided by time-encoding of the photoacoustic signals. The interrogation

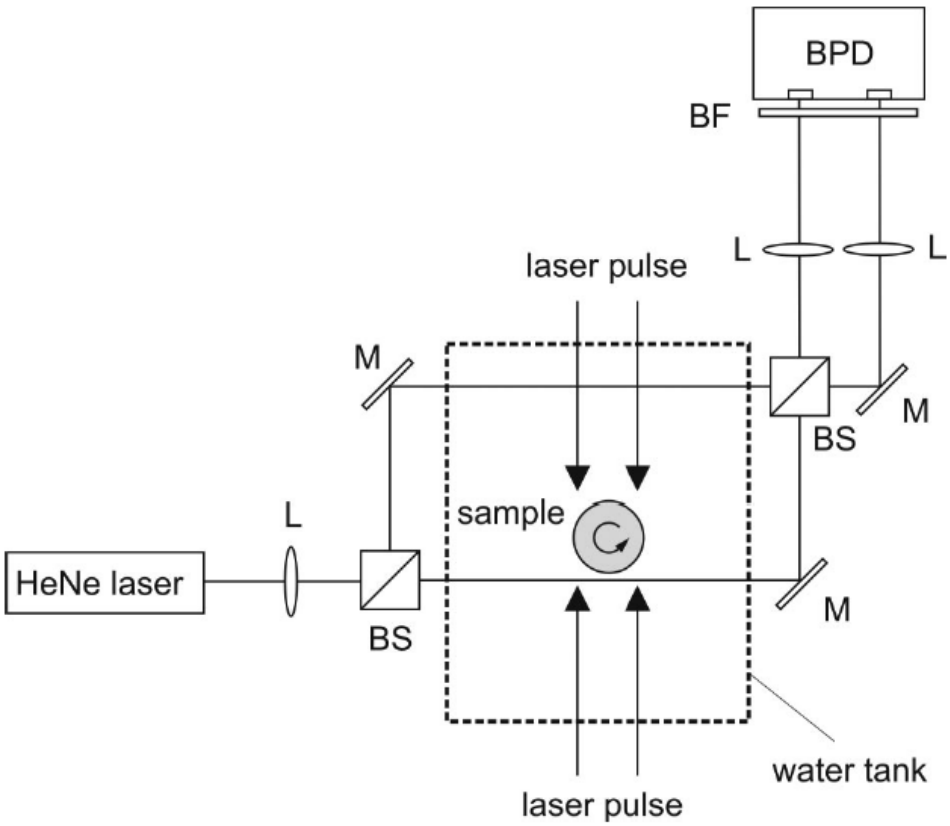

Figure 2.8: A schematic of a Mach-Zehnder interferometer used in [13].

point lateral positioning is provided by a two-axis scanning stage. For this early device, lateral and axial resolutions were relatively poor with values of 30 μm and 60 μm respectively. Later the group improved on this result [14] by implementing a micro-chip laser increasing imaging speed, and added a piezoelectric axial scanning mirror for improved stability. This newer device is reported as featuring 11 μm lateral resolution and 20.6 μm axial resolution, while providing a signal-to-noise (SNR) of 24 dB. This group was also able to demonstrate *in vivo* images of the micro vascular of a mouse ear (Fig. 2.9). Combinations with swept-source optical coherence tomography (SS-OCT) have also been explored, however results thus far have been comparatively poor [83].

2.4 PARS Microscopy

The motivation to create a non-contact all-optical photoacoustic modality is apparent, and towards this aim comes the development of a novel technique known as photoacoustic remote sensing microscopy (PARS). PARS utilizes a newly discovered detection mechanism which does not require interferometric detection architectures or the use of an external resonator. Since the first report of the technique from within our group (which the authour was involved with), [3] PARS has been demonstrably effective even compared to pre-existing contact-based approaches [84]. It has been characterized by exceptional resolution capabilities and sensitivity both in phantoms and *in vivo*. It accomplishes this while still maintaining many of the hallmarks associated with PA imaging such as the ability to perform linear spectral unmixing (such as blood oxygenation measurement). Beneficial properties have been observed experimentally. This includes improved penetration depths of up to 2.5 mm in a tissue mimicking medium, and over 1 mm *in vivo* [25] while maintaining optical-resolution. Also, the ability to image at extremely high acquisition rates (> 5 MHz) due to the novel detection mechanism has been demonstrated [30]. All published work to date on PARS has been conducted through Roger Zemp's lab at the University of Alberta. Much of the early work, including the initial discovery and report of the technique

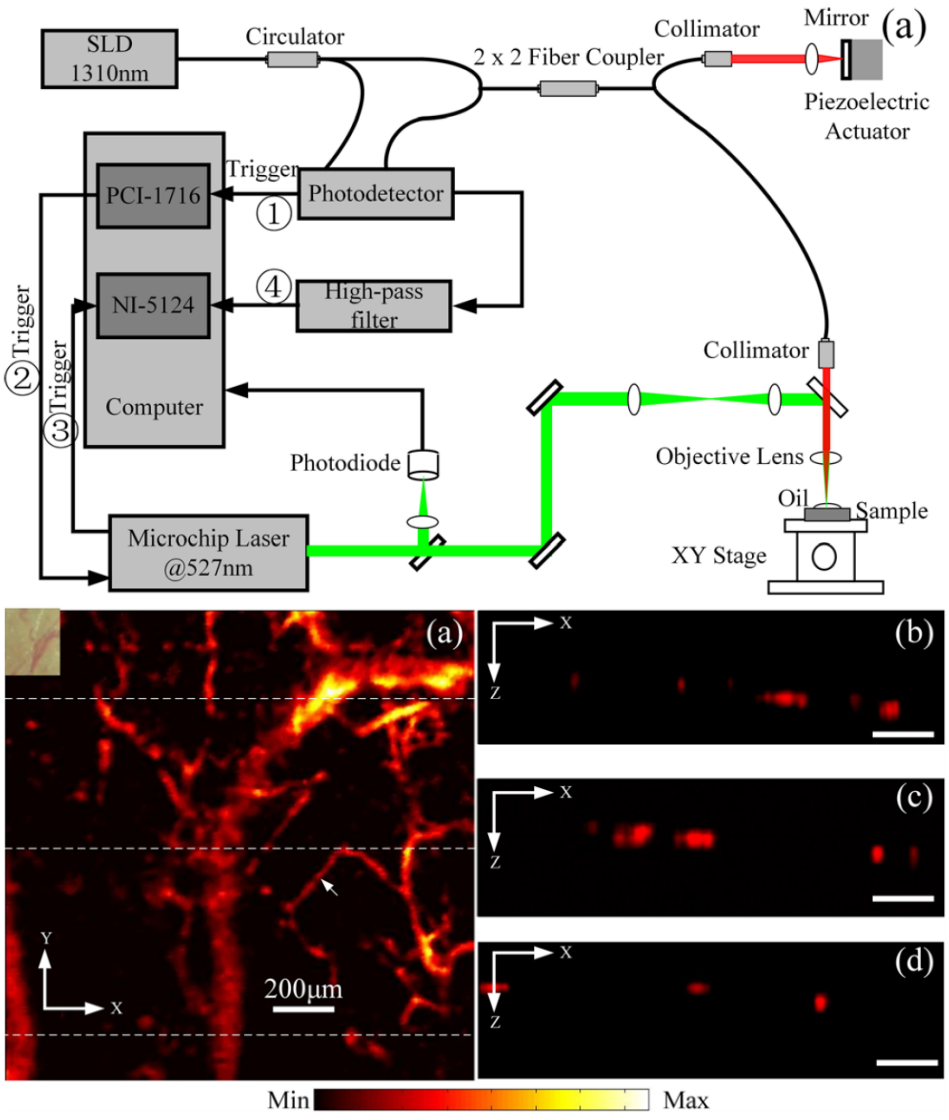

Figure 2.9: (top) shows a system diagram of a combined OCT non-contact photoacoustic system. (bot) shows *in vivo* photoacoustic image of microvasculature of a mouse ear. (a) en-face projection, (b-d) B-scan slices [14].

was heavily led by Parsin Hajireza, with contributions by the author. These contributions will be highlighted for given sections where appropriate.

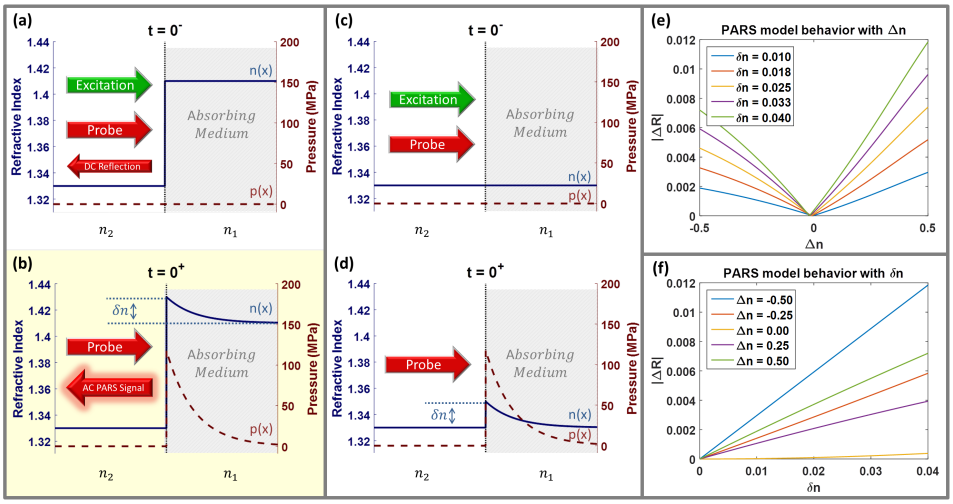

Figure 2.10: A brief overview of the PARS detection mechanism. (a) A pulsed excitation and a continuous-wave probe beam are co-incidence on an optical absorption and refractive index step. (b) Upon absorption of the excitation pulse the absorbing region undergoes photoacoustic excitation and builds an initial photoacoustic pressure. These large pressures induce elasto-optic modulation represented as a modulation to the local refractive index δn. This rapid change at the interface is observable as a modulation and the back-reflected portion of the probe beam. (c,d) If a sufficient pre-existing refractive index contrast is not present them the small change in reflectivity provided by the photoacoustic excitation may be insufficient to be observable. (e,f) Plots which highlight the predicted behavior $\Delta R = \delta n(n_1 - n_2)$ [3].

The PARS mechanism involves several sequential physical effects. In much the same way as conventional photoacoustics this starts with the absorption of a focused excitation pulse which develops an initial photoacoustic pressure rise. However, these large photoacoustic initial pressures may easily be in the range of hundreds of MPa while maintaining ANSI exposure limits [3]. These massive instantaneous pressures in turn can alter the local optical properties via the elast-optic effect [85]. This can be represented as a modulation to the refractive index within the excited region. These modulations can in turn alter the local reflectivity in the region which is

observable by cofocusing a continuous-wave probe beam to the excitation location and monitoring the returned portion of the beam. A simple argument for how this proceeds was presented in our first published work [3] which involves considering a planar geometry between two media where the reflectivity is described by Fresnel reflection coefficients. If one considers two media with refractive indices n_1 and n_2, then the intensity reflection is given by $R = |(n_1 - n_2)/(n_1 + n_2)|^2$. Now if one of these mediums, say n_2, is perturbed through the PARS mechanism by some amount δn_2 then a new reflectivity described by $R' = |(n_1 - n_2 - \delta n_2)/(n_1 + n_2 + \delta n_2)|^2$ is yielded. While monitoring the returned signal, and thereby the reflectivity, only relatively quick changes in reflectivity are monitored such that $\Delta R = R - R'$ is recovered. Although these photoacoustic initial pressures are quite extreme, the elasto-optic effect is quite weak such that for ~ 100 MPa in pressure, only a relatively small change in the refractive index is expected ($\delta n = \sim 0.01$ for water). At first this may seem too subtle of an effect to be a useful, however the change to the refractive index is partially amplified where an existing refractive index contrast exists. It is simple to show that in this example $\Delta R = \propto \delta n(n_1 - n_2)$ (Fig. 2.10e, 2.10f) [3]. This was in fact confirmed in preliminary experiments where phantoms were constructed to have an optical absorption contrast co-localized with various refractive index matching conditions. Although this may appear to be a potential weakness in the approach it is thus far not caused significant issue as optical absorption contrast and optical scattering contrast generally occur together.

Several other potential mechanisms were investigated upon the discovery of the process. Cavitation as a result of the large excitation energy could certainly cause sharp changes in the back-scattered light. However, it was demonstrated that within permissible exposure levels, the generated scattering signal followed a linear trend not indicative of micro-bubble formation. As well, comparing the time-domains of optical scattering in PARS and those from micro- and nanobubbles showed clear differences in the time-evolution of the signals. Another hypothesized signal source was from conductivity changes in the sample due to the large initial pressures. A simple wafer

device was constructed to attempt to monitor such changes but none could be found. Initially, the elasto-optic modulation of the perturbed region was thought to be too subtle of an effect to produce the large experimental signals, and it was not until observing the effective amplification effect provided to the reflectivity modulation by the pre-existing interface that the process was deemed as a plausible mechanism.

A basic PARS system is presented in figure 2.11 which highlights several key components. A near infrared (NIR) probe beam (here 1310 nm) is directed into a focusing objective lens such that it is cofocused with the excitation (532 nm). The reflected portion of the interrogation beam is directed onto a photodiode which monitors the intensity of the back reflected beam. This intensity level is indicative of the instantaneous reflectivity from the sample, which if assuming that the PARS mechanism is the dominant effect, is then indicative of the local optical absorption.

To date, work has already been performed on several aspects of PARS, from the first report [3] which first presented the PARS mechanism with the above simple description, and demonstrated preliminary experimental work towards characterization of the first-generation system. Further work has focused on the refinement of the physical model of the mechanism, and how it evolves in time. This was described for a simple planar geometry [1], followed by a similar description for small spherical scatterers [2]. A second-generation of the system was then developed which further improved the sensitivity and resolution characteristics. Along with these improvements, functional imaging was demonstrated [25], and the deep-sensing capabilities of the approach were examined [25]. The acquisition speed capabilities were characterized at up to 10 MHz [30] which is substantially faster than competing contact-based photoacoustic approaches ($\sim$ 1 MHz), and offers the prospect of rapid volumetric scanning. PARS has proven to be highly effective at visualizing microvasculature. This has been performed under several conditions including the chorioallantoic membrane (CAM) on chicken embryos, and several locations on mice including the ear, rear flank, and the surface of the brain. Initial efforts also show that it may be highly effective at full-body millimeter-scale animal model imaging such as zebrafish larvae.

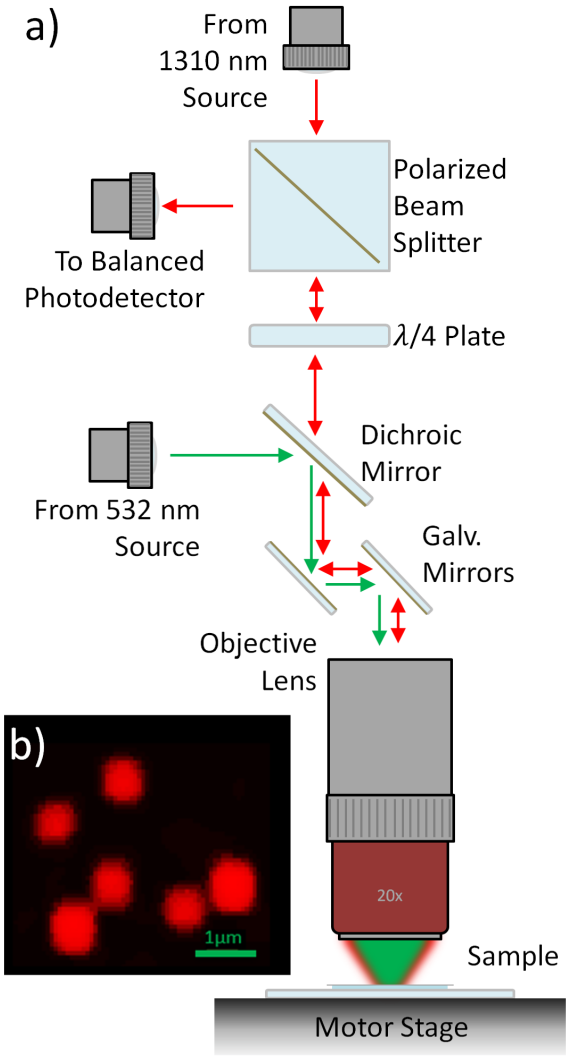

Figure 2.11: (a) A schematic highlighting the basic components of a PARS apparatus. Here, a 1310nm interrogation beam is fed through a polarized beamsplitter followed by a quarter waveplate to produce a circular polarization state. This is then combined with the 532nm excitation using a dichroic mirror. The two beams are then scanned by either using a set of galvanometer mirrors, or a motorized stage. Back-reflected interrogation light from the sample it is directed back through the scanning mirrors and the dichroic, before being returned to a linear polarization state orthogonal to the original such that it is now redirected in the polarized beamsplitter towards the photodiode direction. (b) A PARS image of 100nm gold medal-particles [2].

PARS microscopy presents an exciting new paradigm within the biomedical imaging community. The ability to operate non-contact opens previously inaccessible applications where absorption contrast can provide significant feedback to the user. Given the intense interest already expressed by the photoacoustic community, PARS is poised to be a significant area of development in the years to come.

2.5 Optical Coherence Tomography

Although much of this manuscript discusses the PARS mechanism and PARS-based modalities, in particular, chapter 6 also pulls heavily from the field of optical coherence tomography (OCT). Because of this, a brief background of this technique will be given here as well.

OCT as an imaging modality has been around since the early 1990s [86–88] although the fundamental concept has been around much longer in the fields of white-light interferometry and optical coherence-domain reflectometry [89,90]. OCT relies on the use of low-coherence interferometry. This provides a mechanism for sample ranging as interference of these wider spectra encodes information with regards to the distance from the sample and the reference paths. As opposed to a high-coherence interferometer which will allow interference between interferometer arms regardless of path lengths, in a low-coherence interferometer, only path lengths which are within a given coherence length (determined by the coherence of the light) will interfere. In OCT, this is used to provide depth-encoded information about the sample.

OCT devices commonly fall within two categories, time-domain optical coherence tomography (TD-OCT) and spectral-domain-OCT (SD-OCT) sometimes also called frequency-domain OCT. In a simple TD-OCT (Fig. 2.12a), a Michelson interferometer is set up such that one arm becomes the reference, and the other is impinging upon the sample. By scanning the length of the reference arm, the corresponding reference depth in the sample is interfered with. What results from this depth scanning is commonly referred to as an interferogram. This encodes the in-phase interference between the two paths in time as the reference path is scanned in depth. The

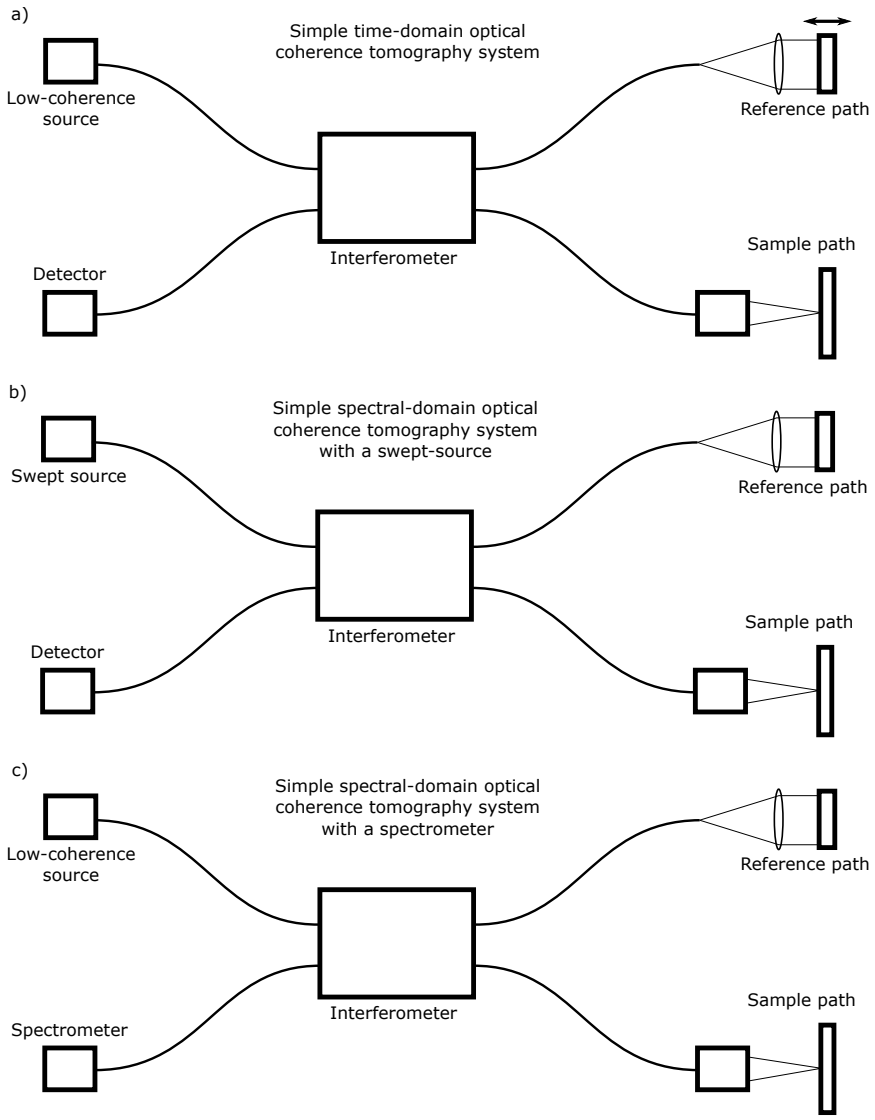

Figure 2.12: Three common architectures for OCT systems. (a) A TD-OCT, (b) a SD-OCT with a swept source, and (c) a SD-OCT with a constant source and a spectrometer.

envelope then of this signal represents the scattering profile of the sample in depth and constitutes a full axial interrogation (A-Scan). SD-OCT devices instead treat the interferometer as a large set of high-coherence systems. This is performed either as a swept-source implementation (Fig. 2.12b) where the detection source is ramped through a range of wavelengths and the results of each are recorded at a single detector like a photodiode, or a low-coherence source is used but detection is carried out using a spectrometer (Fig. 2.12c) which can track the resulting interference of each constituent wavelength independently. This allows for acquisition of full A-scans without any mechanical scanning of components. The benefits of SD-OCT over TD-OCT have been well discussed [89] but can be summarized as follows. The first clear advantage of SD-OCT comes from imaging speed. Whereas TD-OCT must carry out volumetric scanning, SD-OCT can acquire full A-scans within each interrogation time. This significantly improves volume acquisition rates and reduces mechanical complexity in the system. The other commonly cited benefit comes from improved sensitivity, as the multiple individual wavelengths act as a form of averaging, and as a result SD-OCT devices can commonly reach higher sensitivity than what their individual detectors can provide. These benefits come at the cost of system complexity and cost.

OCT techniques have proven particularly efficacious in recovering of tissue layers. For example in the field of ophthalmology which has seen wide adoption of OCT in the last decade uses the modality to image the structure of various components of the eye such as the cornea and retina [91], with some OCT microscopy devices capable of visualizing cellular structure [92,93]. Functional uses for OCT have come from detection of scattering fluid flows such as the flow of blood. This has been used in OCT angiography to visualize blood vessel structure and direction, and has been used to study various diseases such as diabetic retinopathy [94]. The modality has also demonstrated the capability for optical absorption measurement to some degree. This is accomplished by observing the shadowing effects from absorbing structures such as blood vessel when using visible detection wavelengths. These shadows are fit to known absorption curves to determine

their absorption properties. This has thus far demonstrated exciting results in mapping blood oxygen saturation in the retina [95] and, when combined with the capabilities of OCT angiography, has even been capable of mapping oxygen metabolism [96].

Both OCT and PARS feature all-optical architectures and provide complementary contrast to eachother. These aspects are likely to involve future investigations into combining the methods as dual-modality devices. Indeed, the subject of one chapter in this manuscript (Ch. 6) discusses a potential modality which combines properties of the two architectures into a single modality which is predicted to provide both the depth-encoded scattering contrast of a SD-OCT and the direct optical absorption contrast of PARS.

Chapter 3

The PARS Effect in 1D

The underlying mechanism behind the PARS microscope, simply named the PARS mechanism, was first proposed by Hajireza et al. [3]. However this only provided a highly idealized view without an understanding of the time evolution. This had been sufficient to provide a basic understanding of relevant contrast for the PARS microscope. Not only does it have a proportionality to the optical absorption as with more conventional photoacoustic approaches, but it also demonstrated some reliance on the intrinsic optical scattering within the region. Targets which where purposely constructed without scattering contrast produced negligible PARS signal. Clearly deeper understanding of the physical mechanism was required to develop a more complete understanding.

Following this motivation, a simple one dimensional description can be constructed. First, let us properly describe the physical experimental observations. Two beams of light are focused to the same spot on an optically absorbing and scattering sample, one of which is a nanosecond-pulsed excitation, the other which is a continuous-wave interrogation. The interrogation light which is back-reflected from the sample is directed upon a photodiode for measurement of its intensity value. Barring any outside influence, this measured intensity remains constant. However, directly following an excitation pulse a small sharp oscillation is seen in this intensity, which when proper alignment is achieved, has a relatively short life-span around 50 ns

to 300 ns. Experiments are normally performed with a high-pass filter applied to the electrical signal from the photodiode to reject the low-frequency scattering signals which would normally be used if the device was operated as a conventional laser-scanning microscope. With this filter the pulse has a sinusoidal shape reminiscent to acoustic-based photoacoustic signals. However, if this filter is removed the signal appears as an error function. This intuitively follows the previously presented "two state" model from the first report. If it is assumed that we are comparing an unperturbed sample and some earlier time-point with a modulated one from a later time point following an excitation event. However this model does nothing to tell of the time-dependent effects. What dictates the temporal characteristics of this signal such as the rise and decay times. These questions are at the forefront of the following modelling work.

This work was originally presented in [1]. The author's contributions included design of analytical model, producing and testing analytical approximations, coding and performing simulations, and authoring the manuscript.

3.1 The Photoacoustic Effect

Given the strong similarities to conventional photoacoustic imaging, an appropriate analytical starting point would be the photoacoustic equation. This describes the propagation and generation of photoacoustic induced pressures $p(\mathbf{r}, t)$. For simplicity we start with the equation for an inviscid medium

$$\left(\nabla^2 - \frac{1}{v_s^2}\frac{\partial^2}{\partial t^2}\right) p(\mathbf{r}, t) = -\frac{\beta}{\kappa v_s^2}\frac{\partial^2 T(\mathbf{r}, t)}{\partial t^2} \tag{3.1}$$

where v_s is the speed of sound, β is the thermal coefficient of volume expansion, κ is the isothermal compressibility, and $T(\mathbf{r}, t)$ is the rise in temperature due to the absorption of the excitation pulse. Since it is necessary to build local pressure, known as the photoacoustic initial pressure, heating must be done on a short time scale. To negate the effects of heat diffusion, the heating period must be less than the characteristic thermal relaxation

time τ_{th}. Likewise, if we would like to assume the accumulating pressure cannot simply escape the heating region during heating, the timescale must also be shorter than the stress relaxation time τ_s [34]. These are defined as follows

$$\tau_{th} = \frac{d_c^2}{\alpha_{th}} \tag{3.2}$$

$$\tau_s = \frac{d_c}{v_s} \tag{3.3}$$

where d_c is the characteristic size of the heated region, and α_{th} is the thermal diffusivity. Within these assumptions, the fractional volume expansion $dV/V = -\kappa p + \beta T$ is neglected such that the initial pressure rise is defined as

$$p_0 \approx \frac{\beta T}{\kappa} = \frac{\eta_{th}\beta A_e}{\kappa \rho_m C_v} \tag{3.4}$$

where η_{th} is the efficiency of the heat conversion, and A_e is the specific optical absorption. The material properties can then be collected to create the Grüeneisen parameter defined as

$$\Gamma = \frac{\beta}{\kappa \rho_m C_v} \tag{3.5}$$

This, along with noting that the specific optical absorption can be written in terms of the local optical absorption μ_{ex} and the fluence ϕ provides the form

$$p_0 = \Gamma \eta_{th} \mu_{ex} \phi \tag{3.6}$$

With the thermal and stress confinement conditions well satisfied we can rewrite the source term as

$$\frac{\partial T(\mathbf{r}, t)}{\partial t} = \frac{1}{\rho_m C_v} H(\mathbf{r}, t) \tag{3.7}$$

where ρ_m is the mass density, C_v is the specific heat capacity at constant

volume, and $H(\mathbf{r},t) = \eta_{th}\mu_{ex}\Phi$ with Φ being the optical fluence rate. Which finally provides the form of Eq. 3.1 that will be used from here

$$\left(\nabla^2 - \frac{1}{v_s^2}\frac{\partial^2}{\partial t^2}\right) p(\mathbf{r},t) = -\frac{\beta}{C_p}\frac{\partial H(\mathbf{r},t)}{\partial t} \tag{3.8}$$

where C_p is the specific heat capacity at constant pressure.

3.2 PARS Slab Model[1]

In an attempt to explore the most basic description of the PARS mechanism which appears possible, first we focus on the interaction of a planar surface in one dimension. The interface is described (Fig. 3.1a) as consisting of a top layer which is optically transparent to the excitation wavelength with refractive index n_1, and a lower optically absorbing layer with refractive index n_2 and optical absorption μ_{ex}. It will be assumed that the interface is perfectly planar and that both acoustic and electromagnetic plane waves are ideal plane waves. Acoustic dispersion, including attenuation will be ignored assuming that the model will only be valid over a short time and distance. This seems appropriate given the short experimental time domain signal as will be presented further on. For simplicity, acoustic heterogeneity will be ignored giving a constant acoustic propagation velocity over the considered region. Effects of optical dispersion will also be ignored assuming the central wavelength value over the respective excitation and probe beam bandwidths.

Starting by assuming an impulse excitation of a slab interface of thickness d in one dimension, the forward solution to the photoacoustic equation for an inviscid fluid in one dimension (Eq. 3.8) is [34]

$$p(z,t) = \frac{1}{2}p_0(z - v_s t) + \frac{1}{2}p_0(z + v_s t) \tag{3.9}$$

where $p_0(z)$ is the initial pressure distribution described as

$$p_0(z) = \Gamma\eta_{th}\phi_0\mu_{ex}\mathcal{H}\left(z + \frac{d}{2}\right)\mathcal{H}\left(\frac{d}{2} - z\right) \tag{3.10}$$

[1] The following section was taken from [1]

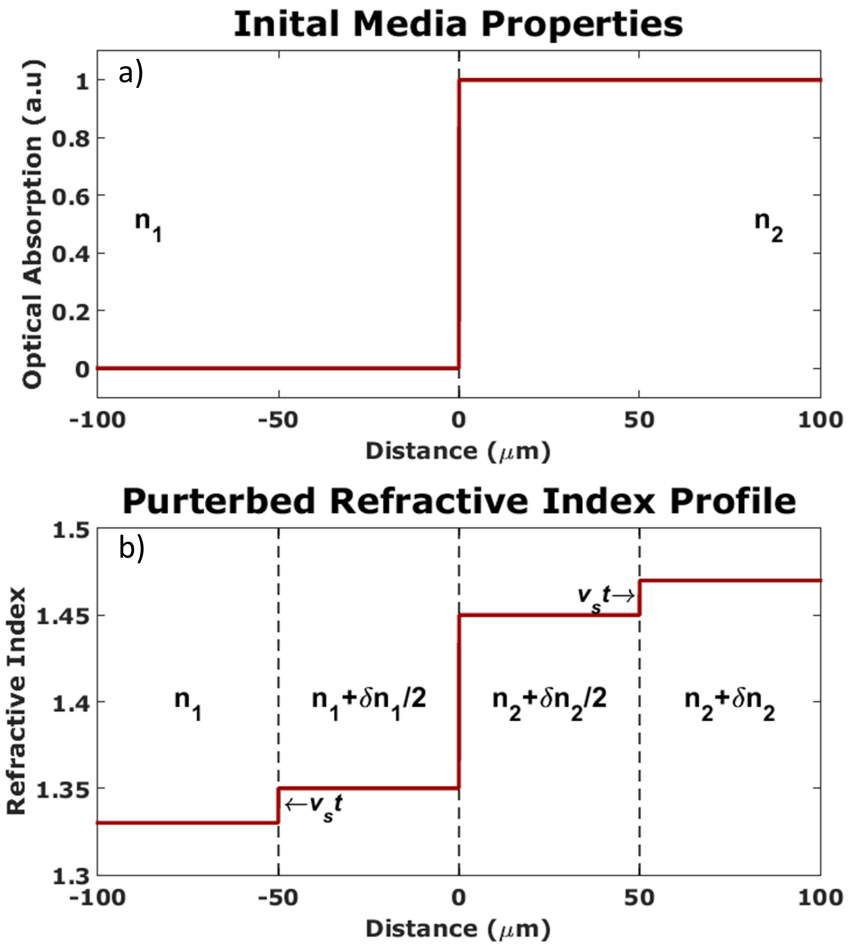

Figure 3.1: (a) The assumed initial state for the interface. It is represented as a step in both the refractive index and optical absorption where the top (n_1) medium is assumed to be optically transparent to the excitation wavelength, and the bottom (n_2) medium is absorbing to the excitation wavelength. Both the excitation and probe beams are incident from the n_1 medium. (b) A representative plot of the perturbed refractive index profile for some time after excitation from a temporal-impulse excitation. In general this profile consists of two propagating pressure waves forming a double etalon structure which results in oscillations of the intensity reflectivity of the probe beam as seen from the n_1 side.

where $\mathcal{H}(z)$ is the Heaviside step function. Since we wish to investigate a simple step interface, we can shift the coordinate system such that one of the interfaces is centered at zero and the thickness is taken towards infinity. Then assuming Beer's law attenuation with an optical absorption profile of the form $\mu_a(z) = \mathcal{H}(z)\mu_{ex}$ the initial pressure for an absorbing step becomes

$$p_0(z) = \Gamma\eta_{th}\phi_0\mu_{ex}\mathcal{H}(z)e^{-\mu_{ex}z} \tag{3.11}$$

When the propagation is considered over short distances such that $z \ll 1/\mu_{ex}$, the propagating pressure becomes (Fig. 3.1b)

$$p(z,t) = \begin{cases} 0 & \text{for } z < -v_s t \\ \frac{1}{2}p_0 & \text{for } -v_s t \leq z < v_s t \\ p_0 & \text{for } z \geq v_s t \end{cases} \tag{3.12}$$

These initial pressures can be quite large. In the case of a red blood cell (RBC) ($\mu_0 = 548$ cm^{-1} at 532 nm, assuming a HbO_2 concentration of 35g/dL) with a focal fluence of 500 mJ/cm^2 (commonly used in OR-PAM systems [16]) initial pressures are expected to be as high as 274 MPa. These large pressures can create non-trivial modulations $\delta n(z,t)$ in the local index of refraction $n_0(z)$ following the elasto-optic relation [97]

$$\delta n(z,t) = \frac{\epsilon n_0^3(z) p(z,t)}{2\rho_m v_s^2} \tag{3.13}$$

where ϵ is the local elasto-optic coefficient (≈ 0.32 for water). Refractive index changes due to absorption may in part be due to heating and not only pressures (This is in fact the basis of photo-thermal imaging), however in the first report [15] it was found that heating induced refractive index changes are a much weaker effect and that the observed transient signal behavior was on a time scale uncharacteristic of heat diffusion. This now provides a refractive index profile of (Fig. 3.1c)

$$n(z,t) = \begin{cases} n_1 & \text{for } z < -v_s t \\ n_1 + \frac{1}{2}\delta n_1 & \text{for } -v_s t \leq z < 0 \\ n_2 + \frac{1}{2}\delta n_2 & \text{for } 0 \leq z < v_s t \\ n_2 + \delta n_2 & \text{for } z \geq v_s t \end{cases} \tag{3.14}$$

where δn_m are the respective perturbations of the regions with refractive index n_m.

Within this impulse response abstraction, we can compare the maximum resulting difference in reflectivity ΔR from the profile by comparing the perturbed intensity reflectivity R' seen at time $t = 0^+$ with that of the unperturbed reflectivity R_s seen at time $t = 0^-$ such that

$$\Delta R = R' - R_s = \left| \frac{n_1 - (n_2 + \delta n_2)}{n_1 + (n_2 + \delta n_2)} \right|^2 - \left| \frac{n_1 - n_2}{n_1 + n_2} \right|^2 \tag{3.15}$$

This is the "two state" model presented in the first report. By assuming small perturbation ($|\delta n_2| \ll |n_2|$), and predominantly real refractive indices equation 3.15 could be well approximated to first order as

$$\Delta R = 4\delta n_2 R_s \frac{n_2}{n_1^2 - n_2^2} + \mathcal{O}\{\delta n_2^2\} \tag{3.16}$$

which demonstrates linearity with the perturbation δn_2, which is itself proportional to the focal fluence and optical absorption, and with the refractive index mismatch $n_1 - n_2$. It should be realized that absorption and scattering contrast are mixed, and not fully-decoupled.

At time scales short enough to ignore the effects of Beer's law attenuation ($t \ll 1/v_s \mu_{ex}$), after the initial impulse this profile (Fig. 3.1b) is structurally similar to two weakly reflecting Fabry-Pérot etalons which are increasing in thickness with time. This results in a modulation between the maximum transmission and maximum reflection of the structure. To examine the resulting intensity reflectivity seen by the probe beam the transfer matrix method is used. The reflectivity will be the ratio of the outward propagating wave and the initial incident wave represented by the T_{21} and T_{11} terms of

the system transfer matrix $\mathbf{T}$, respectively, such that.

$$R = \left| \frac{T_{21}}{T_{11}} \right|^2 \tag{3.17}$$

where

$$\mathbf{T} = \begin{bmatrix} T_{11} & T_{12} \\ T_{21} & T_{22} \end{bmatrix} = \mathbf{D}_0^- \left[\prod_{m=1}^{M} \mathbf{D}_m^+ \mathbf{P}_m \mathbf{D}_m^- \right] \mathbf{D}_{M+1}^+ \tag{3.18}$$

$$\mathbf{D}_{m-1}^- \mathbf{D}_m^+ = \frac{1}{t_{m-1,m}} \begin{bmatrix} 1 & r_{m-1,m} \\ r_{m-1,m} & 1 \end{bmatrix} \tag{3.19}$$

$$\mathbf{P}_m = \begin{bmatrix} \exp(ik_m L_m) & 0 \\ 0 & \exp(-ik_m L_m) \end{bmatrix} \tag{3.20}$$

where the product $\mathbf{D}_{m-1}^- \mathbf{D}_m^+$ forms the transmission-reflection matrix for the boundary between regions $m-1$, and m which are expressed in terms of the Fresnel amplitude transmission and reflection coefficients

$$r_{m-1,m} = \frac{n_{m-1} - n_m}{n_{m-1} + n_m} \tag{3.21}$$

$$t_{m-1,m} = \frac{2n_{m-1}}{n_{m-1} + n_m} \tag{3.22}$$

and relate the field amplitudes on either side of the boundary. The $\mathbf{P}_m$ terms are the propagation matrices where k_m are the mean wavenumbers, and L_m represents the path length through the m^{th} internal region [98]. Here the region $m = 0$ will be defined as the top-most layer from which both the excitation and probe beams arrive from, and $m = M + 1$ is the bottom-most layer assumed to be semi-infinite. Although this formalism can be used directly (and will be used for comparison later), it is far from intuitive as to how it will develop in time and what type of implications may arise. Since a reasonable approximation would be beneficial, the four region structure (Fig. 3.1b) is approximated by

$$k_0(\nu) = \frac{2\pi\nu n_1}{c} \tag{3.23}$$

$$k_1(\nu) = \frac{2\pi\nu n_1^*}{c} \tag{3.24}$$

$$k_2(\nu) = \frac{2\pi\nu n_2^*}{c} \tag{3.25}$$

$$k_3(\nu) = \frac{2\pi\nu n_2^{**}}{c} \tag{3.26}$$

where $n_1^* = n_1 + \delta n_1/2$, $n_2^* = n_2 + \delta n_2/2$, and $n_2^{**} = n_2 + \delta n_2$ are the refractive indicies in the perturbed regions, ν is the optical frequency, and c is the speed of light in vacuum. The time-varying thickness of the two internal regions will be $L_{1,2}(t) = v_s t$. However this result will be nonphysical and is mirrored about $t = 0$. Since the interface is expected to give an unperturbed intensity reflectivity R_s prior to excitation, this term is pulled out of the full expression with the remaining terms only evolving after the excitation ($t > 0$) yielding the form

$$R(t,\nu) = R_s + \mathcal{H}(t)\frac{a_0 + \sum_{m=1}^{3} a_m e^{-\alpha_m t} + \sum_{m=1}^{5} b_m e^{-\alpha_m t}\cos(\omega_m t)}{c_0 + \sum_{m=1}^{3} c_m e^{-\alpha_m t} + \sum_{m=1}^{5} d_m e^{-\alpha_m t}\cos(\omega_m t)} \tag{3.27}$$

where the $\alpha_m(\nu)$ and $\omega_m(\nu)$ terms relate to the imaginary and the real components of the wavenumbers respectively, and a_m, b_m, c_m, d_m are constants.

For values common to *in vivo* targets, this can be further refined. We develop an expression which is second order in the refractive index perturbation along with ignoring terms evaluated to be numerically small. The coefficients can be well approximated by assuming that the perturbations are small ($\mathrm{Re}\{n_i\} \gg \mathrm{Re}\{\delta n_i\}$, further details as to intermediate steps are included in Appendix A). Finally, assuming that the refractive indicies are primarily real (for the probe beam wavelength) such that the attenuation is minimal over the coherence length ($l_c\mu_{pr} \ll 1$), the following relationship can be found

$$R(t,\nu) \approx R_s\left[1 + \mathcal{H}(t)\left(\xi + \sum_{m=1}^{3}\gamma_m \cos(\omega_m t)\right)\right] \tag{3.28}$$

where

$$\xi = \frac{(n_1^2\delta n_2^2 + n_2^2\delta n_1^2)(n_1+n_2)^2}{16n_1^2n_2^2(n_1-n_2)^2} + \mathcal{O}\{\delta n_{1,2}^3\} \tag{3.29}$$

$$\gamma_1 = -\frac{\delta n_1(n_1+n_2)}{2n_1(n_1-n_2)} + \mathcal{O}\{\delta n_{1,2}^2\} \tag{3.30}$$

$$\gamma_2 = -\frac{\delta n_2(n_1+n_2)}{2n_2(n_1-n_2)} + \mathcal{O}\{\delta n_{1,2}^2\} \tag{3.31}$$

$$\gamma_3 = \frac{\delta n_1\delta n_2(n_1+n_2)^2}{8n_1n_2(n_1-n_2)^2} + \mathcal{O}\{\delta n_{1,2}^3\} \tag{3.32}$$

$$\omega_1(\nu) = \frac{4\pi\nu v_s n_1^*}{c} \tag{3.33}$$

$$\omega_2(\nu) = \frac{4\pi\nu v_s n_2^*}{c} \tag{3.34}$$

$$\omega_3(\nu) = \frac{4\pi\nu v_s n_3^*}{c} \tag{3.35}$$

where $\omega_m(\nu)$ are signal frequencies gained through interferometric effects in the structure with amplitudes γ_m, ξ is a perturbation of the signal mean in the excited state from the static state R_s, and $n_3^* = n_1^* + n_2^*$. Comparing equation 3.28 with the earlier maximum-amplitude expression from [15] it is clear that the same general relationships hold such that the total modulation in reflection $\Delta R(t,\nu) = R(t,\nu) - R_s$ is roughly linear with both the refractive index perturbations $\delta n_{1,2}$ and the static refractive index mismatch $n_1 - n_2$.

To properly model the effect of interrogating this interface with a low-coherence probe beam it must be considered for the entire probe-beam spectrum. Since the detection path does not provide any additional phase sensitivity, the total intensity reflection of the spectrum is considered to be the weighted sum of the individual wavelength intensity reflection contributions following

$$R_{lc}(t) = \int S(\nu)R(t,\nu)d\nu \tag{3.36}$$

where $S(\nu)$ is the normalized intensity lineshape function of the probe beam which is assumed to be a Gaussian of the form

$$S(\nu) = \left(\frac{2}{\Delta\nu}\sqrt{\frac{\ln(2)}{\pi}}\right)\exp\left(-4\ln(2)\frac{(\nu-\nu_0)^2}{\Delta\nu^2}\right) \tag{3.37}$$

where $\Delta\nu = (c/l_c)\sqrt{2\ln(2)/\pi}$ is the FWHM bandwidth of the probe beam with coherence length l_c. The perturbation of the intensity reflection coefficient is thus evaluated as

$$\Delta R_{lc}(t) \approx R_s\mathcal{H}(t)\left[\xi + \sum_{m=1}^{3}\gamma_m\cos(\omega_{0,m}t)\exp\left(-\frac{1}{2}\frac{t^2}{t_m^2}\right)\right] \tag{3.38}$$

where

$$t_m = \frac{1}{2\sqrt{\pi}}\frac{l_c}{n_m^* v_s} \tag{3.39}$$

$$\omega_{0,m} = \omega_m(\nu)|_{\nu=\nu_0} = \frac{4\pi\nu_0 v_s n_m^*}{c} \tag{3.40}$$

The resulting consequence of considering an interaction over a wide spectrum is that the high frequency content which resulted from the etalon-like structure ceases for some time greater than t_m which is described by the coherence length and the acoustic propagation velocity in the two internal regions.

As a final step it would be highly useful to provide an expression for a finite excitation of this interface. Despite the above expression ($\Delta R_{lc}(t)$) not being inherently linear with the excitation pulse, since the non-linear components (e.g. Eq. 3.29) are small the resulting convolved expression would be expected to approach that from a more rigorous approach (and this will be demonstrated to be a reasonable approximation). At least within values expected for *in vivo* conditions, performing time convolution on the previous equation agrees well with numerical analysis over a time-convolved pressure field. If the excitation pulse has a pulsewidth t_p defined as

$$W(t) = 2\sqrt{\frac{\ln(2)}{\pi t_p^2}} \exp\left(- 4\ln(2)\frac{t^2}{t_p^2}\right) \tag{3.41}$$

Then the result of time-convolution such that $R_c(t) = R_{lc}(t) * W(t)$ gives

$$\Delta R_c(t) \approx R_s \mathcal{H}(t)\left[\zeta_0 \xi + \sum_{i=1}^{3} \zeta_i \alpha_i \gamma_i \cos(\omega_i' t) \exp\left(- \frac{1}{2}\frac{t^2}{t_i'^2}\right)\right] \tag{3.42}$$

where

$$\alpha_i = \sqrt{\frac{2\ln(2)t_i^2}{t_p^2 + 8\ln(2)t_i^2}} \exp\left(- \frac{\omega_{0,i}^2 t_i^2 t_p^2}{2(t_p^2 + 8\ln(2)t_i^2)}\right) \tag{3.43}$$

$$\omega_i' = \frac{8\ln(2)\omega_{0,i} t_i^2}{t_p^2 + 8\ln(2)t_i^2} \tag{3.44}$$

$$t_i' = \frac{1}{2}\sqrt{\frac{t_p^2 + 8\ln(2)t_i^2}{2\ln(2)}} \tag{3.45}$$

$$\zeta_0 \approx \frac{1}{2}\left[1 + \mathrm{erf}\left(\frac{2\sqrt{2\ln(2)}t}{t_p}\right)\right] \tag{3.46}$$

$$\zeta_i \approx 1 + \mathrm{erf}\left(\frac{8\ln(2)t_i t}{t_p\sqrt{2(t_p^2 + 8\ln(2)t_i^2)}}\right) \tag{3.47}$$

with $\mathrm{erf}(z)$ being the error function. The consideration of a finite excitation provides a low-pass effect on the signal such that for pulse widths longer than $t_{p,max} = \sqrt{\ln(2)}(c/\pi n_i^* v_s \nu_0)$, the higher frequency oscillations will be rejected. However, the excited state offset (ξ) will remain for a longer excitation pulse which can explain how the current embodiment of the PARS system can function with a relatively long pulse ($\approx$ 1ns). In general, for a pulsewidth longer than $t_{p,max}$, the resulting signal would be that of the excitation pulse convolved with a temporal step function.

To examine the quality of the approximation (Eq. 3.42) it is compared with the original matrix expression given by equations 3.17-3.20. The

pressure field from a finite excitation is found by convolving the impulse-excitation pressure (Eq. 3.9) with the pulsewidth expression (Eq. 3.41). The continuous region is then highly discretized and put into the transfer matrix system. Apart from some small numerical instabilities the two are in good agreement (Fig. 3.2), and the approximation in equation 3.42 appears to be highly robust for common *in vivo* values ($1.33 \leq \mathrm{Re}\{n_{1,2}\} \leq 1.50$ [99]). In addition, both the pressure fields and the resulting EM reflection from the profiles were examined with FDTD simulation (Fig. 3.3). The pressure field is simulated assuming a heating function of the form $H(z,t) = \eta_{th}\mu_a(z)\Phi(t)$, where $\Phi(t)$ is the fluence rate, and the EM interaction with the resulting refractive index profile assumes no current sources or magnetic heterogeneities in the materials. Further simulation details are provided in appendix B. Both figures 3.2 and 3.3 show values considering a blood plasma - red blood cell (RBC) interface where the optical properties of blood plasma (4.6g/dL of albumin, 2.6 g/dL of globulin, and 0.38 g/dL of fibrinogen) are around $1.33 + 0i$ [100, 101] and optical properties of the RBC are approximately $1.428 + 0.002i$ [102, 103]. This interface is of particular interest due to the prevalent use of blood as an imaging target *in vivo*.

3.3 Experimental Validation[2]

The PARS system used to conduct experimental measurements is similar to that reported in [15], with the relevant basic components shown in figure 3.4. The system consists of a 532 nm, 1 ns pulsed fiber laser (IPG Photonics Corp. Oxford, MA) used as the excitation beam which is co-focus, and co-scanned with a 1310 nm low-coherence (38 μm coherence length) continuous wave superluminescent diode (SLD1018PXL, ThorLabs Inc., NJ) for the probe beam . The probe beam is passed through a polarized beam splitter (VBA05-1550, Thorlabs Inc., NJ) followed by a $\lambda/4$ zero-order wave plate (Thorlabs Inc., NJ). The two beams are then combined and co-scanned using a 2D galvanometer scanning mirror system (GVS012/M, Thorlabs Inc., NJ) and are focused on to the sample using a 0.4 NA achromatic objective

[2]The following section was taken from [1]

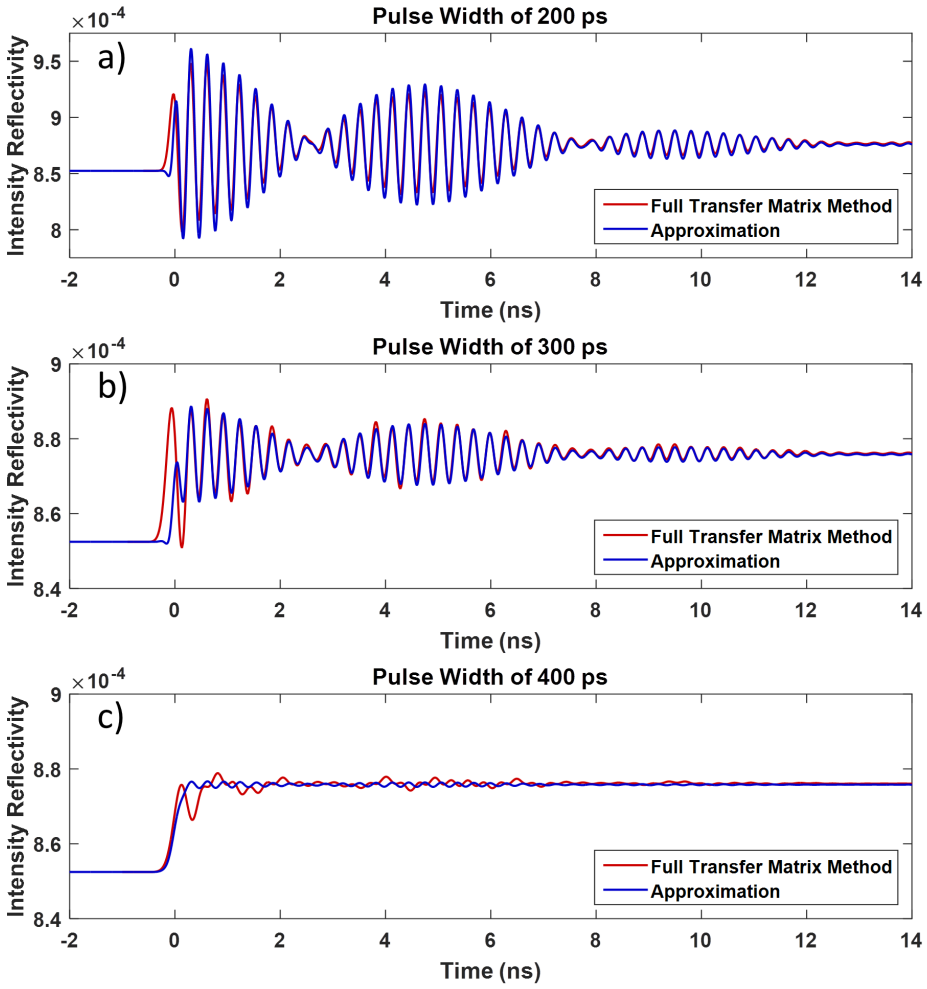

Figure 3.2: (a-c) A comparison between the approximation shown in equation 3.42 and performing a time-convolution on the pressure field in equation 3.9 for three different pulse widths t_p near the maximum pulse width for the system $t_{p,max}$. It is clear that well above $t_{p,max} \approx 160$ps the high frequency content is heavily reduced, with only a step remaining.

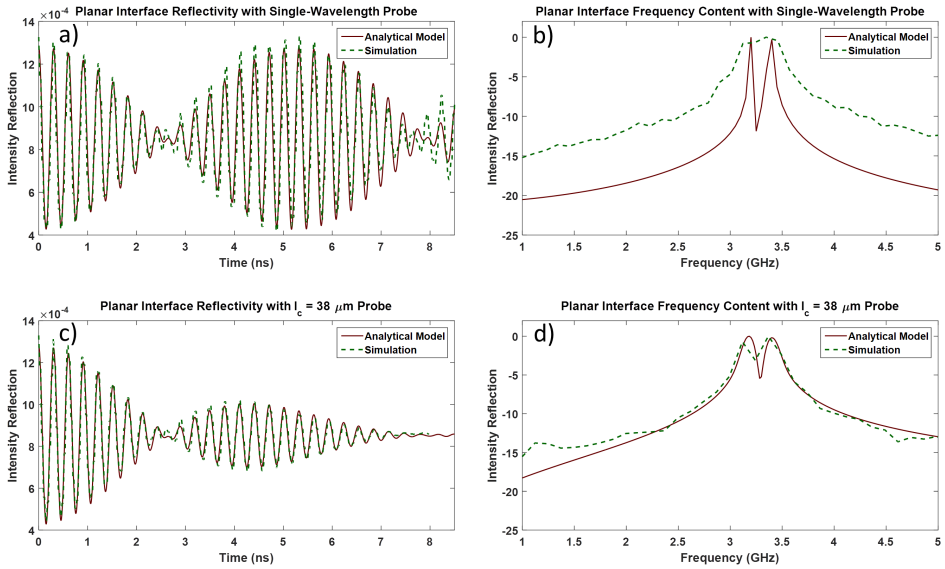

Figure 3.3: Comparison between the analytical model. (a) The resulting time domain signal from a single wavelength (1310 nm) interaction with a temporal-impulse excitation as described in equation 3.28 and its frequency content (b) compared with FDTD simulation of the same interface. (c) Likewise the resulting time domain signal from the same interface now accounting for the spectra content of a 38 μm probe beam as described in equation 3.38 and its frequency content (d). Both cases share the same two peaks which are located at $f_i = \omega_{0,i}/2\pi$, and the decay rate follows the sum of the gaussian envelopes $\sum_i \exp(-t^2/2t_i^2)$.

lens (M Plan Apo NIR 20X, Mitutoyo, Japan). The back-reflected probe beam returns through the $\lambda/4$ wave plate and is redirected through the polarized beam splitter and onto the photodiode for detection (low-bandwidth detection is provided by a PDB425C balanced detector (75 MHz), and high-bandwidth detection is provided by a PDB480-AC balanced detector (1.6 GHz), both from Thorlabs Inc., NJ). Low-bandwidth signals are captured on a 12-bit 125 MHz, 200 MS/s digitizer card (CSE1242, Gage applied, IL), and high-bandwidth signals are captured on a 16-bit 4 GHz, 20 GS/s oscilloscope (RTO1044, Rohde & Schwarz, OR). A silicon wafer used as a target is (100) single crystalline silicon. To test model hypotheses, predictions are compared against data from [15] in which targets consisting of dyed gelatin with different refractive-index fluids overtop were interrogated.

To examine the quality of the approximation (Eq. 3.38), it is compared with the original matrix expression given by Eq. 3.17-3.20. The pressure field from a finite excitation is found by convolving the impulse-excitation pressure (Eq. 3.9) with the pulse width expression (Eq. 3.41). The continuous region is then highly discretized and put into the transfer matrix system. Apart from some small numerical instabilities, the two are in good agreement (Fig. 3.5), and the approximation in Eq. 3.38 appears to be highly robust for common in vivo values ($1.33 \geq Re\{n_{1,2}\} \geq 1.50$ [99]). In addition, both the pressure fields and the resulting EM reflection from the profiles were examined with finite-difference time-domain (FDTD) simulation (Fig. 3.3). The pressure field is simulated assuming a heating function of the form $H(z,t) = \eta_{th}\mu_a(z)\Phi(t)$ where $\Phi(t)$ is the fluence rate, and the EM interaction with the resulting refractive-index profile assumes no current sources or magnetic heterogeneities in the materials. Further simulation details are provided in Appendix B. Both Figs. 3.5 and 3.3 show values considering a blood-plasma–RBC interface, where the optical properties of blood plasma (4.6 g/dL of albumin, 2.6 g/dL of globulin, and 0.38 g/dL of fibrinogen) are around $1.33 + 0i$ [100, 101] and the optical properties of the RBC are approximately $1.428 + 0.002i$ [102]. This interface is of particular interest due to the prevalent use of blood as an imaging target *in vivo*.

The behavior of the intensity reflectivity amplitude in relation to the

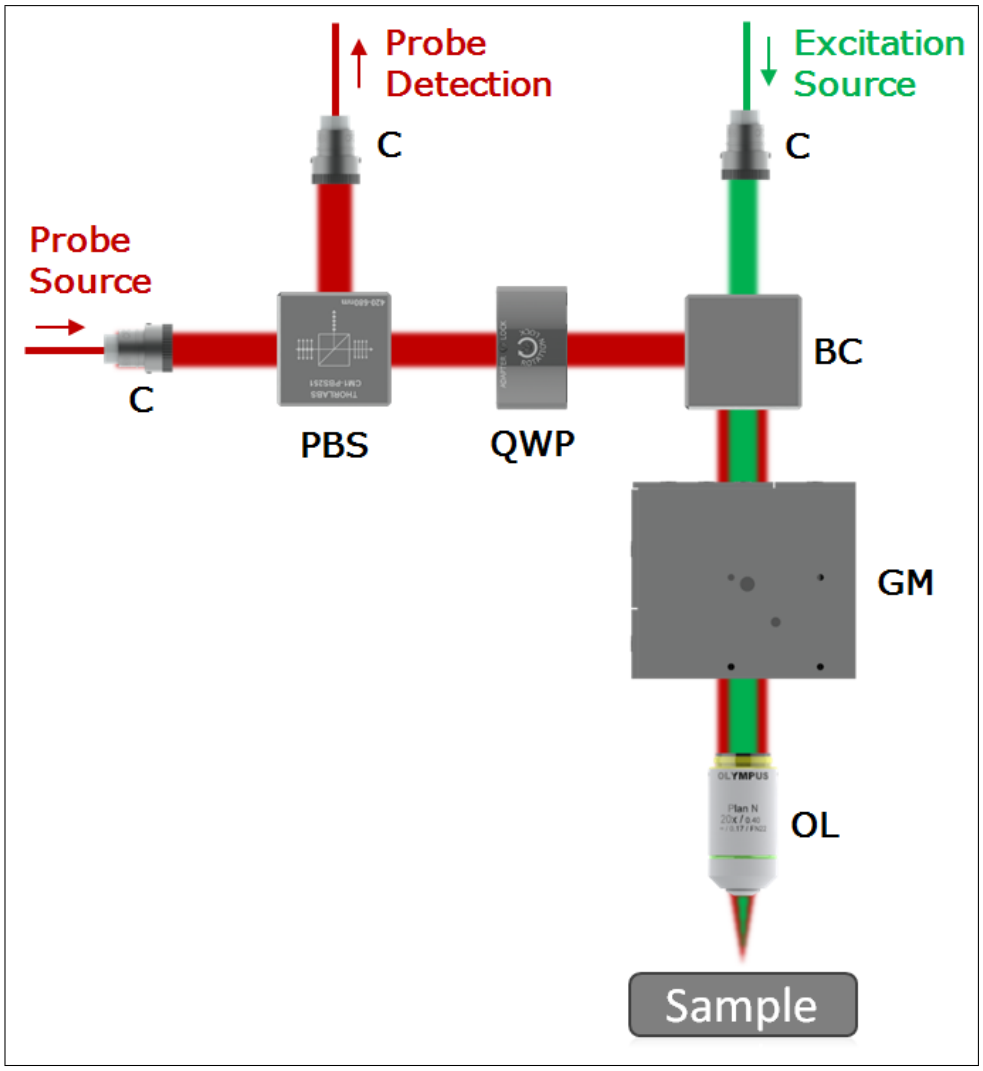

Figure 3.4: A simple schematic of the PARS system. A low-coherence SWIR continuous-wave probe beam is passed through a polarized beam splitter (PBS) and quarter wave plate (QWP) then combined with a visible nanosecond pulsed excitation beam. These are co-scanned through a galvanometer scanning mirrors system (GM) and co-focused onto the sample using an achromatic objective lens. The back reflected probe beam polarization is rotated by the quarter wave plate and directed onto a photodetector.

refractive index contrast (Δn) and to refractive index perturbation (δn) was compared with the previously reported behavior, Eq. 3 of [15] with good agreement (Fig. 3.5a,b). The Δn experiments were originally performed by preparing an optically absorbing phantom consisting of gelatin died with India ink ($n \approx 1.33$) below several top layers with varying refractive indices including a near matched condition. The δn perturbation is found to be proportional to both the excitation fluence and the optical absorption at the excitation wavelength.

Measurement of the time domain signals proved to be more difficult as an appropriately short excitation pulse ($t_p < t_{p.max} \approx 160ps$ for blood plasma - RBC interface) could not be sourced. In addition the detection bandwidth could only be increased to 1.6 GHz, where the lowest GHz frequency content is predicted to be centered around 3.1 GHz (for water or blood plasma). Still, in an effort to approach the initial assumptions of the model, such that it consists of a high finesse planar system a silicon wafer ($n_{532nm} = 4.142+0.032i$, $\mu_{a,532nm} = 7653$ cm^{-1}, $n_{1310nm} = 3.503+0i$ [104]) was placed below a shallow layer of water to act as a top medium. This structure was then probed with the PARS system with a representative time domain signal from the experiment being displayed in figure 3.5c.

Experimental time domain signals were found to be extremely short on the scale of $\approx$ 10ns. Since the analytical model does not provide any insight into a relaxation mechanism for the DC offset (ξ) term, a band pass filter was implemented to filter the model-predicted result which could account for possible high-pass effects in the system. A reasonable match was found for a high-pass filter set at around 8MHz. The actual photodiode response was difficult to model. Initial transient behavior is in good agreement but experimental relaxation and ringing was observed, which was not captured in the model. Possible reasons for these discrepancies will discussed in the following selection.

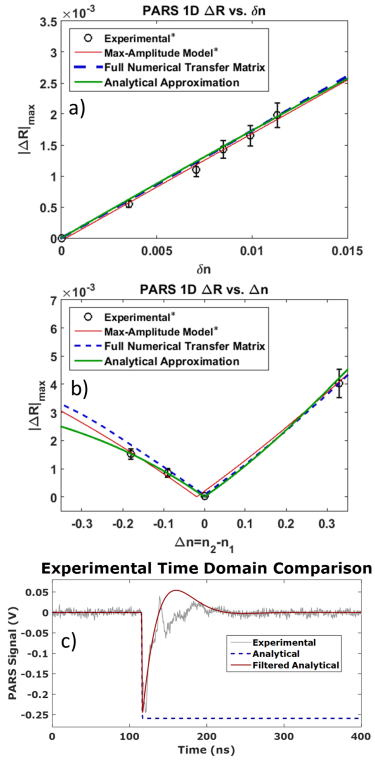

Figure 3.5: Comparison between experimental results and analytical model. (a) A plot showing the relationship between the PARS signal and the inherent refractive index contrast. Experimental values were previously reported [15] and collected using dyed gelatin phantoms submerged between various top players with differing refractive indices. The new analytical model agree is well with the previously reported maximum reflectivity model and to previous experiments. The behavior is roughly linear when the contrast is reasonably small. (b) The behavior of the PARS signal with the magnitude of the perturbation to the refractive index. Again the linear relationship is found in the new analytical model agreeing with previous efforts. (c) A representative experimental time domain signal for a water-silicon interface is compared with the analytical model. Due to the relatively long excitation pulse width currently implemented and system (1ns) no GHz modulations are expected, and rather the analytical model simply predicts a smooth step resembling an error function. However, the signal detection does utilize high-pass filtering along the signal path, and when combined with the detection's 1.6GHz bandwidth produces the reasonable agreement.

3.4 Discussion[3]

Analytical models predict that the observed signal behaves as a pair of moving Fabry-Perot etalons to produce characteristic oscillation frequencies determined by the intrinsic acoustical and optical properties of the media. As a result, prior knowledge of the expected frequency peaks in the signal could provide the ability to target specific species in a sample. In addition, the amplitudes of these GHz signals are predicted to be large compared to the perturbed offset for which the system is currently solely sensitive to. This may offer the potential to further increase measured signal without increasing fluence exposure to the sample, and may provide a method of further reducing noise through targeted filtering of these characteristic signals. The longevity of these oscillations depends on the coherence length of the interrogation beam and on the effective quality factor of the moving etalons, determined in part by the intrinsic optical absorption of the media. The height of these oscillations is determined by the width of the excitation pulse and is more pronounced for shorter pulses ($t_p < t_{max}$). However, they are nearly washed out for the nanosecond pulses used in the present experiment.It was found that both the amplitudes of these oscillations and the magnitude of the DC offset closely follow the behavior described by previously published simple models. It is also worth noting that significant attenuation of the probe beam can affect the longevity of these oscillations. These can be considered by allowing for imaginary components of the refractive indices in the original expression (Eq. 3.27).

Both the analytical model presented here and the experimental time domain signals demonstrate rise times on the order of the excitation pulse rise time. However they disagree on the relaxation time of the signal. This is evidently due to the one dimensional restriction in which the model was created. In the real system the excitation spot has a Gaussian profile with the waist around 1μm in diameter. Although the planar approximation is still likely valid over a short acoustic propagation distance, as this distant increases the wavefront will likely approach a spherical geometry causing

[3]The following section was taken from [1]

rapid decline in pressure. This could warrant further investigation in a more refined model which can account for an excitation beam which has finite width. A quick exploration of this effect by allowing the perturbations to follow a similar decay relation to that of the central amplitude for a Gaussian beam shows the system may return to the static state on the order of 10s of nanoseconds approaching values measured experimentally. This rapid decay time may be of importance since the system does not currently have any method of resolving depth beyond optical sectioning. It would allow for acquisition of data points at rates approaching 50MHz providing the ability to resolve high quality volumes in real time through 3D scanning of the focal spot. An improved understanding of these effects could lead to design optimization and minimization of signal ringing for signal localization and accelerating imaging speed.

The model predicts a linear relationship with the PARS signal to both the excitation fluence and the optical absorption at the excitation wavelength corroborating with previous efforts [15]. This is highly relevant since linear unmixing is a staple for photoacoustic modalities. Although the requirement for refractive index contrast may appear to be a limitation to the technique, it has thus far not been an issue outside of tailored experiments as a refractive index mismatch is generally concurrent with optical absorption contrast *in vivo*. Even given a small refractive index contrast such as the case when looking at a blood plasma - RBC interface, it has been sufficient to achieve high experimental SNR *in vivo* around 40 dB [15]. However, this factor may be of importance when considering exogenous contrast agents.

Chapter 4

The PARS Effect in 3D

Following the simple one dimensional planar interface description of the PARS mechanism, the next clear geometry to investigate is that of a spherical scatterer. More specifically an absorbing sphere which has a refractive index contrast with the background. This geometry has a well known result in optics with Mie scattering theory and its small-particle approximation Rayleigh scattering theory. Photoacoustics has also discussed this geometry [34], highlighting solutions for the acoustic wave propagating from a spherical absorber.

These small particles more closely resemble many real targets. For example it has been shown that red blood cells can be well approximated as Mie scattering particles [105], and resemble a mostly homogeneous absorbing particle due to the prevalence of hemoglobin. Likewise cell nuclei can be consider as absorbing particles due to the prevalence of DNA for an ultraviolet excitation. Also, a variety of popular photoacoustic contrast agents such as gold nanoparticles again fall into this category.

As in the previous chapter, it is assumed that the dominant mechanism involves the thermo-elastic-induced elasto-optic modulation of the absorbing region following excitation with a short optical pulse. Rather than considering how this effects the reflection from the excited region, for a spherical scattering target, the scattering properties become more relevant. The strength of the scatterer is related to the scattering cross-section (which is

normally different from the geometric cross-section of the particle). This property is dependent on the refractive index of the sphere and the background in Mie and Rayleigh scattering theories. Three different approaches with differing levels of complexity will be discussed and compared to each other. As with the planar model, this model begins looking at a simple two-stage system. Here the scattering cross-section of the particle is compared before and after the excitation event. This is handled with Mie theory and the Rayleigh approximation. For consideration of the time-evolution effects and more complex analysis must be performed. This will utilize multi-layer scattering theory to discretized the developing radial refractive index profile to predict a time-evolving scattering cross-section as the acoustic wave progressed through and away from the particle. The end goal of this work was to provide further insight into the mechanism of absorption-induced scattering modulation, enabling improved system design and future modeling approaches.

This work was originally presented in [2]. The author's contributions included design of analytical model, producing and testing analytical approximations, coding and performing simulations, and authoring the manuscript.

4.1 Analytical PARS Model for a Spherical Scatterer[1]

First, the elasto-optic relationship is written similar to that found in Eq. 3.13, now for a radially symmetric region we have[2]

$$\delta n(r,t) = \frac{\epsilon n^3(r) p(r,t)}{2\rho_m v_s^2} \tag{4.1}$$

where ϵ is the elasto-optic coefficient, $n(r)$ is the unperturbed refractive index, $p(r,t)$ is the photoacoustic pressure, ρ_m is the mass density and v_s is the speed of sound [97]. Here r is the radial coordinate and t is time. As well, v_s is considered to be homogeneous throughout the considered region. If this

[1] The following section was modified from [2]
[2] This point onwards is taken from [2]

modulation occurs coincident with a scattering contrast ($dn(r)/dr \neq 0$), an observable change to the back scattered light from the region can be measured through the backscattered fraction. For a single particle interaction this difference in intensity is known to be proportional to the change in scattering cross-section of a particle following $\Delta I \propto \Delta\sigma_s$ [34]. For a first consideration of a time-independent description of this process, the difference in scatteringn cross section between a perturbed state (where the refractive index of the scattering sphere is modulated by some amount δn_s) is compared to that of the same system before excitation. Both Rayleigh and Mie scattering theories are appropriate for this approach where their respective scattering cross-sections are defined as

$$\sigma_{s,Ray.} = \frac{8\pi a^2 x^4}{3}\left|\frac{n_s^2 - n_b^2}{n_s^2 + 2n_b^2}\right|^2 \tag{4.2}$$

$$\sigma_{s,Mie} = \frac{2\pi a^2}{x^2}\sum_{m=1}^{\infty}(2m+1)(|a_m|^2 + |b_m|^2) \tag{4.3}$$

where a is the particle radius, $x = 2\pi a n_b/\lambda$ is the size parameter, n_s and n_b are the unperturbed refractive indices of the sphere and background respectively, and a_m, b_m are the Mie theory scattering coefficients which rely on n_s and n_b and are given by equations 2.12 - 2.16 of [34].

The maximum measured signal would then be proportional to the difference in these two states following $\Delta I \propto \Delta\sigma_s = \sigma_s(n_s + \delta n_s) - \sigma_s(n_s)$ where δn_s is the perturbation of the refractive index in the sphere. Assuming primarily real refractive indices (for the probe wavelength), the Rayleigh approach can be well approximated for *in vivo* values (assuming $\delta n_s \ll n_s, n_b$) by the following expression

$$\Delta\sigma_{s,Ray} \approx 32\pi a^2 x^4 \delta n_s (n_s - n_b)\frac{n_s n_b^2 (n_s + n_b)}{(n_s^2 + 2n_b^2)^3} \tag{4.4}$$

This demonstrates a similar result to that seen in the planar geometry such that the observed signal is proportional to the perturbation (which is itself proportional to both the optical absorption and incident fluence) and

the static refractive index mismatch $n_s - n_b$. No approximation has been attempted for Mie theory.

These approaches do not consider the time evolution effects. The general forward solution to the inviscid photoacoustic equation for a spherical absorber is a well known result described in other works [34]. This impulse response which provides the radial pressure profile can then be timed-convolved to represent the effect of a finite-excitation pulse. The scattering properties for the spatial-temporal region within and surrounding the sphere can be determined through multilayer (ML) scattering theory [106–110] which follows as

$$\sigma_{s,ML}(n_s, t) = \frac{2\pi a^2}{x^2} \sum_{m=1}^{\infty} (2m+1)(|c_m|^2 + |d_m|^2) \tag{4.5}$$

where $c_m(t)$, $d_m(t)$ are the ML scattering coefficients. This requires nontrivial numerical computation well summarized in [111] and provided in appendix C. The ML approach will be considered the gold-standard over the time-independent models in what follows. The approach was compared against a limiting case where an ideal impulse excitation is considered without any acoustic propagation, in which case

$$\Delta\sigma_s(t) = \left(\sigma_s(n, 0^+) - \sigma_s(n, 0^-)\right) \mathcal{H}(t) \tag{4.6}$$

where $\mathcal{H}(t)$ is the Heaviside function. This limiting case was used to validate numerical implementation of Eq. 4.5. A final note, these models only consider simple single particle interactions and do not account for other scattering and absorption effects which will occur in a non-ideal setting such as *in vivo* operation.

System parameters used for simulated values are selected to match those of the experimental setup. A simple schematic is provided in figure 4.1a. In brief, a 1 ns, 532 nm pulsed excitation beam is co-focused and co-scanned along the sample with a 1310 nm continuous-wave interrogation beam. The reflected interrogation content from the sample is then collected. Further details of the system are described in [1, 15]. Two interfaces are selected

for investigation. First a red blood cell (RBC) ($n_{1310nm} = 1.428 + 0.002i$ [102,103]) is considered in a blood-plasma background (4.6 g/dL of albumin, 2.6 g/dL of globulin, and 0.38 g/dL of fibrinogen, $n_{1310nm} = 1.33 + 0i$ [100, 101]). Hemoglobin in RBCs serve as the most prevalent source of photoacoustic imaging contrast *in vivo*. The second target was selected as a gold nanoparticle, shown in figure 4.1b ($n_{532nm} = 0.544 + 2.231i$, $n_{1310nm} = 0.392 + 8.875i$ [112]) suspended in 0.1 mM PBS which is considered to be optically similar to water.

4.2 Experimental Validation[3]

Computational predictions are first performed and then compared against experimental results. To predict the effects of the inherent contrast ($\Delta n = n_s - n_b$) and the particle size parameter (x) on scattering cross-section modulations, we compute the resulting behavior from equations 4.3 and 4.5 (Fig. 4.2). These are considered separately for a constant background ($n_b = 1.5$, Fig. 4.2a, 4.2b) while varying n_s, and for a constant sphere medium ($n_s = 1.5$, Fig. 4.2c, 4.2d) while varying n_b. Several representative line plots from these data sets are shown in figures 4.2(i)-4.2(iv). Note that Rayleigh theory is excluded here but approaches the Mie scattering result for small particles ($x \ll 1$). In this small particle region ML has a distinct lack of Δn dependence in the observable modulation (Fig. 4.2a, 4.2i) for constant n_b, but does show behavior (Fig. 4.2c, 4.2i) for constant n_s. Both of these are contrary to Mie theory predictions. Two likely culprits for this discrepancy arise from the added temporal considerations. First in the small particle regime, an assumption of ideal stress confinement τ_s used in the Mie and Rayleigh approaches do not seem appropriate for respectively long excitation pulse-widths t_p (such that $t_p > \tau_s = a/v_s$) which will create lower available pressure amplitudes in the time-dependent ML description. Second, an acoustic enlargement effect may occur owing to out-propagating acoustic wavefronts. These acoustic wavefronts effectively create a temporary larger particle as seen by the interrogation beam. This

[3]The following section was taken from [2]

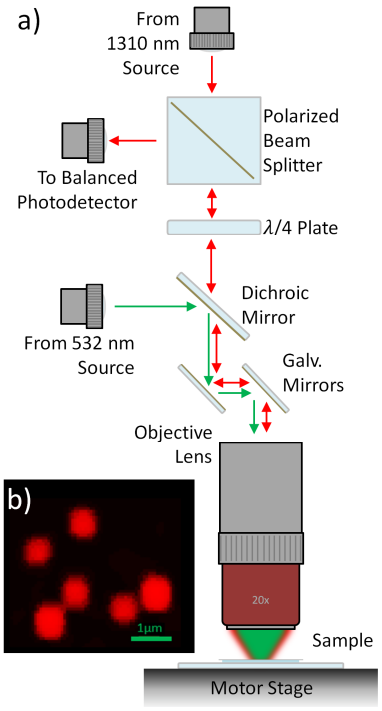

Figure 4.1: (a) Schematic of the experimental setup. Light from the CW 1310 nm SLD interrogation source is passed through a polarized beam splitter and quarter wave plate creating a circular polarized state. It is then combined with the 532 nm, 1ns pulsed excitation beam with a dichroic mirror. The two beams are scanned across the sample using either a set of galvanometer mirrors or a raster scanning motor stage. The reflected interrogation light is passed back through the quarter wave plate and redirected on to one side of a balanced photodetector. There it is compared with a small component of the original 1310nm source beam. (b) A representative image of 100 nm diameter gold nanoparticles taken with the PARS microscope.

acoustic enlargement is more significant for smaller particles, hence the observed strong nonlinearity in Fig. 4.2e. Though these wavefronts present relatively weak interfaces, the a^4 dependence on scattering with Rayleigh regime particles may provide an explanation to this behavior. Moving to larger particles (Fig. 4.2ii) there appears to be far better agreement in particular for the case of a positive contrast ($\Delta n > 0$). Here the effects of acoustic enlargement, and error from assuming ideal stress confinement are less significant.

Next the dependencies on the refractive index perturbation δn_s are investigated (Fig. 4.3). For small particles a nonlinear relationship as a function of excitation fluence is predicted. To experimentally validate these predictions, 100 nm diameter gold nanoparticles were imaged. Fractional scattering cross section modulations as large as 20 times the original cross-sections are predicted and observed. PARS signal strength as a function of excitation fluence agreed well with ML model predictions as shown in Fig. 4.3e (coefficient of determination of $R^2_{ML} = 0.935$, compared to $R^2_{Ray} = 0.752$, $R^2_{Mie} = 0.752$). For larger targets, such as those on the scale of RBCs, ML and Mie both predict linear dependences (Fig. 4.3c). Again, experiments follow suit (Fig. 4.3f) when targeting $\sim$6 μm diameter RBCs (R^2 values of $R^2_{Mie} = 0.979$, and $R^2_{ML} = 0.980$). Here scattering cross section enhancements of over 30% are predicted and observed. This is still a very significant modulation which is easily observable. For the case of larger particles we must also consider the corresponding interrogation spot size. Since all three scattering models assume an initial optical plane wave rather than a tightly focused spot, it is likely more appropriate to consider larger (with regards to the interrogation spot size) structures as being locally planar from the perspective of the interrogation beam and could be more accurately represented by the previously presented planar interface [1] which shows linearity to the perturbation.

Finally the time domain behavior from ML is presented in figure 4.4. The fundamental frequency of the pulse (taken as the maximum value in frequency content) depends inversely on the particle radius, with a ubiquitous low pass effect near 500 MHz which corresponds to the excitation

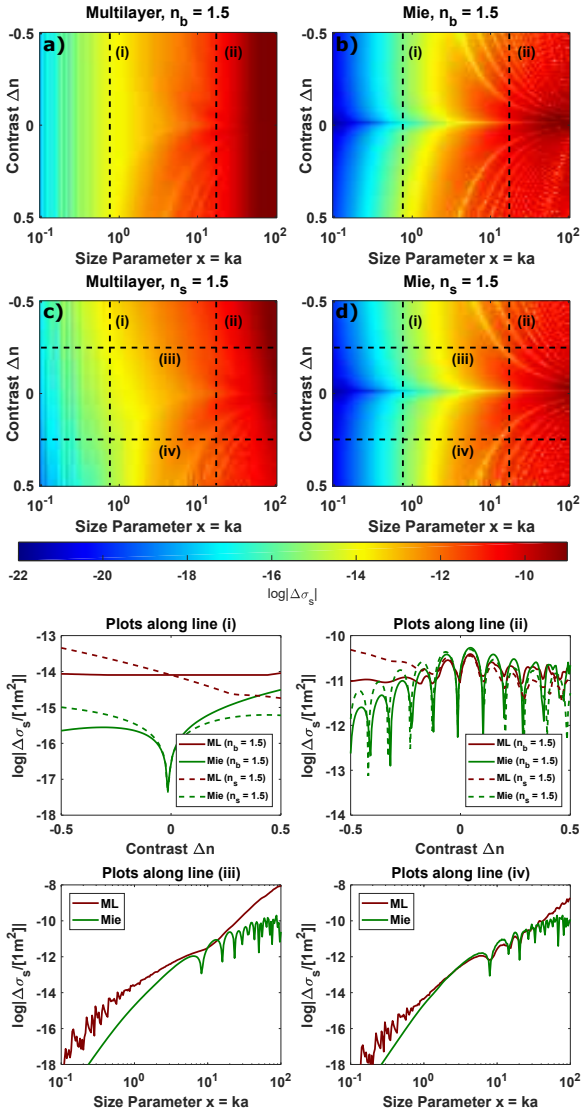

Figure 4.2: Representative plots for ML theory and Mie scattering theory approaches for an initial pressure of 120MPa and a probe wavelength of 1310nm. Particles and background are considered as non-absorbing ($\mathrm{Im}\{n_s\} = 0$ and $\mathrm{Im}\{n_b\} = 0$ at 1310nm). (a,b) show ML and Mie respectively while holding n_b constant. Likewise (c,d) for a constant n_s. (i-iv) Show representative line plots from the above 2D datasets.

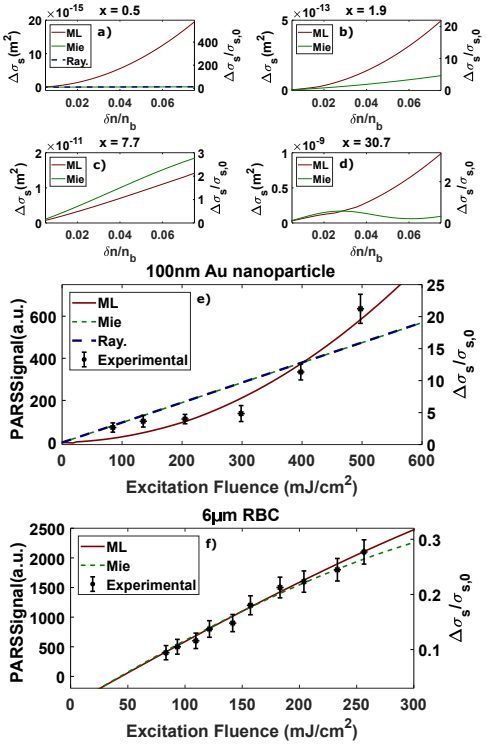

Figure 4.3: (a-d) Show signal dependence $\Delta\sigma_s$ (left axis) along with the corresponding normalized cross-sectional modulation $\Delta\sigma_s/\sigma_{s,0}$ (right axis) with the normalized perturbation $\delta n/n_b$. Parameters used assume a 120MPa initial pressure, RBC-like values for n_s, and blood plasma-like values for n_b. (e) Shows a comparison with experiment for a 100nm diameter gold nanoparticle and likewise (f) for an 6μm RBC. For experimental comparisons, predicted values undergo linear scaling along the vertical axis to provide the largest coefficient of determination. Note that the excitation fluences used are quite large (up to 500mJ/cm^2). However these values are not uncommon focal fluenc levels for OR-PAM systems [16], and are considered to be below the experimentally observed damage threshold and small animals [17]. The supplementary information section of [15] provides laser safety details for PARS.

pulsewidth used (1 ns). For smaller particles higher frequency harmonics are observed in the frequency content though some of these effects may be a result of numerical instability. One advantage of the PARS technique is the broad bandwidth available in modern photodiodes, which may allow for capture of the majority of the PARS signal spectra even for small particles. This is in contrast to bandwidth-limited ultrasound detectors which capture only a fraction of the emitted photoacoutsic power-spectral density. The current photodiode has a 75 MHz bandwidth. Convolving predicted PARS signals with such a band-pass response predicts signal durations on the order of 13 ns, which is less than the the $\sim$100 ns durations observed experimentally. Some of these longer signal durations may be due to acoustic reverberations, not currently considered. Future work should aim to include acoustic impedance mismatches and achieve closer experimental agreement. The previous chaper (Ch. 3) which considered a planar model discussed impact of interrogation beam linewidth on the PARS signal. In brief, the more narrowband the source the more temporal oscillations observed, and the longer the duration of the PARS signal. In the spherical model, these oscillations are less severe and the linewidth has a lesser effect on the PARS signal such that they do not appear to add any additional utility.

4.3 Conclusion[4]

In conclusion, we have demonstrated that scattering cross-section modulations are predicted when an absorbing scatterer is perturbed by a pulsed excitation. These effects can be very large, greater than 20 times that of the unperturbed scattering cross section. These large effects have not previously been elucidated to our knowledge. Scattering cross-section modulations result in local modulation of the backscattered light. A co-incident CW interrogation beam can then detect these modulations to provide photoacoustic detection. Static models aiming to explain this effect demonstrate conceptual value but fail to predict observations in experiments. However, a multilayer time-dependent approach encompasses more physical considera-

[4]This section was taken from [2]

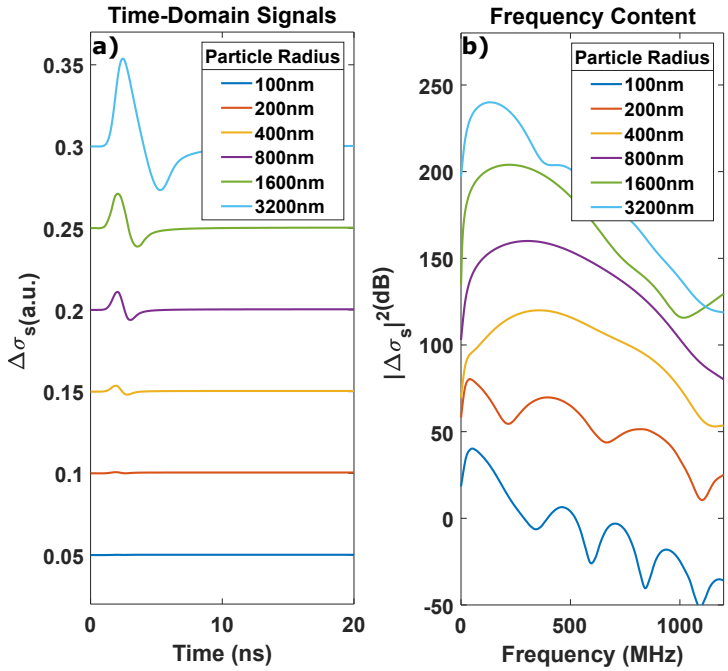

Figure 4.4: (a) Time-domain behavior and the respective (b) frequency-domain behavior of the PARS mechanism. Parameters used assume a 120MPa initial pressure, RBC-like values for n_s, and blood plasma-like values for n_b

tions including acoustic propagation and finite-pulse-width excitation. This approach correctly predicts nonlinear fluence dependence, experimentally observed in small gold nanoparticles. Acoustic enlargement effects associated with an out-propagating acoustic wave may amplify light scattering, and are captured by this multilayer model. The present models may prove important for future system design considerations as well potential optimization of contrast agents for use in PARS microscopy, and future efforts. Because PARS microscopy offers a high-signal-to-noise, non-contact alternative to optical-resolution photoacoustic microscopy, many exciting clinical, pre-clinical, and industrial applications are anticipated.

Chapter 5

Real-time functional PARS microscopy

Multiplex imaging with photoacoustic modalities has become a staple of the field, and has proven efficacious in label-free measurement of blood oxygenation [6], separation of DNA and cytoplasm [21], and separation of exogenous markers from surrounding signals such as blood [9]. Functional PA imaging is typically accomplished using illumination with a set of different wavelengths. This process takes advantage of the linear relationship between measured photoacoustic pressures and the chromophore concentration. This linear system can then be solved providing relative concentrations for relevant chromophore species. Commonly PA functional imaging is performed using two or more narrow-line illuminations requiring a tunable optical source [5]. However, other approaches for generating excitation wavelengths have been demonstrated such as the use of non-linear stimulated Raman scattering (SRS) within single-mode optical fibers. These have been implemented as a multi-wavelength source for conventional OR-PAM devices [113], and was recently reported for use as a functional PARS excitation source as well [25]. Note that this process is similar to that used in other work with single-mode fibers [114] and photonic crystal fibers [115]. This method of generating excitation wavelengths has benefits in terms of total system cost and complexity, but does not facilitate real-time acquisitions as

it requires manual changing of optical filters between acquisitions to provide desired excitation wavelength from generated SRS spectra. Previous works have demonstrated fast A-line rates (>5 MHz) [30] which suggest PARS is capable of providing real-time multiplex and functional imaging given an appropriate excitation source.

Here we present the first fully fiber-tetherable PARS system capable of real-time functional acquisition rates. Previous PARS system architectures used primarily free-space optics. This is accomplished by the implementation of additional fiber-based optical processing components, and utilizes the same SRS multi-wavelength generation method used previously [25]. However, as a means of improving imaging speeds, rather than filtering SRS spectra to provide a desired single-wavelength, here spectra are simply passed to the sample. We present a new wide-excitation unmixing algorithm to accommodate contributions from all wavelengths. As the spectral content of generated SRS spectra can be controlled by modulation of the pump power into the single-mode fiber, pulse-to-pulse switching of excitation spectra simply required the implementation of a fast optical modulator at the input. Phantom studies are conducted in blood flow phantoms where the SO_2 is characterized, followed by *in vivo* experiments recovering SO_2 maps from the ear of a mouse.

5.1 Full Spectrum Spectral Unmixing[1]

The unmixing problem follows closely from the single-wavelength method while allowing for contributions from each region of the spectrum. Rather than assuming two (or more) discrete excitation wavelengths, the full-spectrum method accounts for contributions from all wavelengths λ_i used to excite the sample. It is assumed that the effects of each fluence distribution $\phi_{S_n}(\lambda_i)$ in spectra S_n at a given region under interrogation sums to give the total photoacoustic pressure:

[1]The following section was modified from [116]

$$PA_{S_n} = \alpha \sum_{i=1}^{N} \mu_a(\lambda_i)\phi_{S_n}(\lambda_i) \tag{5.1}$$

where the optical absorption $\mu_a(\lambda_i) = \sum_{m=1}^{M} \varepsilon_m(\lambda_i)C_m$ is defined as in the single wavelength method with $\varepsilon_m(\lambda_i)$ and C_m being the molar extinction coefficient and concentration for species m respectively, and α is a constant which would require calibration to measure. This yields a linear system of equations of the form

$$\begin{bmatrix} PA_{S_1} \\ PA_{S_2} \\ \vdots \\ PA_{S_N} \end{bmatrix} = \alpha \begin{bmatrix} E_{11} & E_{12} & \cdots & E_{1M} \\ E_{21} & E_{22} & \cdots & E_{2M} \\ \vdots & \vdots & \ddots & \vdots \\ E_{N1} & E_{N2} & \cdots & E_{NM} \end{bmatrix} \begin{bmatrix} C_1 \\ C_2 \\ \vdots \\ C_M \end{bmatrix} \tag{5.2}$$

or

$$\mathbf{PA} = \alpha E \mathbf{C} \tag{5.3}$$

where

$$E_{nm} = \sum_{i=1}^{N} \varepsilon_m(\lambda_i)\phi_{S_n}(\lambda_i). \tag{5.4}$$

Solving for $\mathbf{C}$ gives the relative concentrations of the individual species within the interrogation region.

In the case where a narrow linewidth excitation is used with each source having equal fluence (ϕ_0), the sums in each element of E can be approximated as $\sum_i \varepsilon_m(\lambda_i)\phi_{S_n}(\lambda_i) \approx \phi_0 \varepsilon_m(\lambda_n)$, which recovers the conventional single wavelength unmixing technique. In this paper, only oxy- and deoxy-hemoglobin were considered as dominant chromophores, and oxygen saturation of hemoglobin (SO2) was estimated. This approach can provide substantially improved provided excitation pulse energy from the source (easily over 700%) when compared against the wavelength filtering approach as

discussed below.

5.1.1 Experimental Results[2]

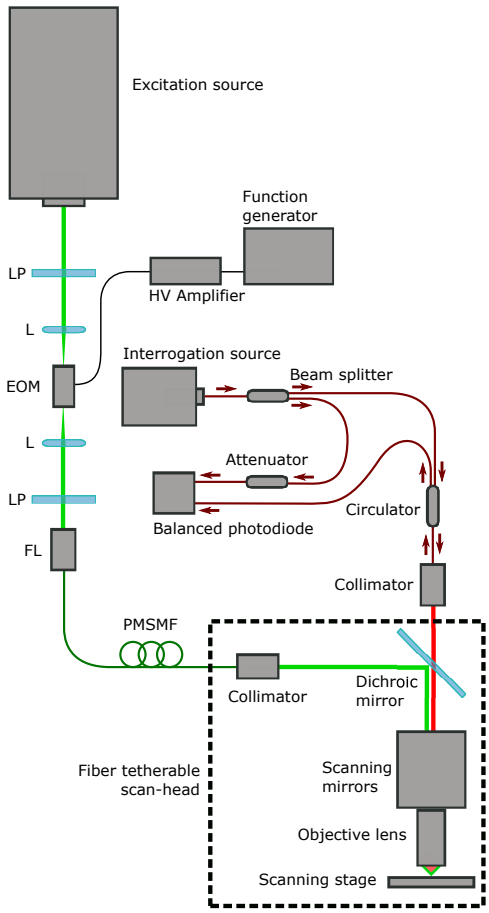

Figure 5.1: The PARS system used for fast functional imaging. The fiber tetherable scan-head is boxed.

Figure 5.1 shows PARS experimental setup. The output of a 532-nm 1-ns pulsewidth, ytterbium-doped fiber laser (IPG Photonics) capable of pulse repetition rates from 20 kHz to 600 kHz was coupled into a 4-m polarization-maintaining single-mode fiber (PMSMF) (HB-450, Fibercore

[2]The following section was modified from [116]

Inc., UK) through an electro-optic modulator (EOM) (EO-AM-NR-C4, ThorLabs). High power linear polarizers (LP) (GTH10M-A, ThorLabs) are used to control the polarization of the light into the PMSMF. The resulting optical switch can alter the fiber-coupled power pulse to pulse to generate different SRS spectra. These SRS spectra are formed from inelastic nonlinear interaction between incoming photons through the fiber and the molecules in the fiber itself. Visualization 1 shows the changes of the spectrum in a single mode fiber. Here the EOM was triggered at a slow rate (2 Hz) to make the changes in spectrum visible. A fiber optic spectrometer (USB4000, Ocean Optics Inc.) was used to characterize the SRS peaks. The output of the PMSMF was collimated using a collimator lens (F280APC-A, Thorlabs Inc.).

A 1310-nm continuous super-luminescent diode (SLD) source with 45 nm FWHM linewidth (SLD1018PXL, ThorLabs) was used for detection. The beam was split by using a 90:10 in-line fiber splitter (TW1300R5A1, ThorLabs). The 10% fraction of the light passes through an in-line variable attenuator (VOA50-APC, Thorlabs) and then connected to reference port of a balanced photodiode (PDB420C-AC, ThorLabs). The 90% fraction of the light passes through a circulator to interrogate the sample with a spot which was co-focused with the excitation beam and returned the reflected light to the other port of the 75-MHz-bandwidth balanced photodiode. The excitation and detection beams are combined using a dichroic mirror and then scanned across the sample via a 2D galvanometer scanning mirror system (GVS012/M, Thorlabs Inc.). The scanning mirrors were driven by a two-channel function generator (AFG3022B, Tektronix Inc.). The scanning light was then focused tightly using a 0.4-numerical-aperture objective lens (M Plan Apo NIR 20X, Mitutoyo, Japan). A 12-bit PCI digitizer (Gage Applied CSE1242) at a sampling rate of 200 MS/s is used for collecting the signals. For the applications which necessitate larger fields of view (FOV), a two-axis mechanical scanning system was used. Two Micos PLS-85 linear stages each driven by an Anaheim Automation MBC25081 bipolar microstep driver provide lateral sample movement down to a 1.25 μm step size while maintaining scanning mirrors in a fixed position.

Two fast spectral modulation schemes were implemented for comparison, both based on input power modulation of the excitation source. The first involved using one excitation spectra for forming a complete image then switching the excitation power to form a different excitation source spectra and forming another image. The second involved fast switching via the EOM so that shot-to-shot the spectra would be toggled. This approach does not require a second scan to form a functional image but may suffer from some pulse-to-pulse mis-alignment due to scanning motion.

Fig. 5.2a shows a carbon fiber network image using galvanometer scanning mirrors. The lateral resolution of the system is measured as 3 μm. Figure 5.2b shows red blood cells imaged in the mouse ear using galvanometer scanning mirrors. Figure 5.2c shows in vivo PARS images of en-face microvasculature in the ear of an 8-week old nude mouse (NU/NU, Charles River, MA, USA) using the two-axis lateral mechanical scanning stage. During the imaging session, the animal was anesthetized using a breathing anesthesia system (E-Z Anesthesia, Euthanex Corp.). In these images, a pulse energy of 50 nJ was used with interrogation power fixed at 5 mW. The SNR of the large vessels (average of maximum-amplitude-projection pixels in a region of interest over the standard deviation of the background noise found in a separate region with no vessels) is measured as $\sim$40 dB.

Figure 5.3a shows two SRS excitation spectra used to form functional images, each generated from different input powers injected into the single mode fiber. When these spectra are filtered substantial energy can be lost. For example, if the 565 nm peak is separated from the spectrum using a 5 nm linewidth filter, only 32 % of the spectrum's energy remains for functional imaging. Given that the SRS generation process already demands high input intensities on the order of several μJ for ns-scale pulses, throwing the majority of this energy away before interacting with the sample results is further inefficiencies. Figure 5.3b shows phantom validation experiments of the SO2 measurement accuracy using the functional PARS method. In this experiment blood mixed with different oxygen levels were injected into two separate tubes. The oxygenation of tube 1 and tube 2 were measured independently by a fiber-optic oxygen meter (FireStingO2,

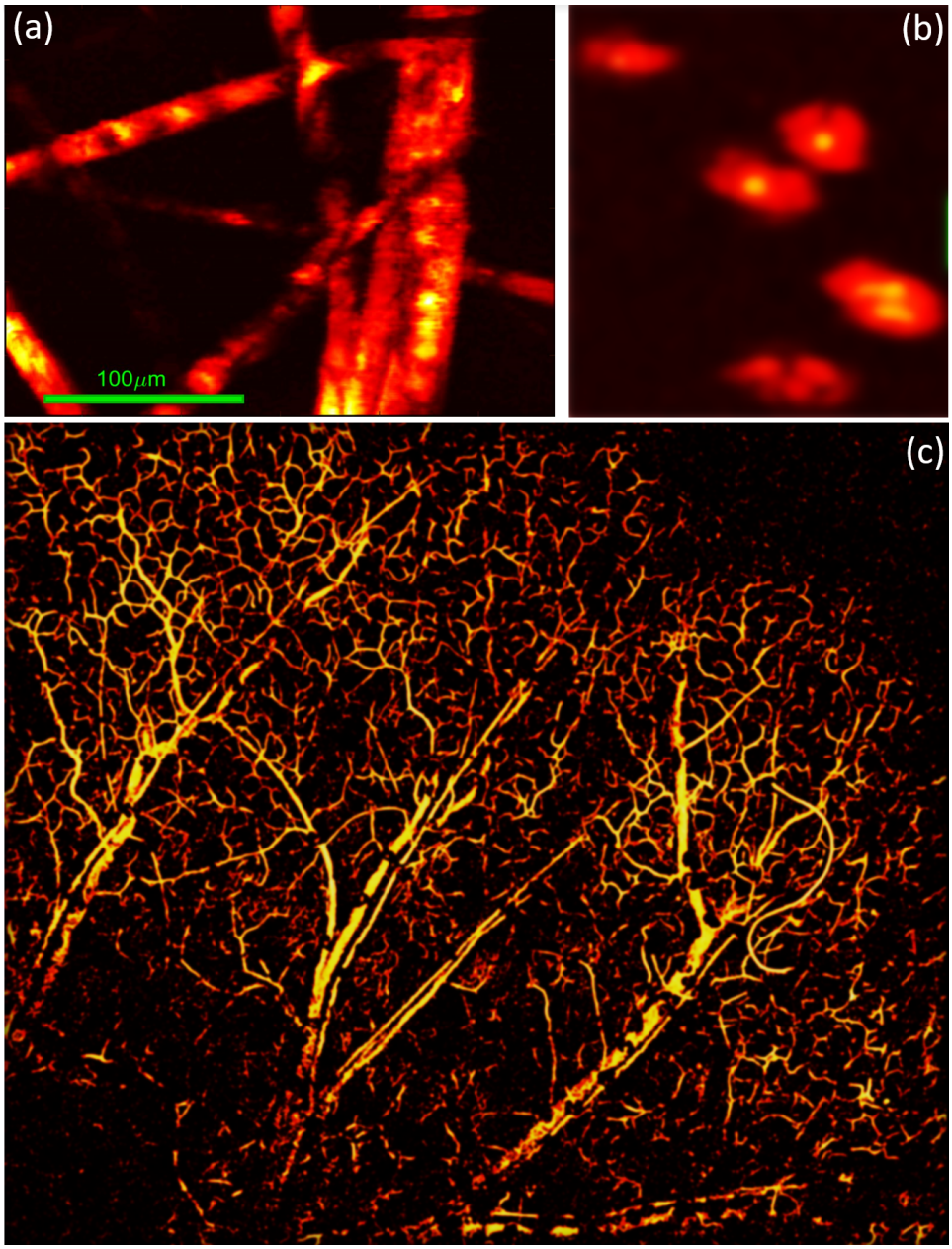

Figure 5.2: Structural characteristics of the system described in figure **??**. (a) Shows 7 μm carbon fibers, (b) shows red blood cells, and (c) shows the microvascular network with the ear of a Charles River athymic NU/NU mouse.

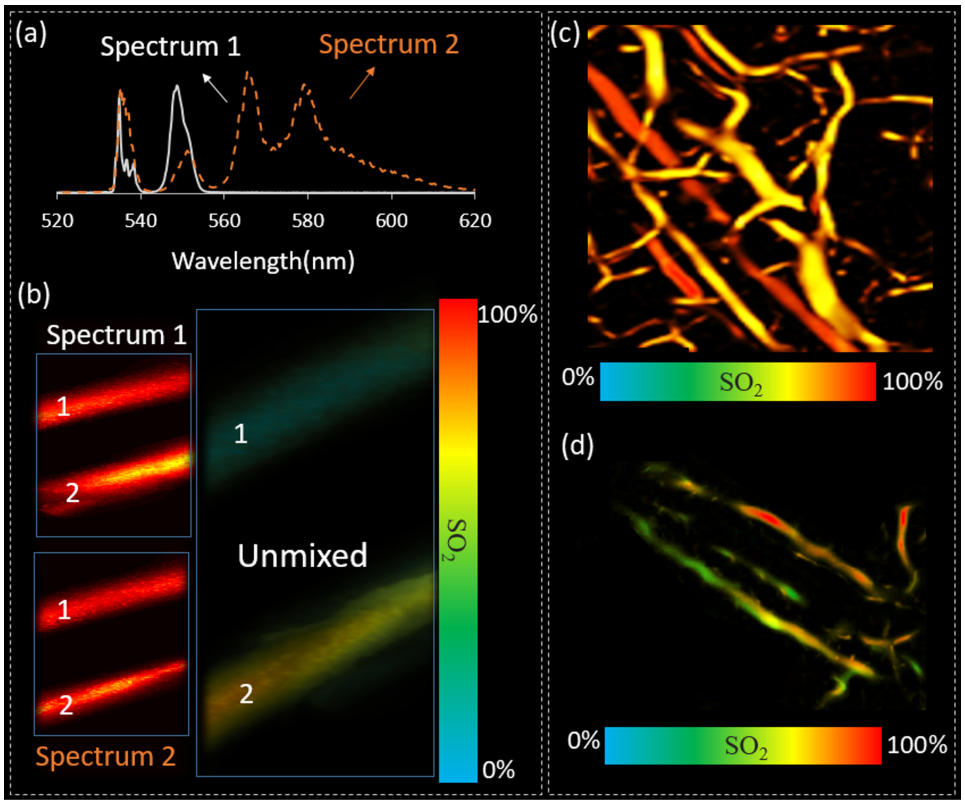

Figure 5.3: (a) Shows two representative SRS spectra acquired by switching the state of the fast optical swtich. (b) Shows the results of phantom experiments where two capillary tubes are filled with blood of different oxygenation states. The individual results of imaging with each spectrum individually are shown along with the unmixed result. (c-d) Shows *in vivo* results for performing SO_2 unmixing within the ear of a Charles River athymic NU/NU mouse.

PyroScience GmbH, Germany) and imaged simultaneously with functional PARS. The probe measurements showed 22% and 76% oxygenation in tube 1 and tube 2 respectively which was found to be within 5% accuracy with the unmixed result shown in figure 5.3b.

Figure 5.3c shows SO_2 measurement of a mouse ear when the EOM was off and two separate images using spectra shown in figure 5.3a are formed and unmixed as proposed earlier. Arteriole SO_2 is consistent with pulse oximetry measurements monitored simultaneously during the imaging session. Figure 5.3d shows SO_2 measurement of a mouse ear when the EOM was on to switch the spectrum at each excitation pulse. In this experiment only one image was formed. This method improves the imaging speed compared to the method using separate scans but exhibits inferior image quality as will be discussed. All of the experimental procedures were carried out in conformity with the laboratory animal protocol approved by the University of Alberta Animal Use and Care Committee. Authors were also trained and certified to use mice and rats in the research work. During the imaging sessions, animals were anaesthetized with isoflurane using a breathing anesthesia system (E-Z Anesthesia, Euthanex Corp., Palmer, PA, USA).

5.1.2 Discussion[3]

The approach presented here demonstrated an effective method for producing a functional multi-wavelength source capable of rapid pulse-to-pulse switching of wavelength content from a single source using non-linear SRS inside of a single-mode optical fiber. This facilitates the use of a single optical source for multi-wavelength excitation offering a low-cost alternative to multiple source systems. In addition, the broad-spectrum unmixing algorithm used allows for consideration of complex excitation spectra. This enables full SRS spectra to be used directly as excitation sources without the need to extract narrow-line pulses. In doing so, the full energy of the SRS pulse can be used in exciting the sample, and optical filtering at the fiber output does not need to proceed, facilitating real-time acquisitions from a

[3]The following section was modified from [116]

single optical source. However, the wide excitation spectra will potentially produce undesired chromatic aberrations within the system which may be difficult to correct for over narrow-line beams as achromatic optics must be implemented. The fiber-tetherable architecture used also facilitates future iterations of PARS devices such as handheld scan-heads and endoscopic probes. However, the current scan-head used in these experiments is still too bulky for use as a handheld device.

It was noted in these experiments that the signal to noise of the system of $\sim$ 40 dB was reduced with the introduction of a single-mode fiber collection compared with our previous free-space system ($\sim$ 50 dB [25]). Thus using the full energy of the SRS output, rather than applying a narrowline filtering, was particularly advantageous. The SO_2 image in Fig. 5.3d using fast EOM-switching shot-to-shot exhibited lower image quality than in Fig. 5.3c which formed two separate images at different input powers. One reason for this could be that slightly different locations are interrogated between laser shots due to scanning. Future work should aim to improve this.

In summary, the first all-fiber non-contact photoacoustic imaging system capable of providing cellular resolution is reported. By taking advantage of stimulated Raman scattering generated in a single mode fiber and a fast electro optic modulator a novel method of unmixing based on spectrum was shown.

Chapter 6

Coherence-gated PARS

Since detection is performed at the source of the acoustic pressures, the same time-gating approach used by other photoacoustic modalities to discern depth information does not apply with PARS. This in turn provides no depth information beyond that provided by optical sectioning necessitating depth-scanning. Despite this limitation, rapid acquisition (>10MHz point rate) is possible since the technique is primarily stress-confinement limited [30]. The modality is commonly operated at a high numerical aperture to provide tight lateral resolution, in which case the expected axial resolution is also potentially good at superficial depths. However, beyond superficial imaging depths degradation to the axial resolution will occur due to multiple scattering. These issues in part inspired the current investigation.

The purpose of this chapter is to introduce a PARS-based method for achieving depth-resolved images with optical absorption contrast. To accomplish this, we propose imaging depth-resolved changes in the refractive index immediately after an excitation pulse induces large initial pressures associated with light absorption. This could be accomplished through the use of an OCT A-scan which is sensitive to local scattering and infers a refractive index distribution. By forming the difference between OCT A-scan envelope signals with and without excitation pulses, depth resolved images with optical absorption contrast are generated. To demonstrate the proof of principle of this method we perform simulations which build on our

previously validated models of the PARS detection mechanism which were presented in chapters 3 and 4.

The proposed approach is not to be confused with previous OCT-based photoacoustic detection methods which aimed to detect outward propagating acoustic waves manifesting themselves as subtle oscillations at the sample outer surface [79–82]. Instead our approach locally detects optical-absorption-induced initial pressures directly at their sub-surface origins. These effects have been demonstrated in modeling and experiments to be substantial. For example, in [2] red blood-cell scattering cross sections were observed to change by greater than 5% when illuminated with pulses of mere nJ energies. We propose using a pulsed low-coherence source spectral-domain optical coherence tomography (SD-OCT) method, which enables full A-scan acquisitions without mechanical depth-scanning, reference-beam scanning or swept-source wavelength-scanning. This approach also offers high signal-to-noise [117]. Our proposed method which we call coherence gated photoacoustic remote sensing microscopy (CG-PARS) would involve replacing the standard PARS detection pathway with a pulsed low-coherence interrogation beam, low-coherence interferometer and a spectrometer to capture the nanosecond-scale absorption-induced changes in refractive index. The presented results demonstrate the potential of the proposed method and illustrate the importance of key design parameters.

6.1 Coherence-gated PARS detection[1]

The proposed detection process behind CG-PARS is effectively similar to the process used for SD-OCT. The primary difference is that ns-scale time-dependent effects must now be captured. The recovery of a SD-OCT reflectivity envelope in depth $r_s(\ell_s, t)$, where ℓ_s and t are the scattering depth and time respectively, is well known [34] and can be related to the reflectivity spectrum $I(\nu, t)$, where ν is the optical frequency, captured on a spectrometer through a Fourier transform. One way to form a CG-PARS image is to capture the modulation $\Delta I(\nu, t)$ due to an excitation pulse, then relate

[1] The following section was taken from [4]

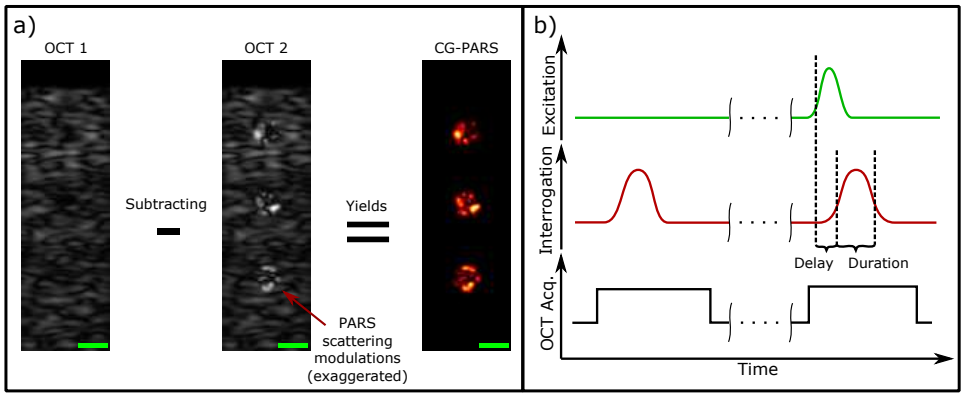

Figure 6.1: Several key aspects of the detection mechanism are highlighted. (a) Shows of the central idea behind CG-PARS detection where two OCT acquisitions are subtracted from each other to highlight regions of optical absorption. In this example, OCT_1 represents an unperturbed acquisition of the optical scattering distribution, and OCT_2 represents the same region directly following an excitation event where regions have been modulated through the PARS mechanism. The difference then highlights these modulated regions. Scale bars: 50 μm. (b) Shows the relative timing between the excitation pulse (green), interrogation pulses (red), and the activity of the OCT detection array. Of particular importance is the relative delay, and the duration of the second interrogation pulse relative to the excitation pulse.

this to a time-sequence of OCT A-scans. This could be accomplished using a photodiode array in the spectrometer rather than a CCD-based spectrometer although it would require a multi-channel data acquisition system and dense photodiode array. CCD cameras themselves do not typically have the temporal bandwidth to capture required modulations. Even rapid SD-OCT systems with low MHz-range A-scan rates [118] yield total integration times which are substantially longer than the 10 ns to 50 ns time-domain behavior experimentally observed with the PARS mechanism. To overcome this issue a pulsed detection scheme is proposed, and is the focus of this chapter.

By appropriate timing of the interrogation pulses a relatively slow detection array can be forced into capturing brief reflectivity perturbations within the sample. Specifically an acquisition is made with the unperturbed sample and then again directly after an excitation event (Fig. 6.1). Each of these i intensity spectra then relate to a given estimate of the stationary reflectivity distribution $\hat{r}_{s,i}(\ell_s)$, which individually represent SD-OCT A-scan acquisitions after taking their envelopes. Subtracting two appropriate envelopes may then highlight modulation in the local scattering distribution, which is primarily attributed to PARS modulation and therefore implies optical absorption proportionality in the A-scan envelope-detected difference signal $b(z)$, represented as

$$b(z) = ||\mathcal{H}\{\hat{r}_{s,1}\}| - |\mathcal{H}\{\hat{r}_{s,2}\}|| \tag{6.1}$$

Here $|\mathcal{H}|$ represents the the magnitude of the Hilbert transform, an envelope-detection operation.

The expected behavior for this process is highlighted in Fig. 6.2. Objects which have optical scattering contrast will be visualized through the individual OCT acquisitions. Objects which have optical absorption contrast may then be recovered through the difference between a perturbed scattering profile and one which has not yet undergone photoacoustic excitation.

One key aspect of CG-PARS over conventional PARS microscopy involves the acquisition time needed to acquire full B-scans and volumetric C-scans (Fig. 6.3). Within two laser pulse events CG-PARS can provide full

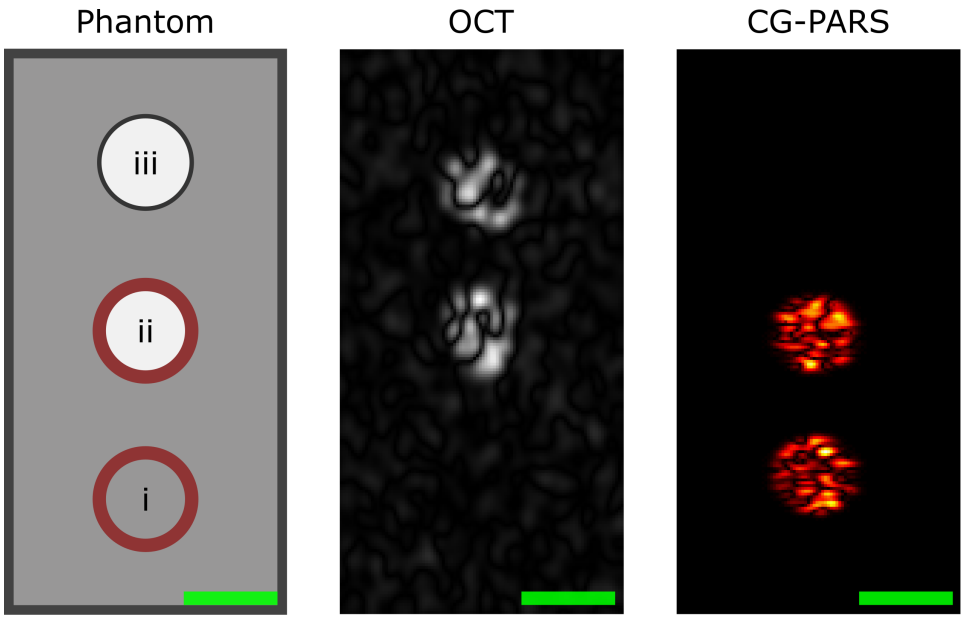

Figure 6.2: An example of simulated contrast performance. Here three targets are placed inside a scattering medium where (i) is a purely absorbing target, (ii) is both absorbing and scattering, and (iii) is a purely scattering target. OCT has sensitivity to the optically scattering regions, and CG-PARS has sensitivity to the optical absorption. Note that since CG-PARS is also reliant on the optical scattering for signal, the absorption of target (i) must be larger than that of target (ii) to produce similar CG-PARS signal. Scale bars: 100 μm.

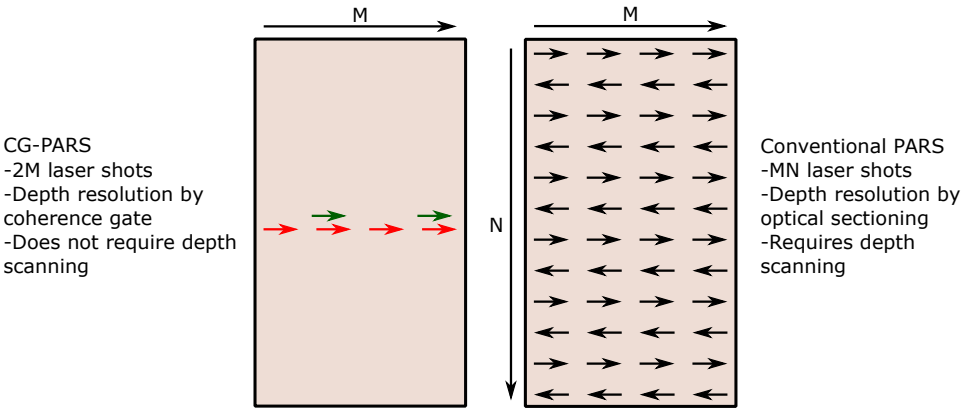

Figure 6.3: A comparison between the scanning patterns of the newly proposed CG-PARS and conventional PARS microscopy. Since CG-PARS is capable of acquiring full depth-resolved A-scans within two laser pulse events only $2M$ laser shots are required to perform a B-scans. Conventional PARS however, requires MN laser shots to characterize the same region.

depth-encoded A-scans and it does not necessitate depth scanning, whereas PARS only yields a small region defined by the optical section for a given acquisition event. This requires depth scanning with conventional PARS yielding significantly higher acquisition times.

6.2 1D Simulation[2]

The first proposed approach for modeling these effects involves an effective 1D simulation. Much of this work follows closely from previous efforts on modeling the time-evolution of PARS signals due to pulsed absorption-based reflectivity changes and scattering cross section modulations of planar and spherical scatterers, respectively [1, 2]. First, for a spacial coordinate $\mathbf{x} = (x, y, z)$ we consider a sample with a spatially-varying refractive index profile $n_0(\mathbf{x})$, optical absorption at the excitation wavelength $\mu_a(\mathbf{x})$, and constant acoustic propagation velocity v_s. This region is then illuminated with a Gaussian beam having an intensity distribution $I_{ex}(\mathbf{x}, t)$. We then assume a

[2]The following section was taken from [4]

thermal confinement condition such that the local heating within the region can be approximated as $H(\mathbf{x},t) \approx \mu_a(\mathbf{x}) I_{ex}(\mathbf{x},t)$ for unity Gruneisen parameter. This is used as a source term within the inviscid photoacoustic equation to find the pressure field $p(\mathbf{x},t)$ following $\nabla^2 p - \left(1/v_s^2\right) p_{tt} = -(\beta/C_p) H_t$ where ∇^2 is the Laplacian, β is the thermal coefficient of volume expansion, and C_p is the specific heat capacity at constant pressure [34]. Here a subscript t denotes a temporal derivative, and two such subscripts denote the second derivative in time.

Simulation of this problem is performed through explicit finite-difference numerical methods which are well summarized in many other works [119, 120]. In brief, we discretized the photoacoustic equation components as

$$\begin{aligned}\nabla^2 p(\mathbf{x},t) \approx & \frac{p^n_{i-1,j,k} - 2p^n_{i,j,k} + p^n_{i+1,j,k}}{(\Delta x)^2} + \cdots \\ & \frac{p^n_{i,j-1,k} - 2p^n_{i,j,k} + p^n_{i,j+1,k}}{(\Delta y)^2} + \frac{p^n_{i,j,k-1} - 2p^n_{i,j,k} + p^n_{i,j,k+1}}{(\Delta z)^2}\end{aligned} \tag{6.2a}$$

$$\frac{\partial^2 p(\mathbf{x},t)}{\partial t^2} \approx \frac{p^{n+1}_{i,j,k} - 2p^n_{i,j,k} + p^{n-1}_{i,j,k}}{(\Delta t)^2} \tag{6.2b}$$

$$\frac{\partial H(\mathbf{x},t)}{\partial t} \approx \frac{H^{n+1}_{i,j,k} - H^n_{i,j,k}}{\Delta t} \tag{6.2c}$$

where $H^n_{i,j,k} = \mu_a(\mathbf{x})\Phi(\mathbf{x},t)$ is known from the excitation fluence distribution $\Phi(\mathbf{x},t)$, and the discretization is performed as $x = i\Delta x$, $y = j\Delta y$, $z = k\Delta z$, $t = n\Delta t$. This yields an update equation of the form

$$\begin{aligned}p^{n+1}_{i,j,k} = (\Delta t)^2 \Bigg[& \frac{\beta}{C_p} \frac{H^{n+1}_{i,j,k} - H^n_{i,j,k}}{\Delta t} + c_a^2 \Bigg(\frac{p^n_{i-1,j,k} - 2p^n_{i,j,k} + p^n_{i+1,j,k}}{(\Delta x)^2} + \cdots \\ & + \frac{p^n_{i,j-1,k} - 2p^n_{i,j,k} + p^n_{i,j+1,k}}{(\Delta y)^2} + \frac{p^n_{i,j,k-1} - 2p^n_{i,j,k} + p^n_{i,j,k-1}}{(\Delta z)^2} \Bigg) \Bigg] + \cdots \\ & 2p^n_{i,j,k} - p^{n-1}_{i,j,k}\end{aligned} \tag{6.3}$$

Apart from conventional stability condition where $c_a^2(\Delta t)^2 < (\Delta x)^2 +$

$(\Delta y)^2 + (\Delta z)^2$, consideration here must also be given to the desired pulse-width of the excitation laser such that at minimum the Nyquist sampling criteria is satisfied.

The photoacoustic pressure may be significantly large to generate non-trivial modulations in the refractive index profile such that optical scattering changes from the excited region are detectable. This process follows the elasto-optic relation [85]

$$n^*(\mathbf{x}, t) = n_0(\mathbf{x}) + \delta n(\mathbf{x}, t) = n_0 + \frac{\epsilon n_0^3 p}{2\rho_m v_s^2} \tag{6.4}$$

where ϵ is the elasto-optic coefficient ($\epsilon \approx 0.32$ for water [121, 122]) and ρ_m is the mass density. As mentioned in the previous section, rather than simulating a continuous-wave interrogation beam, a pulsed detection scheme is used. Since it will be of interest to track phase fronts for coherence considerations, the full electric field of the interrogation beam is considered within the region. As with the excitation beam, an ideal Gaussian is used to represent the interrogation pulse intensity profile. This approximation is of course not valid in general (particularly at depth) so we limit consideration to within the minimum transport mean free path of both wavelengths. Since it would require substantial computational power to now simulate the full three-dimensional electromagnetic field of the interrogation interaction with the sample, the dimensionality of the problem is reduced to one by taking a weighted sum across regions of equal phase such that the resulting equivalent linear refractive index profile $\bar{n}^*(z, t)$ is given by

$$\bar{n}^*(z, t) = \frac{\sum\limits_{\mathbf{x} \in \Psi(z)} I_{int}(\mathbf{x}, t) n^*(\mathbf{x}, t)}{\sum\limits_{\mathbf{x} \in \Psi(z)} I_{int}(\mathbf{x}, t)} \tag{6.5}$$

where Ψ represents regions of equal phase such that

$$\Psi(z) = \{\mathbf{x} | \phi(z) \leq \phi(\mathbf{x}) < \phi(z + \Delta z)\} \tag{6.6}$$

where $\phi(\mathbf{x})$ is the local phase. Given that we restrict the use of this simulation to low numerical aperture values ($NA < 0.1$), the electric field distri-

bution of the interrogation beam should be reasonably cylindrical about the optical axis over the considered region. The resulting one-dimensional refractive index profile will provide some reflected complex electric field spectrum $E_s(\nu, t)$ which will dictate the relative amplitude reflection and accumulated phase of each wavelength. This is obtained using a transfer-matrix method detailed in [1](Ch. 3).

The back-reflected interrogation light from the sample is compared with a reference path with a low-coherence interferometer. The electric field which is back-reflected from the sample $E_s(\nu, t)$ is compared with that of the reference arm $E_r(\nu, t)$, represented as

$$E_r(\nu, t) = E_{0,r}(\nu)e^{i[4\pi\nu\Delta\ell_r/c]}, \tag{6.7}$$

where $\Delta\ell_r$ is the reference path-length. These two beams are allowed to interfere, and are spectrally separated within a spectrometer where the final measured time-varying intensity spectra will be defined by $I_i(\nu) = \int_{int_i} |E_s + E_r|^2 dt$ for the i^{th} interrogation pulse. Two relevant intensity spectra can then be processed to form a CG-PARS A-line following section 6.1.

6.3 CG-PARS Linear Shift-Variant model[3]

The previous approach is an approximate method for reducing the OCT and CG-PARS modeling problem to 1D. It allows investigation of the temporal evolution of the PARS signals and is most accurate for planar structures. An alternate approach for more general geometries and used for validation is to consider a linear shift-variant (LSV) point-spread function (PSF) model, which will then be further simplified to a convolution-based shift invariant approximation.

[3]The following section was taken from [4]

6.3.1 OCT

In the absence of noise, the complex OCT signal as a function of image space coordinate $\mathbf{x} = (x, y, z)$ can be written as [123–125]

$$S_{OCT}(\mathbf{x}) = \int h_{OCT}(\mathbf{x}, \mathbf{x}')r(\mathbf{x}')d\mathbf{x}' \tag{6.8}$$

The displayed signal is usually the envelope or complex magnitude, $|S_{OCT}|$. Here r is the amplitude reflectivity distribution.

For a planar interface $r(\mathbf{x})$ can be represented as a Fresnel reflectivity. For an isotropic-scattering point target, $r(\mathbf{x}) = r_0\delta(\mathbf{x} - \mathbf{x_0})$, where r_0 relates to the scattering cross-section [2]. In general a more complex target can be considered a superposition of such point targets.

When the interrogation source is focused on illumination and detection, the point-spread function can be modeled as:

$$h_{OCT}(\mathbf{x}, \mathbf{x}') = 2E_R E_{S_0} h^2_{E,int}(\mathbf{x}, \mathbf{x}')R_{zz}(z - z') \tag{6.9}$$

Here $h_{E,int}$ is the shifted normalized electric field of a focused beam, E_R is the amplitude of the reflected the electric field along the reference arm, and E_{S_0} is the incident electric field amplitude on sample. $h_{E,int}$ is squared in the above expression to denote focusing on illumination and detection. R_{zz} is the axial autocorrelation function that represents coherence-based depth-gating.

When the interrogation source is a focused Gaussian beam in a minimally-scattering medium or at a depth where ballistic light transport dominates, $h_{E,int}$ can be modeled as:

$$h_{E,int}(\mathbf{x}, \mathbf{x}') = \frac{w_0}{w(z_f)} \exp\left(-\frac{\rho^2(\mathbf{x}, \mathbf{x}')}{w(z_f)^2}\right) \exp\left(-i\left(k(z_f) + k\frac{\rho^2(\mathbf{x}, \mathbf{x}')}{2R(z_f)} - \psi(z_f)\right)\right) \tag{6.10}$$

where $w(z) = w_0\sqrt{1 + (z/z_R)^2}$ is the depth-dependent beam waist,

$R(z) = z\sqrt{1 + (z_R/z)^2}$ is the radius of curvature of the wavefront, $\psi(z) = \arctan(z/z_R)$ is the Guoy phase, $z_R = \pi w_0^2 \nu/c$ is the Rayleigh range, $z_f = z - f$ with f as the focal depth, $k = 2\pi n\nu/c$ is the wavenumber, and $\rho^2(\mathbf{x}, \mathbf{x}') = (x - x')^2 + (y - y')^2$ is the square of the radial spatial coordinate. In a scattering medium, $h_{E,int}$ is more difficult to compute, but for an incoherent source, Monte Carlo methods could be used to model the response to a Gaussian beam focusing into tissue [126].

When the interrogation source has a Gaussian power-spectral density, the autocorrelation function is a Gaussian modulated sinusoid as given by Eq. 9.38 of [34]. For frequency-domain systems, signals are recorded in the spectral domain and inverse-transformed to the spatial domain, with filtering to remove the modulations. In this case, a model for the effective autocorrelation function is simply

$$R_{zz}(z) = \exp\left(-\frac{z^2}{2\sigma_z^2}\right). \tag{6.11}$$

If within the depth of focus, we take $w(z)$, $R(z)$ and $\psi(z)$ as roughly constant so that S_{OCT} can be approximated as a linear shift-invariant (LSI) model of the form

$$S_{OCT,LSI}(\mathbf{x}) = h_{OCT,LSI}(\mathbf{x}) * r(\mathbf{x}) \tag{6.12}$$

where

$$h_{OCT,LSI}(\mathbf{x}) = 2E_R E_{S0} \exp\left(\frac{-2\rho^2}{w_0^2}\right) \exp\left(-i2kz\right) \exp\left(-\frac{z^2}{2\sigma_z^2}\right) \tag{6.13}$$

The shift-variant approach offers the power to study highly focused beams whereas the shift-invariant model is more suitable for looser focusing and offers intuition and fast simulation performance.

When performing speckle simulations, statistically-independent normally-distributed random fields may be chosen for the real and imaginary parts of r, in which case the resulting speckle statistics for $|S|$ are Rayleigh dis-

tributed [127] for both the LSV and the LSI models as expected for fully-developed OCT speckle.

6.3.2 PARS

To model PARS as a linear system, we express the PARS signal as

$$S_{PARS}(\mathbf{x}) = \int h_{PARS,int}(\mathbf{x}, \mathbf{x}')\Delta r_I(\mathbf{x}, \mathbf{x}')d\mathbf{x}' \tag{6.14}$$

where, ignoring scattering,

$$h_{PARS,int}(\mathbf{x}, \mathbf{x}') = |E_{S0}|^2|h_{E,int}(\mathbf{x}, \mathbf{x}')|^4 \tag{6.15}$$

where the fourth power represents two-way focusing of an intensity distribution and where Δr_I is the perturbation in the intensity reflection coefficient. It has been shown [1, 3] that the intensity reflectivity is proportional to the perturbation of the refractive index ($\Delta r_I \propto r\delta n$), and that the perturbation relates to the optical absorption and the optical fluence distributions such that

$$\delta n(\mathbf{x}, \mathbf{x}') = \frac{\Gamma\eta n^3}{2\rho_m v_s^2}\mu_a(\mathbf{x}')\phi_{ex}(\mathbf{x}, \mathbf{x}') \tag{6.16}$$

where $\phi_{ex}(\mathbf{x}, \mathbf{x}')$ is the excitation fluence distribution. It may be modeled as $\phi_{ex} \propto I_{ex,0}|h_{E,ex}|^2$ with $I_{ex,0}$ being the maximum excitation intensity. Here the amplitude shape function $h_{E,ex}(\mathbf{x}, \mathbf{x}')$ may be considered as the same form of $h_{E,int}(\mathbf{x}, \mathbf{x}')$ with appropriate wavelength substitutions. This would yield an expression of the form

$$S_{PARS}(\mathbf{x}) \propto |E_{S0}|^2 I_{ex,0} \int |h_{E,int}(\mathbf{x}, \mathbf{x}')|^4|h_{E,ex}(\mathbf{x}, \mathbf{x}')|^2\mu_a(\mathbf{x}')r(\mathbf{x}')d\mathbf{x}'. \tag{6.17}$$

However, since the focal depth is scanned throughout the target such that $f = z'$, if we assume local shift invariance, we can write an LSI expression as

$$S_{PARS,LSI}(\mathbf{x}) \propto |h_{E,int}(\mathbf{x})|^4 |h_{E,ex}(\mathbf{x})|^2 * \mu_a(\mathbf{x}) r(\mathbf{x}). \tag{6.18}$$

6.3.3 CG-PARS

The CG-PARS signal distribution will be considered the difference between a perturbed S_{OCT} envelope signal with an unperturbed one such that

$$S_{CG-PARS}(\mathbf{x}) = ||S_{OCT}(\mathbf{x})| - |S_{OCT} + \Delta S_{OCT}|| \tag{6.19}$$

where $\Delta S_{OCT}(\mathbf{x})$ can be represented as

$$\Delta S_{OCT}(\mathbf{x}) = E_R E_{S0} I_{ex,0} \int h^2_{E,int}(\mathbf{x}, \mathbf{x}') R_{zz}(\mathbf{x}, \mathbf{x}') |h_{E,ex}(\mathbf{x}, \mathbf{x}')|^2 \mu_a(\mathbf{x}') r(\mathbf{x}') d\mathbf{x}' \tag{6.20}$$

For primarily real positive signals, this expression becomes

$$S_{CG-PARS}(\mathbf{x}) \approx \Delta S_{OCT}(\mathbf{x}) \tag{6.21}$$

This illustrates that CG-PARS detects optical absorption by measuring changes in OCT signal induced by a pulsed excitation beam.

If the LSI approximation can additionally be used, the expression can be further reduced as

$$S_{CG-PARS,LSI}(\mathbf{x}) \propto h_{OCT,LSI}(\mathbf{x}) h_{EX,LSI}(\mathbf{x}) * \mu_a(\mathbf{x}) r(\mathbf{x}) \tag{6.22}$$

where

$$h_{EX,LSI}(\mathbf{x}) = I_{ex,0} \exp\left(-\frac{2\rho^2}{w_0^2}\right) \tag{6.23}$$

is the LSI excitation distribution.

6.4 Simulations and Results[4]

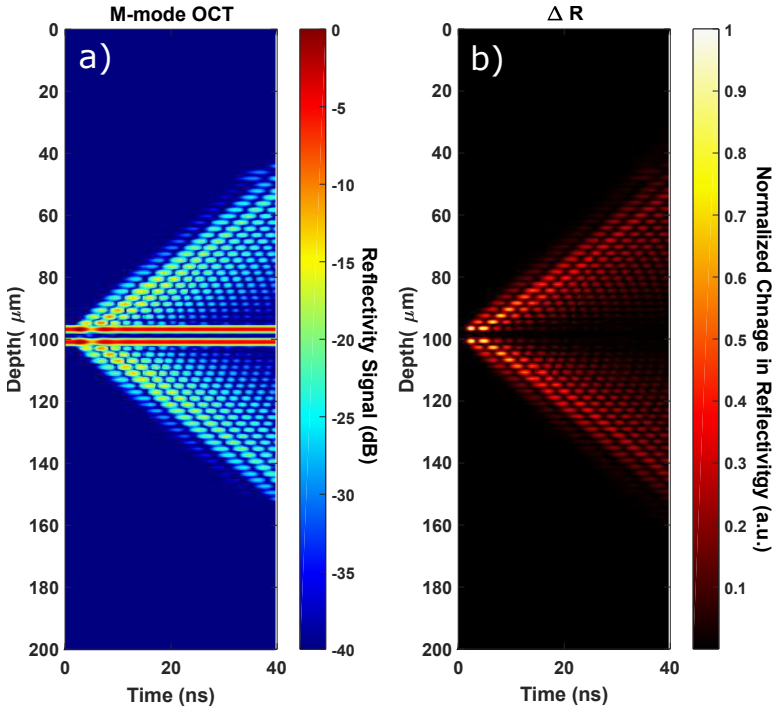

Figure 6.4: An example of a CG-PARS interaction with a optically absorbing and optically scattering regions. (a) Highlights the reflectivity signal in depth with time. (b) shows the change in the reflectivity profile.

6.4.1 Temporal evolution of PARS modulations

First the 1D model is used to examine the temporal effects discussed in section 6.1 by simulating a single OCT A-scan repeated at multiple time-delays following a photoacoustic excitation event (Fig. 6.4(a)). We refer to this as an M-mode OCT acquisition. Here a 4 μm diameter tube with optical absorption of $\mu_a = 250$ cm^{-1} and a mean refractive index $n = 1.41$ (to provide a blood-like target) is simulated within a homogeneous non-absorbing medium ($n = 1.33$). The simulation is performed assuming an interroga-

[4]This section was taken from [4]

tion beam with central wavelength $\lambda = 1310$ nm, and spectral bandwidth $\Delta\lambda = 85$ nm which gives a free-space full-width at half maximum (FWHM) coherence length of 8.9 μm. Figure 6.4(a) shows the reflectivity signals in time where the out-propagating acoustic waves are clearly visible for an excitation event at time $t = 0$. Then, if all subsequent time points ($t > 0$) are subtracted from the unperturbed profile ($t = 0$) (Fig. 6.4(b)) the change to the reflectivity profile (ΔR) is highlighted. It can be seen that following the excitation event the targets are perturbed to a significant degree, but the acoustic propagation has not yet distorted the original object. This is the aspect which CG-PARS is attempting to capture. However, the timescales necessary (∼ns) are currently not obtainable by modern OCT devices. This then motivates the use of a short pulse for interrogation. This implementation should allow for precise timing and duration of the acquisition events. As well, using a pulsed interrogation allows for higher peak intensities and previous work has demonstrated large signal-to-noise ratios (∼ 100dB) [128]. This dynamic range may be necessary for weak modulation signals.

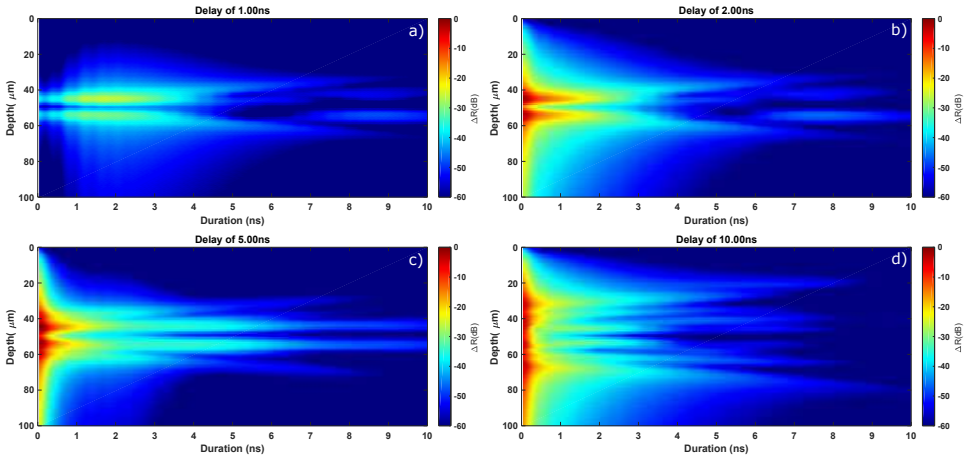

Figure 6.5: The effects of various interrogation timing parameters are highlighted. The target is a homogeneous absorbing region between 40 and 60 μm in depth.

These results also highlight the importance and potential impact when selecting the relative delay and duration of the secondary interrogation pulse

which directly follows the excitation event. To examine the effects of these parameters, a study is performed observing a single A-scan for a homogeneous absorbing region (Fig. 6.5). Here, it is quite obvious that if the interrogation is made too early then a yet unperturbed profile may be examined (Fig. 6.5(a)). If the interrogation is made too late then undesirable non-localized signal artifacts may be recovered resulting from the out-propagating acoustic waves (Fig. 6.5(c), 6.5(d)). This could result in artificial broadening of the target and reduce CG-PARS signal contrast. The duration of the interrogation should be sufficiently long to provide adequate sensitivity, but not so long as to also capture out-propagating acoustic waves. Despite our efforts here, the precise values of these will likely require tuning for a given experiment.

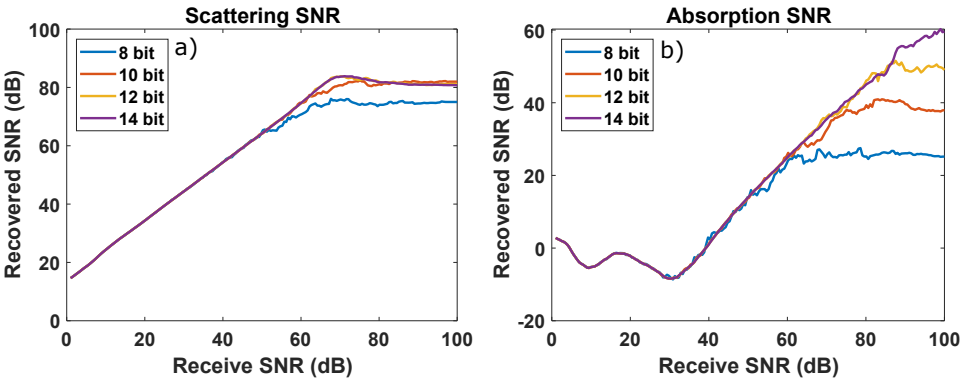

Figure 6.6: The effects of various receive SNR values for (a) The recovered SNR of the produced scattering A-scans and (b) The recovered SNR of the produced absorption A-scans.

6.4.2 Effects of Receive SNR and Discretization Error

Perhaps one of the most critical components to investigate here in terms of the potential feasibility of the proposed device involves a study of the required detector sensitivity compared to their noise vs. what might be expected from the recovered image (Fig. 6.6). Although there will be a significant number of possible noise sources throughout the system, two large

components are likely to be the receive sensitivity of the detector array elements, and additional errors brought on through analog-to-digital readout of these elements. Studies were performed by imaging a single homogeneous 10μm thick absorbing layer for various receive bit discretization (from 8-bit to 14-bit) and for various receive element SNR values (1 dB to 100 dB). The results of these are summarized in graphs (Fig. 6.6(a), Fig. 6.6(b)) where the recovered scattering SNR (OCT) is included for comparison. For these particular values (where the mean absorption of the region is taken as 250 cm$^-$1, the 532 nm excitation pulse energy is 25 nJ), the maximum recovered scattering SNR is near $\sim$90 dB which is consistent from reported values for pulsed-detection OCT systems [128]. The recovered absorption SNR by comparison seems to have taken values roughly $\sim$20 - 30 dB lower. However, this limitation may not be problematic given available hardware. For example in [129] an OCT device was constructed with an OCT spectrometer with available pixel sensitivity of 66 dB and a 12-bit ADC. This would yield a predicted recovery of around 34 dB for CG-PARS. CG-PARS will require some minimum level of sensitivity in the OCT detection to achieve practical signal-to-noise which may limit its performance at depth in scattering media.

6.4.3 Contrast Mechanism

PARS contrast is already discussed in our previous papers, but has previously not been investigated for CG-PARS. Contrast behavior is highlighted in Fig. 6.2. Three different types of targets are situated within a scattering phantom, and their responses are simulated using the LSV method described in section 6.3. Targets with optical absorption (i-ii) are detected with CG-PARS whereas those with optical scattering (ii-iii) can be recovered using the OCT acquisition which is also provided by the technique. Targets are 80 μm cylindrical regions within a discreet random media background with optical reflectivity variance of 2×10^{-4} and no optical absorption. Methods for calculating more precise values for the scattering variance distributions have been discussed [130] but are not used here. The targets themselves

have amplitude reflectivity variances of $\sigma^2_{r,i} = 0$, $\sigma^2_{r,ii} = 1 \times 10^{-3}$, and $\sigma^2_{r,iii} = 1 \times 10^{-3}$, and mean optical absorption $\mu_{a,i} = 250$ cm^{-1}, $\mu_{a,ii} = 50$ cm^{-1}, and $\mu_{a,iii} = 0$ cm^{-1} respectively. The region is again simulated using an interrogation beam with central wavelength $\lambda_0 = 1310$ nm, and spectral bandwidth $\Delta\lambda = 85$ nm, and Gaussian waist with $NA = 0.02$. Since CG-PARS has sensitivity to the inherent reflectivity profile of the region, the absorption of target (i) needs to be significantly higher than that of target (ii) to provide similar CG-PARS signal. This is a preexisting trait of the PARS mechanism. However, biological tissues tend to be highly heterogeneous in their microscale optical properties, and thus are likely to provide a large degree of optical scattering. Indeed this limitation has not been problematic for conventional PARS microscopy. This is not to be interpreted as a requirement for speckle contrast such as that required by OCT. Rather, the CG-PARS approach only requires optical absorption contrast and some degree of inherent scattering from the material. For example, a blood vessel may be indistinguishable by conventional OCT providing similar speckle characteristics to the surrounding tissue. CG-PARS may then overcome this issue through visualization of the optical absorption contrast.

6.4.4 PARS Experimental Comparison

Prior to demonstrating the potential advantages of CG-PARS over PARS, B-scan point-spread functions from PARS systems are compared with PSF models. The PARS LSV model (Sec. 6.3.3) is compared against experimental B-scans results (Fig. 6.7). The experimental system used is similar to that provided in [3]. In brief, a 532-nm ns-pulsed excitation is co-focused with a 1310-nm continuous-wave super luminescent diode (SLD) with spectral bandwidth of $\Delta\lambda = 45$ nm. Focusing is provided by a $NA = 0.4$ objective lens which is assumed to provide $NA \approx 0.2$ when considering the effective focal length $f = 10$ mm, and input beam diameter $d \approx 4$ mm. Experimental results are acquired by performing several sequential C-scan maximum amplitude projections (MAP) at 22 progressive depths (with a 25 μm step-size) using a translation stage. The phantom used consisted

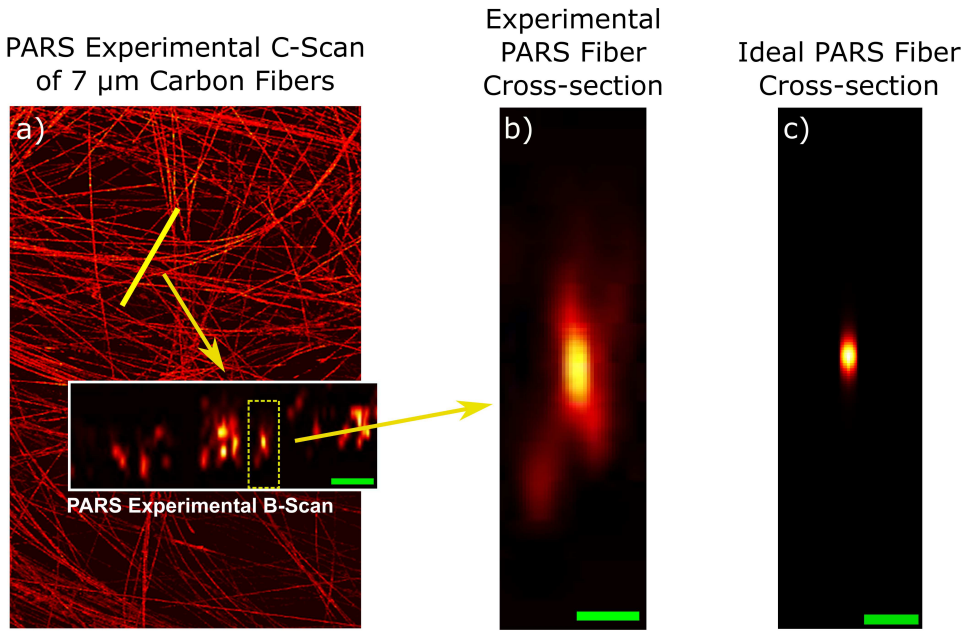

Figure 6.7: A comparison between PARS experimental B-Scans and simulation results. (a) PARS C-Scan maximum intensity projection of 7μm carbon fibers along with a (inset) representative experimental B-Scan (scale bar: 100 μm) and (b) a representative cross-section of a single fiber (scale bar: 25 μm). B-scans were pulled from volumetric data, where multiple maximum-amplitude C-scans were acquired at various depths. (c) A PARS LSV simulation of a cylindrical absorber with diameter 7 μm situated within a non-scattering medium (using $n = 1.33$). Scale bar: 25 μm.

of a network of 7 μm carbon fibers suspended in clear gelatin at various depths. If we compare with the ideal performance for such a structure (Fig. 6.7(c)) simulated using the LSV PARS model (Sec. 6.3.2) there exists some discrepancy likely attributed to misalignment between the excitation and interrogation focii and potentially heterogeneity within the medium. These problems further highlight the need for coherence gating to improve depth-resolution.

6.4.5 Point Spread Functions

The point-spread functions (PSFs) for the 1D CG-PARS simulation and LSV model are shown in Figs. 6.8(a) and 6.8(b). Here a low numerical aperture is used similar to that seen in OCT providing reduced lateral performance but greater depth-of-focus. The detection source stimulated again has a $\lambda_0 = 1310$ nm central wavelength with a $\Delta\lambda = 85$ nm spectral bandwidth. Both models agreed reasonably with each other in particular with predicted axial performance. As a final comparison, a conventional PARS visualization is simulated using the LSV model on the same target (Fig. 6.8(c)). If the same numerical aperture ($NA = 0.02$) is used, the points are not well recovered as conventional PARS microscopy relies on optical sectioning for axial resolution. Here a substantially larger numerical aperture is necessary to provide the same axial performance (Fig. 6.8(d)), however experimental results thus far suggest that this represents a highly idealized situation which is unlikely to occur deep within scattering phantoms and *in vivo*. It is also important to note that conventional PARS necessitates depth scanning and thus may require a significantly higher acquisition times. For example, if scanning a 1mm deep and 2mm wide region with respective step sizes of 4 μm and 2 μm yields B-scan frame rates of 1 fps for conventional PARS and 250 fps for CG-PARS assuming a 500kHz laser pulse rate.

6.4.6 Scattering Phantom Simulations

Next, a more complex phantom is simulated using the LSV model (Fig. 6.9). Several blood-vessel-like structures are placed within a scattering phantom

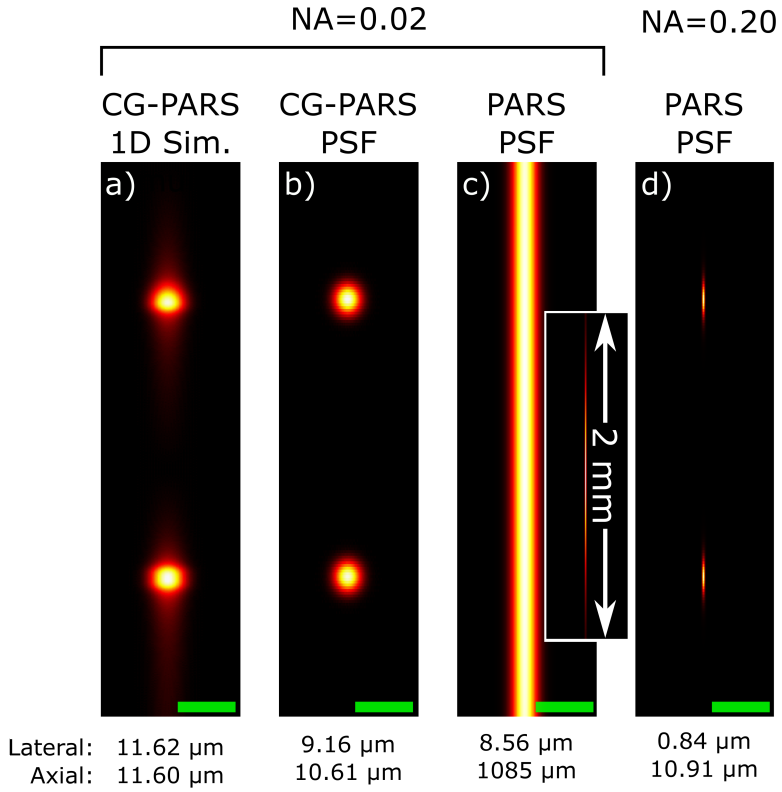

Figure 6.8: A comparison between (a) the CG-PARS 1D simulation (Sec. 6.2), (b) the CG-PARS LSV model (Sec. 6.3.3), and (c-d) the PARS LSV model (Sec. 6.3.2). The 1D simulation and the LSV model in (a) and (b) agree well with each other in terms of predicted axial and lateral resolutions. Conventional PARS performs extremely poorly with the same optical setup as it can only provide axial resolution as defined by the optical section. If a higher numerical aperture is used ($NA = 0.2$) the axial resolution would improve, however, alignment issues and optical scattering may confound this. In the above simulations, phantoms consist of two point targets which are situated within a non-scattering medium ($n = 1.33$). The first numerical aperture ($NA = 0.02$) is typical of commercially available OCT systems and is assuming a effective focal length of 100 mm and a input beam diameter of 4 mm. Interrogation is performed using a pulsed source with 1310 nm central wavelength and 85 nm spectral bandwidth. Scale bars represent 25 μm.

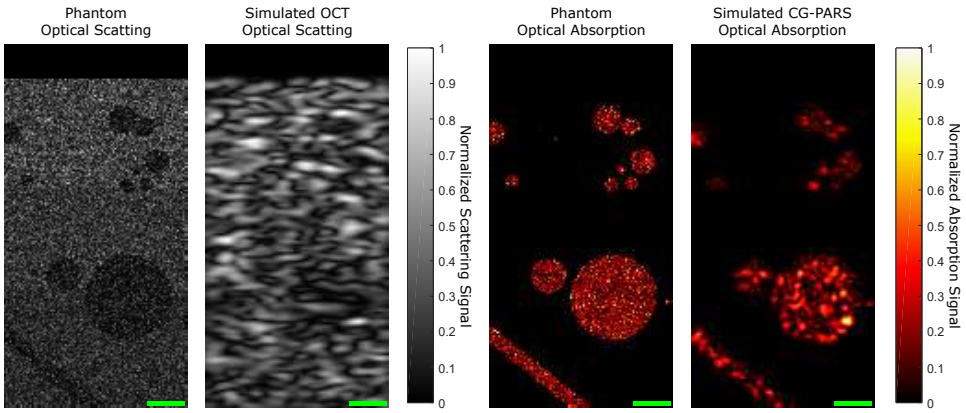

Figure 6.9: A more complex phantom a simulated using the LSV model detailed in section 6.3. (a) Shows the optical scattering distribution of the phantom and the recovery provided by (b) conventional OCT. (c) shows the optical absorption distribution of the phantom and the recovery provided by (d) CG-PARS. Scale bars: 50μm.

with two different scattering layers. Despite the subtle contrast which can be seen in the ground-truth phantom (Fig. 6.9(a)) the structures are not significantly recovered through simple OCT methods. It is worth noting that other OCT methods such as OCT angiography and visible OCT would likely perform better here at recovering the vessel structures. CG-PARS offers improved recovery of these structures relative to OCT due to the optical absorption contrast available. Within highly scattering targets such as skin or brain tissue CG-PARS may offer structural visualization complimenting that provided by OCT.

6.5 Discussion[5]

The proposed coherence-gated photoacoustic remote sensing (CG-PARS) modality offers potential benefits over conventional PARS microscopy in terms of improved axial performance and acquisitions speeds. It also offers complementary absorption contrast to the scattering contrast offered

[5]This section was taken from [4]

by coherence-gated methods such as OCT. By enabling full depth-resolved acquisitions CG-PARS may be the path forward towards creating a fully functional non-contact optical resolution photoacoustic modality which may offer competitive functionality to conventional OR-PAM. The predicted linear behavior of the recovered signal to the optical absorption may enable spectral unmixing capabilities for measurement of blood oxygen saturation and molecular reporters. Future work should include the design and construction of an experimental apparatus to realize these predictions. Such systems will require careful attention to interrogation pulse duration and timing relative to excitation pulses. Adequate sensitivity and dynamic range will also prove critical.

The present work represents a first investigation of coherence-gating for photoacoustic remote sensing and may provide a simulation platform for achieving optimal experimental design. This paper also introduces important point-spread function representations which will be beneficial for system modeling and for guiding design.

6.6 Conclusion[6]

Preliminary work regarding a new non-contact photoacoustic modality called CG-PARS was presented. Here, CG-PARS interactions were simulated with several approaches. This method offers the promise of overcoming many limitations with current competing techniques such as conventional PARS microscopy, OR-PAM, OCT, and visible-OCT. The ability to perform complete A-scan acquisitions offers significant speed benefits over voxel-based scanning provided by conventional PARS. Like conventional PARS, there exists the ability to select appropriate wavelengths for both excitations and detection which could provide greater penetration depths than those available to OR-PAM. Since CG-PARS contrast is proportional to optical absorption, future work may realize functional imaging of oxygen saturation and molecular imaging of reporters to provide information complementary

[6]This section was modified from [4]

to optical coherence tomography. CG-PARS presents exciting possibilities for the future of optical absorption microscopy.

Chapter 7

Conclusions

PARS microscopy represents a powerful new field in optical imaging capable of recovering optical absorption contrast with sub-micron scale resolution from within turbid media. Moreover it accomplishes this while operating as a reflection-mode device suitable for imaging thick samples. This architecture makes PARS suitable for *in-situ* imaging of larger specimens, potentially even suitable for future clinical implementations. As with other photoacoustic devices, the ability for PARS techniques to visualize optical absorption contrast enables label-free operation for a wide variety of targets seen in biology such as DNA, RNA, cytochrome, hemoglobin, melanin, and lipids to name a few. The addition of exogenous labels could be used to provide further contrast and functional information. The linear relationship between the measured PARS signal and the optical absorption facilitates multiplex imaging of multiple chromophores allowing for label free functional information to be acquired such as blood oxygen saturation.

7.1 The PARS mechanism

7.1.1 Contributions

Work on the PARS mechanism was primarily lead by the author who was the primary contributor with regards to developing and testing the mathematical models, designing and performing simulations, and performing rele-

vant experimental validations. The original concept for the PARS detection method was first proposed in [3] which suggested the simple two-state model presented in the first report. This idea was expanded upon by the author to account for for complex geometry and time-evolution.

7.1.2 Discussion

The focus of these sections was to further explore are the fundamental mechanisms behind PARS microscopy and to explore future embodiments of the technique. Modelling was performed for simple planar geometries (Ch. 3) and more complex spherical scattering particles (Ch. 4). Planar models built upon the initially proposed time-independent two-state model from the first report [3] by including consideration of the time evolution. This investigation corroborated much of the initial findings and suggested the potential existence of an additional GHz range oscillation in the time domain signal which may be indicative of sample properties near the detection interface. However, these predictions could not be shown experimentally and may simply be a result of the model's over simplicity. The spherical scattering investigation showed that simple two-state representations may be woefully inappropriate outside of specific sample conditions in that they failed to adequately represent experimental measurements. However, the proposed multilayer scattering method was able to correctly predict the nonlinear relationship observed in nanometer-scale particles between the PARS signal intensity and excitation pulse energy. This approach considered the time-dependent evolution of the refractive index profile as a series of concentric spheres. These simple models are then later used to form the basis of more complex proposed modalities discussed in chapter 6.

7.1.3 Limitations

Since it was the original intention of this work to examine simplistic geometries to try and gain intuitive insight into the PARS mechanism, a great deal of considerations where omitted from the work. Both investigations only considered incident plane waves, which are not used in experiments.

Experiments are conducted with focused beams (assumed to be close to Gaussian TEM_{00}). This approximation was assumed to be acceptable as Gaussian beams have little curvature near their focus. However, the finite lateral profile of the beams may play a role in the longevity of the PARS time signals. This was noted in [1] as a potential cause of discrepancy. In a Gaussian-plane interaction one would expect optical and acoustic diffraction to reduce the signal longevity which would likely bring analytical results more inline with experimental observations. Another omission was the inclusion of acoustic impedance mismatches. Here acoustic impedance was assumed to be homogeneous. In general this will not be the case for real samples, however within biological tissues there would not be a large acoustic mismatch expected. This is inline with the substantially longer transport mean-free-path of acoustic waves in biological tissues as compared to optical waves. Future investigations could include inhomogeneous acoustic impedances to see what effects they might incur on the signals.

7.2 Fast functional PARS imaging

7.2.1 Contributions

Work on the functional PARS imaging system was lead primarily by the author who was involved with optical and software design, and conducted experiments.

7.2.2 Discussion

The primary goals of this apparatus was to construct a device which was capable of performing real-time functional imaging and a device which featured a tetherable scan head. The real-time functional aspect involved solving two distinct issues. First, the method of generating multiple wavelengths which had been previously used involved over-pumping a single-mode optical fiber to induce stimulated Raman scattering, forming distinct Raman spectral bands. The spectral content at the output of the fiber was controlled by simply modulating the input power. This allowed for the implementation

of pulse-to-pulse switching of output wavelengths by rapid modulation of the pump beam through the use of an electro-optic modulator. The second issue to be solved, involved augmenting the conventional narrow-linewidth demixing algorithm such that it could account for the complex excitation spectra. This was accomplished, and allows for more general consideration of excitation wavelengths. The desired for a tetherable scan head also motivated the use of the broad Raman spectra as the fiber-based components would inherently detract from the optical power efficiency of the system. Thus by not throwing away the majority of the spectrum, more excitation energy could be maintained.

7.2.3 Limitations

Although real-time frame rates were demonstrated, the approach suffered from poor SNR and unmixing accuracy. This was primarily attributed to the inconsistent output power for two given SRS spectra. This could have arose from several points in the system. The free-space electro-optic modulator degraded the quality of the output beam such that coupling into the optical fiber for non-linear modification was inconsistent. As well, small power modulations in the pump source itself could have easily resulted in larger power modulations and spectral modulations at the output due to the non-linear relationship between the input and output end of the fiber. Future apparatus should implement a second active power modulation stage at the exit of the single-mode fiber to provide additional pulse normalization. This should better allow for balancing between safe optical exposure levels and providing sufficient excitation energy necessary for reasonable quality unmixing. As well, beam quality and coupling issues could be mitigated through the use of an in-line fiber-based electro-optic modulator rather than a free-space element.

7.3 Coherence-gated PARS

7.3.1 Contributions

Work on the analytical modelling and simulation for the proposed coherence-gate PARS system was lead primarily by the author.

7.3.2 Discussion

The final topic covered in this work involved a new proposed modality which uses the PARS detection method. This involved the addition of optical coherence gating to the detection path such that depth discrimination could be provided outside of optical sectioning. In conventional PARS microscopy the axial performance of the device is solely determined by the optical section provided by the primary focusing optics. Although this is more than adequate at superficial depths, at deeper penetrations whether optical focus deteriorates, the axial performance quickly degrades. As well, conventional PARS requires performing of depth scanning to interrogate volumes, something which traditional contact-based PA modalities inherently provide. These issues first motivated the creation of CG-PARS which takes heavy influence from spectral-domain OCT (Ch. 6). By marking the difference between an OCT A-scan before and after a photoacoustic excitation, observed changes may be primarily attributed to PARS modulations in the scattering profile. However, the logistics of a spectral detection which can interrogate nanosecond-scale events is not trivial and would require the construction of a pulsed-detection OCT to facilitate short interrogation times. This modality was examined with simulations and mathematical modelling but had not yet been constructed and tested. It would seem to be similarly characterized like a SD-OCT device in that it would be appropriate to use low-NA objectives to purposely extend the optical depth of focus, allowing the fill axial performance of the device to be determined by the coherence gate. This modality would promise to acquire full PARS A-scans within a two-detection pulse train. A clear future direction for coherence-augmented PARS devices would be to pull from concepts in time-domain OCT to pro-

vide a microscopy which can decouple axial performance from the optical section. This may be particularly useful in PARS since the method has demonstrated exceptional performance at depth in terms of sensitivity, but the axial resolution degrades rapidly.

7.3.3 Limitations

Some potential issues with an eventual experimental apparatus arose from the analytical and simulation work conducted. One aspect which appears to require significant consideration is regarding the sensitivity of the optical receive elements used in the spectral detection as the system will inherently require a large dynamic range to be able to detect the small PARS perturbations in the scattering profiles. Another aspect is that since the method relies on acquiring two OCT A-scans in quick succession, any significant motion of the sample between these acquisitions will corrupt the final extracted profile. It would seem wise to design the pulses such that this delay between scans is minimized.

7.4 Concluding statements

PARS microscopy is positioned to be a dynamic and exciting field within the optics and biomedical imaging communities in the times to come. The techniques investigated thus far have demonstrated exceptional capabilities. Future work will likely focus on various new targets, many of which have already been shown to work with conventional contact-based PA devices. These would include targeting DNA and cytochrome absorption to provide label-free visualization of cell nuclei and cytoplasm respectively, potentially facilitating label-free histopathology. As well, there is a wealth of exogenous agents such as various nanoparticles and fluorescent markers which may drastically improve the range of targets, and functional information available to PARS devices. It will be exciting to water the next several years of PARS developments to truly see what the technology can achieve.

Bibliography

[1] K. L. Bell, P. Hajireza, W. Shi, and R. J. Zemp, "Temporal evolution of low-coherence reflectrometry signals in photoacoustic remote sensing microscopy," *Applied optics*, vol. 56, no. 18, pp. 5172–5181, 2017.

[2] K. Bell, P. Hajireza, and R. Zemp, "Scattering cross-sectional modulation in photoacoustic remote sensing microscopy," *Optics letters*, vol. 43, no. 1, pp. 146–149, 2018.

[3] P. Hajireza, W. Shi, K. Bell, R. J. Paproski, and R. J. Zemp, "Non-interferometric photoacoustic remote sensing microscopy," *Light: Science & Applications*, vol. 6, no. 6, p. e16278, 2017.

[4] K. L. Bell, P. Hajireza, and R. J. Zemp, "Coherence-gated photoacoustic remote sensing microscopy," *Optics express*, vol. 26, no. 18, pp. 23 689–23 704, 2018.

[5] S. Hu, K. Maslov, and L. V. Wang, "Second-generation optical-resolution photoacoustic microscopy with improved sensitivity and speed," *Optics letters*, vol. 36, no. 7, pp. 1134–1136, 2011.

[6] L. V. Wang and S. Hu, "Photoacoustic tomography: in vivo imaging from organelles to organs," *Science*, vol. 335, no. 6075, pp. 1458–1462, 2012.

[7] M. Jeon, J. Kim, and C. Kim, "Multiplane spectroscopic whole-body photoacoustic imaging of small animals in vivo," *Medical & biological engineering & computing*, vol. 54, no. 2-3, pp. 283–294, 2016.

[8] E. Zhang, J. Laufer, and P. Beard, "Backward-mode multiwavelength photoacoustic scanner using a planar fabry-perot polymer film ultrasound sensor for high-resolution three-dimensional imaging of biological tissues," *Applied optics*, vol. 47, no. 4, pp. 561–577, 2008.

[9] A. P. Jathoul, J. Laufer, O. Ogunlade, B. Treeby, B. Cox, E. Zhang, P. Johnson, A. R. Pizzey, B. Philip, T. Marafioti *et al.*, "Deep in vivo photoacoustic imaging of mammalian tissues using a tyrosinase-based genetic reporter," *Nature Photonics*, 2015.

[10] P. Hajireza, J. Sorge, M. Brett, and R. Zemp, "In vivo optical resolution photoacoustic microscopy using glancing angle-deposited nanostructured fabry–perot etalons," *Optics letters*, vol. 40, no. 7, pp. 1350–1353, 2015.

[11] R. Ellwood, O. Ogunlade, E. Zhang, P. Beard, and B. Cox, "Photoacoustic tomography using orthogonal fabry–pérot sensors," *Journal of Biomedical Optics*, vol. 22, no. 4, pp. 041 009–041 009, 2017.

[12] H. Li, B. Dong, Z. Zhang, H. F. Zhang, and C. Sun, "A transparent broadband ultrasonic detector based on an optical micro-ring resonator for photoacoustic microscopy," *Scientific reports*, vol. 4, p. 4496, 2014.

[13] G. Paltauf, R. Nuster, M. Haltmeier, and P. Burgholzer, "Photoacoustic tomography using a mach-zehnder interferometer as an acoustic line detector," *Applied optics*, vol. 46, no. 16, pp. 3352–3358, 2007.

[14] Z. Chen, S. Yang, Y. Wang, and D. Xing, "Noncontact broadband all-optical photoacoustic microscopy based on a low-coherence interferometer," *Applied Physics Letters*, vol. 106, no. 4, p. 043701, 2015.

[15] P. Hajireza, W. Shi, K. Bell, R. Paproski, and R. J. Zemp, "Non-interferometric photoacoustic remote sensing microscopy," *Light: Science & Applications*, vol. 1, no. 6, p. e16278, 2017.

[16] K. Maslov, H. F. Zhang, S. Hu, and L. V. Wang, "Optical-resolution photoacoustic microscopy for in vivo imaging of single capillaries," *Optics letters*, vol. 33, no. 9, pp. 929–931, 2008.

[17] V. P. Zharov, E. I. Galanzha, E. V. Shashkov, N. G. Khlebtsov, and V. V. Tuchin, "In vivo photoacoustic flow cytometry for monitoring of circulating single cancer cells and contrast agents," *Optics letters*, vol. 31, no. 24, pp. 3623–3625, 2006.

[18] T. Imai, J. Shi, T. T. Wong, L. Li, L. Zhu, and L. V. Wang, "High-throughput ultraviolet photoacoustic microscopy with multifocal excitation," *Journal of biomedical optics*, vol. 23, no. 3, p. 036007, 2018.

[19] T. T. Wong, R. Zhang, P. Hai, C. Zhang, M. A. Pleitez, R. L. Aft, D. V. Novack, and L. V. Wang, "Fast label-free multilayered histology-like imaging of human breast cancer by photoacoustic microscopy," *Science advances*, vol. 3, no. 5, p. e1602168, 2017.

[20] Y. Zhou, S. V. Tripathi, I. Rosman, J. Ma, P. Hai, G. P. Linette, M. L. Council, R. C. Fields, L. V. Wang, and L. A. Cornelius, "Non-invasive determination of melanoma depth using a handheld photoacoustic probe," *The Journal of investigative dermatology*, vol. 137, no. 6, p. 1370, 2017.

[21] C. Zhang, Y. S. Zhang, D.-K. Yao, Y. Xia, and L. V. Wang, "Label-free photoacoustic microscopy of cytochromes," *Journal of biomedical optics*, vol. 18, no. 2, p. 020504, 2013.

[22] K. Jansen, A. F. Van Der Steen, H. M. van Beusekom, J. W. Oosterhuis, and G. van Soest, "Intravascular photoacoustic imaging of human coronary atherosclerosis," *Optics letters*, vol. 36, no. 5, pp. 597–599, 2011.

[23] A. Agarwal, S. Huang, M. O'donnell, K. Day, M. Day, N. Kotov, and S. Ashkenazi, "Targeted gold nanorod contrast agent for prostate cancer detection by photoacoustic imaging," *Journal of applied physics*, vol. 102, no. 6, p. 064701, 2007.

[24] L. Li, R. J. Zemp, G. F. Lungu, G. Stoica, and L. V. Wang, "Photoacoustic imaging of lacz gene expression in vivo," *Journal of biomedical optics*, vol. 12, no. 2, p. 020504, 2007.

[25] P. H. Reza, K. Bell, W. Shi, J. Shapiro, and R. J. Zemp, "Deep noncontact photoacoustic initial pressure imaging," *Optica*, vol. 5, no. 7, pp. 814–820, 2018.

[26] P. H. Reza, K. Bell, W. Shi, and R. J. Zemp, "Multi-scale photoacoustic remote sensing (pars)(conference presentation)," in *Photons Plus Ultrasound: Imaging and Sensing 2016*, vol. 9708. International Society for Optics and Photonics, 2016, p. 97082F.

[27] P. H. HajiReza, K. L. Bell, W. Shi, and R. J. Zemp, "Non-interferometric deep optical resolution photoacoustic remote sensing microscopy (conference presentation)," in *Photons Plus Ultrasound: Imaging and Sensing 2017*, vol. 10064. International Society for Optics and Photonics, 2017, p. 1006420.

[28] K. L. Bell, P. H. Reza, W. Shi, and R. J. Zemp, "Temporal evolution of low-coherence reflectometry signals in photoacoustic remote sensing microscopy (conference presentation)," in *Photons Plus Ultrasound: Imaging and Sensing 2017*, vol. 10064. International Society for Optics and Photonics, 2017, p. 1006422.

[29] K. L. Bell, P. H. Reza, , and R. J. Zemp, "Spherical scatterer cross section modulation in photoacoustic remote sensing microscopy (conference presentation)," in *European Conference on Biomedical Optics*, 2017.

[30] L. Snider, K. Bell, P. Reza, and R. J. Zemp, "Toward wide-field high-speed photoacoustic remote sensing microscopy," in *Photons Plus Ul-*

trasound: Imaging and Sensing 2018, vol. 10494. International Society for Optics and Photonics, 2018, p. 1049423.

[31] K. L. Bell, P. Hajireza, and R. Zemp, "Coherence-gated photoacoustic remote sensing microscopy (conference presentation)," in *Photons Plus Ultrasound: Imaging and Sensing 2018*, vol. 10494. International Society for Optics and Photonics, 2018, p. 1049422.

[32] N. J. Haven, K. L. Bell, P. Kedarisetti, P. H. Reza, J. D. Lewis, and R. J. Zemp, "Label-free non-contact imaging of cell nuclei using ultraviolet photoacoustic remote sensing microscopy (conference presentation)," in *Photons Plus Ultrasound: Imaging and Sensing 2019*, vol. 10878. International Society for Optics and Photonics, 2019, p. 108781X.

[33] A. G. Bell, "On the production and reproduction of sound by light," *American Journal of Science*, no. 118, pp. 305–324, 1880.

[34] L. V. Wang and H.-i. Wu, *Biomedical optics: principles and imaging*. John Wiley & Sons, 2012.

[35] C. Hoelen, F. De Mul, R. Pongers, and A. Dekker, "Three-dimensional photoacoustic imaging of blood vessels in tissue," *Optics letters*, vol. 23, no. 8, pp. 648–650, 1998.

[36] T. T. Wong, R. Zhang, P. Hai, R. L. Aft, D. V. Novack, and L. V. Wang, "Photoacoustic microscopy enables multilayered histological imaging of human breast cancer without staining," in *Photons Plus Ultrasound: Imaging and Sensing 2018*, vol. 10494. International Society for Optics and Photonics, 2018, p. 1049443.

[37] E. I. Galanzha, E. V. Shashkov, P. M. Spring, J. Y. Suen, and V. P. Zharov, "In vivo, noninvasive, label-free detection and eradication of circulating metastatic melanoma cells using two-color photoacoustic flow cytometry with a diode laser," *Cancer research*, vol. 69, no. 20, pp. 7926–7934, 2009.

[38] J.-T. Oh, M.-L. Li, H. F. Zhang, K. Maslov, and L. V. Wang, "Three-dimensional imaging of skin melanoma in vivo by dual-wavelength photoacoustic microscopy," *Journal of biomedical optics*, vol. 11, no. 3, p. 034032, 2006.

[39] J. L. Su, R. R. Bouchard, A. B. Karpiouk, J. D. Hazle, and S. Y. Emelianov, "Photoacoustic imaging of prostate brachytherapy seeds," *Biomedical optics express*, vol. 2, no. 8, pp. 2243–2254, 2011.

[40] J. L. Su, A. B. Karpiouk, B. Wang, and S. Y. Emelianov, "Photoacoustic imaging of clinical metal needles in tissue," *Journal of biomedical optics*, vol. 15, no. 2, p. 021309, 2010.

[41] J. Laufer, P. Johnson, E. Zhang, B. Treeby, B. Cox, B. Pedley, and P. Beard, "In vivo preclinical photoacoustic imaging of tumor vasculature development and therapy," *Journal of biomedical optics*, vol. 17, no. 5, pp. 0 560 161–0 560 168, 2012.

[42] S. Manohar, S. E. Vaartjes, J. C. van Hespen, J. M. Klaase, F. M. van den Engh, W. Steenbergen, and T. G. Van Leeuwen, "Initial results of in vivo non-invasive cancer imaging in the human breast using near-infrared photoacoustics," *Optics express*, vol. 15, no. 19, pp. 12 277–12 285, 2007.

[43] M. Pramanik, G. Ku, C. Li, and L. V. Wang, "Design and evaluation of a novel breast cancer detection system combining both thermoacoustic (ta) and photoacoustic (pa) tomography," *Medical physics*, vol. 35, no. 6Part1, pp. 2218–2223, 2008.

[44] M. Heijblom, D. Piras, W. Xia, J. C. van Hespen, J. Klaase, F. Van den Engh, T. Van Leeuwen, W. Steenbergen, and S. Manohar, "Visualizing breast cancer using the twente photoacoustic mammoscope: what do we learn from twelve new patient measurements?" *Optics express*, vol. 20, no. 11, pp. 11 582–11 597, 2012.

[45] J. Zhang, S. Yang, X. Ji, Q. Zhou, and D. Xing, "Characterization of lipid-rich aortic plaques by intravascular photoacoustic tomography:

ex vivo and in vivo validation in a rabbit atherosclerosis model with histologic correlation," *Journal of the American College of Cardiology*, vol. 64, no. 4, pp. 385–390, 2014.

[46] P. Schoenhagen and D. G. Vince, "Intravascular photoacoustic tomography of coronary atherosclerosis: riding the waves of light and sound," 2014.

[47] M.-L. Li, J.-T. Oh, X. Xie, G. Ku, W. Wang, C. Li, G. Lungu, G. Stoica, and L. V. Wang, "Simultaneous molecular and hypoxia imaging of brain tumors in vivo using spectroscopic photoacoustic tomography," *Proceedings of the IEEE*, vol. 96, no. 3, pp. 481–489, 2008.

[48] K. Aizawa, S. Sato, D. Saitoh, H. Ashida, and M. Obara, "Photoacoustic monitoring of burn healing process in rats," *Journal of biomedical optics*, vol. 13, no. 6, p. 064020, 2008.

[49] C. Lutzweiler, R. Meier, E. Rummeny, V. Ntziachristos, and D. Razansky, "Real-time optoacoustic tomography of indocyanine green perfusion and oxygenation parameters in human finger vasculature," *Optics letters*, vol. 39, no. 14, pp. 4061–4064, 2014.

[50] E. W. Stein, K. I. Maslov, and L. V. Wang, "Noninvasive, in vivo imaging of blood-oxygenation dynamics within the mouse brain using photoacoustic microscopy," *Journal of biomedical optics*, vol. 14, no. 2, p. 020502, 2009.

[51] D.-K. Yao, K. Maslov, K. K. Shung, Q. Zhou, and L. V. Wang, "In vivo label-free photoacoustic microscopy of cell nuclei by excitation of dna and rna," *Optics letters*, vol. 35, no. 24, pp. 4139–4141, 2010.

[52] L. Wang, K. I. Maslov, W. Xing, A. Garcia-Uribe, and L. V. Wang, "Video-rate functional photoacoustic microscopy at depths," *Journal of biomedical optics*, vol. 17, no. 10, p. 106007, 2012.

[53] J. Niederhauser, M. Jaeger, M. Hejazi, H. Keppner, and M. Frenz, "Transparent ito coated pvdf transducer for optoacoustic depth profiling," *Optics communications*, vol. 253, no. 4, pp. 401–406, 2005.

[54] H. F. Zhang, K. Maslov, and L. V. Wang, "In vivo imaging of subcutaneous structures using functional photoacoustic microscopy," *Nature protocols*, vol. 2, no. 4, pp. 797–804, 2007.

[55] S. J. Kavros, D. A. Liedl, A. J. Boon, J. L. Miller, J. A. Hobbs, and K. L. Andrews, "Expedited wound healing with noncontact, low-frequency ultrasound therapy in chronic wounds: a retrospective analysis," *Advances in skin & wound care*, vol. 21, no. 9, pp. 416–423, 2008.

[56] Y. Sun, M. Y. Sy, Y.-X. J. Wang, A. T. Ahuja, Y.-T. Zhang, and E. Pickwell-MacPherson, "A promising diagnostic method: Terahertz pulsed imaging and spectroscopy," *World journal of radiology*, vol. 3, no. 3, p. 55, 2011.

[57] V. Ntziachristos, J. S. Yoo, and G. M. van Dam, "Current concepts and future perspectives on surgical optical imaging in cancer," *Journal of biomedical optics*, vol. 15, no. 6, pp. 066 024–066 024, 2010.

[58] J. Thomson, H. Wickramasinghe, and E. Ash, "A fabry-perot acoustic surface vibration detector-application to acoustic holography," *Journal of Physics D: Applied Physics*, vol. 6, no. 6, p. 677, 1973.

[59] P. C. Beard and T. N. Mills, "Optical fiber sensor for the detection of laser-generated ultrasound in arterial tissues," in *International Symposium on Biomedical Optics Europe'94*. International Society for Optics and Photonics, 1995, pp. 112–122.

[60] P. Beard and T. Mills, "Extrinsic optical-fiber ultrasound sensor using a thin polymer film as a low-finesse fabry–perot interferometer," *Applied optics*, vol. 35, no. 4, pp. 663–675, 1996.

[61] ——, "Miniature optical fibre ultrasonic hydrophone using a fabry-perot polymer film interferometer," *Electronics Letters*, vol. 33, no. 9, pp. 801–803, 1997.

[62] O. S. Heavens, *Optical properties of thin solid films*. Courier Corporation, 1991.

[63] E. Z. Zhang and P. C. Beard, "A miniature all-optical photoacoustic imaging probe," in *SPIE BiOS*. International Society for Optics and Photonics, 2011, pp. 78 991F–78 991F.

[64] R. J. Colchester, E. Z. Zhang, C. A. Mosse, P. C. Beard, I. Papakonstantinou, and A. E. Desjardins, "Broadband miniature optical ultrasound probe for high resolution vascular tissue imaging," *Biomedical optics express*, vol. 6, no. 4, pp. 1502–1511, 2015.

[65] S. J. Mathews, E. Z. Zhang, A. E. Desjardins, and P. C. Beard, "Miniature fibre optic probe for minimally invasive photoacoustic sensing," in *SPIE BiOS*. International Society for Optics and Photonics, 2016, pp. 97 082R–97 082R.

[66] P. Hajireza, K. Krause, M. Brett, and R. Zemp, "Glancing angle deposited nanostructured film fabry-perot etalons for optical detection of ultrasound," *Optics express*, vol. 21, no. 5, pp. 6391–6400, 2013.

[67] B. Huang, J. Xia, K. Maslov, and L. V. Wang, "Improving limited-view photoacoustic tomography with an acoustic reflector," *Journal of biomedical optics*, vol. 18, no. 11, pp. 110 505–110 505, 2013.

[68] G. Li, J. Xia, K. Wang, K. Maslov, M. A. Anastasio, and L. V. Wang, "Tripling the detection view of high-frequency linear-array-based photoacoustic computed tomography by using two planar acoustic reflectors," *Quantitative imaging in medicine and surgery*, vol. 5, no. 1, p. 57, 2015.

[69] R. Ellwood, E. Zhang, P. Beard, and B. Cox, "Orthogonal fabry-pérot sensor array system for minimal-artifact photoacoustic tomography,"

in *SPIE BiOS*. International Society for Optics and Photonics, 2015, pp. 932 312–932 312.

[70] R. Ellwood, O. Ogunlade, E. Zhang, P. Beard, and B. Cox, "Orthogonal fabry-pérot sensors for photoacoustic tomography," in *SPIE BiOS*. International Society for Optics and Photonics, 2016, pp. 97 082N–97 082N.

[71] Z. Xie, S.-L. Chen, T. Ling, L. J. Guo, P. L. Carson, and X. Wang, "Pure optical photoacoustic microscopy," *Optics express*, vol. 19, no. 10, pp. 9027–9034, 2011.

[72] T. Ling, S.-L. Chen, and L. J. Guo, "Fabrication and characterization of high q polymer micro-ring resonator and its application as a sensitive ultrasonic detector," *Optics express*, vol. 19, no. 2, pp. 861–869, 2011.

[73] K. Kim, W. Luo, C. Zhang, C. Tian, L. Guo, X. Wang, and X. Fan, "Air-coupled ultrasound detection using capillary-based optical ring resonators." *Scientific reports*, vol. 7, no. 1, p. 109, 2017.

[74] X. L. Deán-Ben, G. A. Pang, F. Montero de Espinosa, and D. Razansky, "Non-contact optoacoustic imaging with focused air-coupled transducers," *Applied Physics Letters*, vol. 107, no. 5, p. 051105, 2015.

[75] W. Kaule, "Interferometric method and apparatus for sensing surface deformation of a workpiece subjected to acoustic energy," Sep. 6 1977, uS Patent 4,046,477.

[76] ——, "Method and apparatus for receiving ultrasonic waves by optical means," Jun. 21 1983, uS Patent 4,388,832.

[77] J.-P. Monchalin, "Optical detection of ultrasound at a distance using a confocal fabry–perot interferometer," *Applied Physics Letters*, vol. 47, no. 1, pp. 14–16, 1985.

[78] R. Dewhurst and Q. Shan, "Modelling of confocal fabry-perot interferometers for the measurement of ultrasound," *Measurement Science and Technology*, vol. 5, no. 6, p. 655, 1994.

[79] T. Berer, E. Leiss-Holzinger, A. Hochreiner, J. Bauer-Marschallinger, and A. Buchsbaum, "Multimodal noncontact photoacoustic and optical coherence tomography imaging using wavelength-division multiplexing," *Journal of biomedical optics*, vol. 20, no. 4, pp. 046 013–046 013, 2015.

[80] E. Leiss-Holzinger, J. Bauer-Marschallinger, A. Hochreiner, P. Hollinger, and T. Berer, "Dual modality noncontact photoacoustic and spectral domain oct imaging," *Ultrasonic imaging*, vol. 38, no. 1, pp. 19–31, 2016.

[81] Z. Chen, S. Yang, and D. Xing, "All-optically integrated multimodality imaging system: combined photoacoustic microscopy, optical coherence tomography, and fluorescence imaging," in *SPIE/COS Photonics Asia*. International Society for Optics and Photonics, 2016, pp. 100 240H–100 240H.

[82] Y. Wang, C. Li, and R. K. Wang, "Noncontact photoacoustic imaging achieved by using a low-coherence interferometer as the acoustic detector," *Optics letters*, vol. 36, no. 20, pp. 3975–3977, 2011.

[83] C. Blatter, B. Grajciar, P. Zou, W. Wieser, A.-J. Verhoef, R. Huber, and R. A. Leitgeb, "Intrasweep phase-sensitive optical coherence tomography for noncontact optical photoacoustic imaging," *Optics letters*, vol. 37, no. 21, pp. 4368–4370, 2012.

[84] J. Yao, "When pressure meets light: detecting the photoacoustic effect at the origin," *Light: Science & Applications*, vol. 6, no. 6, p. e17062, 2017.

[85] W. B. Leigh, *Devices for optoelectronics*. Marcel Dekker, 1996.

[86] D. Huang, E. A. Swanson, C. P. Lin, J. S. Schuman, W. G. Stinson, W. Chang, M. R. Hee, T. Flotte, K. Gregory, C. A. Puliafito *et al.*, "Optical coherence tomography," *science*, vol. 254, no. 5035, pp. 1178–1181, 1991.

[87] J. Schmitt, M. Yadlowsky, and R. Bonner, "Subsurface imaging of living skin with optical coherence microscopy," *Dermatology*, vol. 191, no. 2, pp. 93–98, 1995.

[88] J. G. Fujimoto, M. E. Brezinski, G. J. Tearney, S. A. Boppart, B. Bouma, M. R. Hee, J. F. Southern, and E. A. Swanson, "Optical biopsy and imaging using optical coherence tomography," *Nature medicine*, vol. 1, no. 9, pp. 970–972, 1995.

[89] J. M. Schmitt, "Optical coherence tomography (oct): a review," *IEEE Journal of selected topics in quantum electronics*, vol. 5, no. 4, pp. 1205–1215, 1999.

[90] R. C. Youngquist, S. Carr, and D. E. Davies, "Optical coherence-domain reflectometry: a new optical evaluation technique," *Optics letters*, vol. 12, no. 3, pp. 158–160, 1987.

[91] C. A. Puliafito, M. R. Hee, C. P. Lin, E. Reichel, J. S. Schuman, J. S. Duker, J. A. Izatt, E. A. Swanson, and J. G. Fujimoto, "Imaging of macular diseases with optical coherence tomography," *Ophthalmology*, vol. 102, no. 2, pp. 217–229, 1995.

[92] H. Pahlevaninezhad, M. Khorasaninejad, Y.-W. Huang, Z. Shi, L. P. Hariri, D. C. Adams, V. Ding, A. Zhu, C.-W. Qiu, F. Capasso *et al.*, "Nano-optic endoscope for high-resolution optical coherence tomography in vivo," *Nature photonics*, vol. 12, no. 9, p. 540, 2018.

[93] L. Ginner, A. Kumar, D. Fechtig, L. M. Wurster, M. Salas, M. Pircher, and R. A. Leitgeb, "Noniterative digital aberration correction for cellular resolution retinal optical coherence tomography in vivo," *Optica*, vol. 4, no. 8, pp. 924–931, 2017.

[94] T. E. De Carlo, A. Romano, N. K. Waheed, and J. S. Duker, "A review of optical coherence tomography angiography (octa)," *International journal of retina and vitreous*, vol. 1, no. 1, p. 5, 2015.

[95] S. Pi, A. Camino, W. Cepurna, X. Wei, M. Zhang, D. Huang, J. Morrison, and Y. Jia, "Automated spectroscopic retinal oximetry with visible-light optical coherence tomography," *Biomedical optics express*, vol. 9, no. 5, pp. 2056–2067, 2018.

[96] J. Yi, W. Liu, S. Chen, V. Backman, N. Sheibani, C. M. Sorenson, A. A. Fawzi, R. A. Linsenmeier, and H. F. Zhang, "Visible light optical coherence tomography measures retinal oxygen metabolic response to systemic oxygenation," *Light: Science & Applications*, vol. 4, no. 9, p. e334, 2015.

[97] S. H. Jack, D. B. Hann, and C. A. Greated, "Influence of the acousto-optic effect on laser doppler anemometry signals," *Review of scientific instruments*, vol. 69, no. 12, pp. 4074–4081, 1998.

[98] A. Yariv and P. Yeh, "Optical waves in layered media," 1988.

[99] T. L. T Biswas, "In vivo mr measurement of refractive index, relative water content and t2 relaxation time of various brain lesions with clinical application to discriminate brain lesions," *The Internet Journal of Radiology*, vol. 13, no. 1, 2009.

[100] G. S. Adair and M. E. Robinson, "The specific refraction increments of serum-albumin and serum-globulin," *Biochemical Journal*, vol. 24, no. 4, p. 993, 1930.

[101] J. Vörös, "The density and refractive index of adsorbing protein layers," *Biophysical journal*, vol. 87, no. 1, pp. 553–561, 2004.

[102] M. Friebel and M. Meinke, "Model function to calculate the refractive index of native hemoglobin in the wavelength range of 250-1100 nm dependent on concentration," *Applied optics*, vol. 45, no. 12, pp. 2838–2842, 2006.

[103] S. Prahl. (2017) Optical absorption of hemoglobin. [Online]. Available: http://omlc.org/spectra/hemoglobin/

[104] M. A. Green and M. J. Keevers, "Optical properties of intrinsic silicon at 300 k," *Progress in Photovoltaics: Research and Applications*, vol. 3, no. 3, pp. 189–192, 1995.

[105] J. M. Steinke and A. Shepherd, "Comparison of mie theory and the light scattering of red blood cells," *Applied optics*, vol. 27, no. 19, pp. 4027–4033, 1988.

[106] J. R. Wait, "Electromagnetic scattering from a radially inhomogeneous sphere," *Applied Scientific Research, Section B*, vol. 10, no. 5-6, pp. 441–450, 1962.

[107] R. Bhandari, "Scattering coefficients for a multilayered sphere: analytic expressions and algorithms," *Applied optics*, vol. 24, no. 13, pp. 1960–1967, 1985.

[108] D. Mackowski, R. Altenkirch, and M. Menguc, "Internal absorption cross sections in a stratified sphere," *Applied Optics*, vol. 29, no. 10, pp. 1551–1559, 1990.

[109] V. Cachorro and L. Salcedo, "New improvements for mie scattering calculations," *Journal of electromagnetic waves and applications*, vol. 5, no. 9, pp. 913–926, 1991.

[110] W. J. Wiscombe, "Improved mie scattering algorithms," *Applied optics*, vol. 19, no. 9, pp. 1505–1509, 1980.

[111] O. Pena and U. Pal, "Scattering of electromagnetic radiation by a multilayered sphere," *Computer Physics Communications*, vol. 180, no. 11, pp. 2348–2354, 2009.

[112] P. B. Johnson and R.-W. Christy, "Optical constants of the noble metals," *Physical review B*, vol. 6, no. 12, p. 4370, 1972.

[113] P. Hajireza, A. Forbrich, and R. Zemp, "In-vivo functional optical-resolution photoacoustic microscopy with stimulated raman scattering fiber-laser source," *Biomedical optics express*, vol. 5, no. 2, pp. 539–546, 2014.

[114] Y. Liang, L. Jin, B.-O. Guan, and L. Wang, "2 mhz multi-wavelength pulsed laser for functional photoacoustic microscopy," *Optics letters*, vol. 42, no. 7, pp. 1452–1455, 2017.

[115] Y. N. Billeh, M. Liu, and T. Buma, "Spectroscopic photoacoustic microscopy using a photonic crystal fiber supercontinuum source," *Optics express*, vol. 18, no. 18, pp. 18 519–18 524, 2010.

[116] K. L. Bell, P. H. Reza, and R. J. Zemp, "Real-time functional photoacoustic remote sensing microscopy," *Optics letters*, vol. 44, no. 14, pp. 3466–3469, 2019.

[117] B. Bouma, *Handbook of optical coherence tomography*. CRC Press, 2001.

[118] T. Wang, T. Pfeiffer, E. Regar, W. Wieser, H. van Beusekom, C. T. Lancee, G. Springeling, I. Krabbendam, A. F. van der Steen, R. Huber *et al.*, "Heartbeat oct: in vivo intravascular megahertz-optical coherence tomography," *Biomedical optics express*, vol. 6, no. 12, pp. 5021–5032, 2015.

[119] K. Yee, "Numerical solution of initial boundary value problems involving maxwell's equations in isotropic media," *IEEE Transactions on antennas and propagation*, vol. 14, no. 3, pp. 302–307, 1966.

[120] A. Taflove and S. C. Hagness, *Computational electrodynamics: the finite-difference time-domain method*. Artech house, 2005.

[121] S. Sakadžić and L. V. Wang, "Modulation of multiply scattered coherent light by ultrasonic pulses: an analytical model," *Physical Review E*, vol. 72, no. 3, p. 036620, 2005.

[122] S. G. Resink, W. Steenbergen, and A. C. Boccara, "State-of-the art of acoust-optic sensing and imaging of turbid media," *Journal of biomedical optics*, vol. 17, no. 4, p. 040901, 2012.

[123] J. A. Izatt, M. A. Choma, and A.-H. Dhalla, "Theory of optical coherence tomography," *Optical Coherence Tomography: Technology and Applications*, pp. 65–94, 2015.

[124] M. Gu, C. Sheppard, and X. Gan, "Image formation in a fiber-optical confocal scanning microscope," *JOSA A*, vol. 8, no. 11, pp. 1755–1761, 1991.

[125] T. Wilson and C. Sheppard, *Theory and practice of scanning optical microscopy*. Academic, 1984, vol. 180.

[126] B. H. Hokr, J. N. Bixler, G. Elpers, B. Zollars, R. J. Thomas, V. V. Yakovlev, and M. O. Scully, "Modeling focusing gaussian beams in a turbid medium with monte carlo simulations," *Optics express*, vol. 23, no. 7, pp. 8699–8705, 2015.

[127] B. Karamata, K. Hassler, M. Laubscher, and T. Lasser, "Speckle statistics in optical coherence tomography," *JOSA A*, vol. 22, no. 4, pp. 593–596, 2005.

[128] A. F. Fercher, "Optical coherence tomography–development, principles, applications," *Zeitschrift für Medizinische Physik*, vol. 20, no. 4, pp. 251–276, 2010.

[129] A. Zhang, Q. Zhang, Y. Huang, Z. Zhong, and R. K. Wang, "Multifunctional 1050 nm spectral domain oct system at 147 khz for posterior eye imaging," *Sovremennye tekhnologii v meditsine*, vol. 7, no. 1 (eng), 2015.

[130] M. Almasian, T. G. Leeuwen, and D. J. Faber, "Oct amplitude and speckle statistics of discrete random media," *Scientific reports*, vol. 7, no. 1, p. 14873, 2017.

[131] W. Yang, "Improved recursive algorithm for light scattering by a multilayered sphere," *Applied optics*, vol. 42, no. 9, pp. 1710–1720, 2003.

Appendix A

Approximation used in the planar PARS model

Plugging in values from equations 3.23-3.26 into the transfer matrix system (Eq. 3.17-3.20) gives the general form for the intensity reflectivity of

$$R(t,\nu) = \left| \frac{Ae^{i2k_1L_1} + Be^{i2k_2L_2} + Ce^{i2(k_1L_1+k_2L_2)} + D}{Ee^{i2k_1L_1} + Fe^{i2k_2L_2} + Ge^{i2(k_1L_1+k_2L_2)} + H} \right|^2 \tag{A.1}$$

where

$$\begin{aligned}
A &= 18n_1\delta n_1\delta n_2 - 12n_1\delta n_2^2 + 24n_1^2\delta n_2 + 4n_2\delta n_1^2 \\
&\quad - 10n_2\delta n_1\delta n_2 + 24n_1n_2\delta n_1 - 40n_1n_2\delta n_2 \\
&\quad + 32n_1^2n_2 - 8n_2^2\delta n_1 - 32n_1n_2^2 + \mathcal{O}\{\delta n^3\} && \text{(A.2)} \\
B &= 2n_1\delta n_1\delta n_2 - 2n_2\delta n_1\delta n_2 + \mathcal{O}\{\delta n^3\} && \text{(A.3)} \\
C &= -6n_1\delta n_1\delta n_2 - 4n_1\delta n_2^2 \\
&\quad - 8n_1^2\delta n_2 - 2n_2\delta n_1\delta n_2 - 8n_1n_2\delta n_2 + \mathcal{O}\{\delta n^3\} && \text{(A.4)} \\
D &= -6n_1\delta n_1\delta n_2 - 4n_2\delta n_1^2 - 10n_2\delta n_1\delta n_2 \\
&\quad - 8n_1n_2\delta n_1 - 8n_2^2\delta n_1 + \mathcal{O}\{\delta n^3\} && \text{(A.5)}
\end{aligned}$$

$$
\begin{aligned}
E &= 6n_1\delta n_1\delta n_2 + 4n_2\delta n_1^2 - 10n_2\delta n_1\delta n_2 \\
&\quad + 8n_1n_2\delta n_1 - 8n_2^2\delta n_1 + \mathcal{O}\{\delta n^3\} && \text{(A.6)} \\
F &= 6n_1\delta n_1\delta n_2 - 4n_1\delta n_2^2 + 8n_1^2\delta n_2 - 2n_2\delta n_1\delta n_2 \\
&\quad - 8n_1n_2\delta n_2 + \mathcal{O}\{\delta n^3\} && \text{(A.7)} \\
G &= -2n_1\delta n_1\delta n_2 - 2n_2\delta n_1\delta n_2 + \mathcal{O}\{\delta n^3\} && \text{(A.8)} \\
H &= -18n_1\delta n_1\delta n_2 - 12n_1\delta n_2^2 - 24n_1^2\delta n_2 - 4n_2\delta n_1^2 \\
&\quad - 10n_2\delta n_1\delta n_2 - 24n_1n_2\delta n_1 - 40n_1n_2\delta n_2 \\
&\quad - 32n_1^2n_2 - 8n_2^2\delta n_1 - 32n_1n_2^2 + \mathcal{O}\{\delta n^3\} && \text{(A.9)}
\end{aligned}
$$

$$
2k_i(\nu)L_i(t) = \frac{4\pi n_i^* v_s \nu t}{c} = \omega_i(\nu)t + i\alpha_i(\nu)t \qquad \text{(A.10)}
$$

$$
n_{1,2}^* = n_{1,2} + \delta n_{1,2}/2 \qquad \text{(A.11)}
$$

Evaluating the magnitude square in equation A.1 gives

$$
\begin{aligned}
R(t,\nu) = &\frac{|A|^2e^{-2\alpha_1 t} + |B|^2e^{-2\alpha_2 t} + |C|^2e^{-2\alpha_3 t} + |D|^2}{|E|^2e^{-2\alpha_1 t} + |F|^2e^{-2\alpha_2 t} + |G|^2e^{-2\alpha_3 t} + |H|^2} \cdots \\
&\frac{+2\mathrm{Re}\{AB\}e^{-\alpha_3 t}\cos(\omega_3 t) + 2\mathrm{Re}\{AC\}e^{-\alpha_4 t}\cos(\omega_4 t)}{+2\mathrm{Re}\{EF\}e^{-\alpha_3 t}\cos(\omega_3 t) + 2\mathrm{Re}\{EG\}e^{-\alpha_4 t}\cos(\omega_4 t)} \cdots \\
&\frac{+2\mathrm{Re}\{AD\}e^{-\alpha_1 t}\cos(\omega_1 t) + 2\mathrm{Re}\{BC\}e^{-\alpha_5}\cos(\omega_5 t)}{+2\mathrm{Re}\{EH\}e^{-\alpha_1 t}\cos(\omega_1 t) + 2\mathrm{Re}\{FG\}e^{-\alpha_5 t}\cos(\omega_5 t)} \cdots \\
&\frac{+2\mathrm{Re}\{BD\}e^{-\alpha_2 t}\cos(\omega_2 t) + 2\mathrm{Re}\{CD\}e^{-\alpha_3 t}\cos(\omega_3 t)}{+2\mathrm{Re}\{FH\}e^{-\alpha_2 t}\cos(\omega_2 t) + 2\mathrm{Re}\{GH\}e^{-\alpha_3 t}\cos(\omega_3 t)} \cdots \\
&+ \mathcal{O}\{\delta n^3\} \qquad \text{(A.12)}
\end{aligned}
$$

where

$$\omega_3 = \omega_1 + \omega_2 \tag{A.13}$$

$$\omega_4 = 2\omega_1 + \omega_2 \tag{A.14}$$

$$\omega_5 = \omega_1 + 2\omega_2 \tag{A.15}$$

$$\alpha_3 = \alpha_1 + \alpha_2 \tag{A.16}$$

$$\alpha_4 = 2\alpha_1 + \alpha_2 \tag{A.17}$$

$$\alpha_5 = \alpha_1 + 2\alpha_2 \tag{A.18}$$

We would like for the initial state of the system to be that of the unperturbed interface R_s such that

$$R(t,\nu)|_{t<0} = R_s \tag{A.19}$$

and so we get the general form

$$R(t,\nu) = R_s + \mathcal{H}(t)\frac{a_0 + \sum_{m=1}^{3} a_m e^{-\alpha_m t} + \sum_{m=1}^{5} b_m e^{-\alpha_m t}\cos(\omega_m t)}{c_0 + \sum_{m=1}^{3} c_m e^{-\alpha_m t} + \sum_{m=1}^{5} d_m e^{-\alpha_m t}\cos(\omega_m t)} \tag{A.20}$$

where $\mathcal{H}$ is the Heaviside step function, $\alpha_m(\nu)$ and $\omega_m(\nu)$ terms relate to the imaginary and the real components of the wavenumbers respectively, and a_m, b_m, c_m, d_m are constants.

Looking at numerical values for the terms when considering an *in vivo* range ($1.33 < \mathrm{Re}\{n_{1,2}\} < 1.5$) is clear that $B \ll A, C, D$ and that $H \gg E, F, G$. Then letting the imaginary components be small,we can plug into equation A.1 assuming

$$A \approx 32 n_1 n_2 (n_1 - n_2) \tag{A.21}$$

$$B \approx 0 \tag{A.22}$$

$$C \approx -8 n_1 \delta n_2 (n_1 + n_2) \tag{A.23}$$

$$D \approx -8 n_2 \delta n_1 (n_1 + n_2) \tag{A.24}$$

$$E \approx 0 \tag{A.25}$$

$$F \approx 0 \tag{A.26}$$

$$G \approx 0 \tag{A.27}$$

$$H \approx 32 n_1 n_2 (n_1 + n_2) \tag{A.28}$$

and get equation 3.28

$$\begin{aligned} R(t,\nu) = & \frac{R_s}{16 n_1^2 n_2^2} \Bigg(16 n_1^2 n_2^2 \\ & + \frac{(n_1^2 \delta n_2^2 + n_2^2 \delta n_1^2)(n_1 + n_2)^2}{(n_1 - n_2)^2} \\ & - 8 \frac{n_1 n_2^2 \delta n_1 (n_1 + n_2)}{(n_1 - n_2)} \cos(\omega_1 t) \\ & - 8 \frac{n_1^2 n_2 \delta n_2 (n_1 + n_2)}{(n_1 - n_2)} \cos(\omega_2 t) \\ & + 2 \frac{n_1 n_2 \delta n_1 \delta n_2 (n_1 + n_2)^2}{(n_1 - n_2)^2} \cos(\omega_3 t) \Bigg) \end{aligned} \tag{A.29}$$

Appendix B

Overview of simulation for planar PARS model

To compare with the analytical model, a FDTD based simulation is used [119]. This is implemented both on the generation of the photoacoustic (PA) pulse and on the 1D electro-magnetic plane-wave interaction of the resulting profile. For the PA equation we start with

$$\left(\nabla^2 - \frac{1}{v_s^2}\frac{\partial^2}{\partial t^2}\right) p(\mathbf{r}, t) = -\frac{\beta}{C_P}\frac{\partial H(\mathbf{r}, t)}{\partial t} \tag{B.1}$$

which is an acoustic wave equation of pressure $p(\mathbf{r}, t)$, with a source term $H(\mathbf{r}, t)$ describing the localized heating generated by the absorption of an optical excitation pulse, β is the thermal coefficient of volume expansion, C_P is the specific heat capacity at constant pressure and v_s is the speed of acoustic wave propagation in the medium.

FDTD formulation of the PA equation is performed as

$$\nabla^2 p(\mathbf{r},t) = \frac{p_i^{n+1} - 2p_i^n + p_i^{n-1}}{(\Delta t_a)^2} \tag{B.2}$$

$$\frac{\partial^2 p(\mathbf{r},t)}{\partial t^2} = \frac{p_{i-1}^n - 2p_i^n + p_{i+1}^n}{(\Delta x)^2} \tag{B.3}$$

$$\frac{\partial H(\mathbf{r},t)}{\partial t} = \frac{H_i^{n+1} - H_i^n}{\Delta t_a} \tag{B.4}$$

where $H_i^n = \eta_{th}\mu_a(z)\phi(z,t)|_{z=i\Delta x, t=n\Delta t_a}$ is known. This gives an update equation of the form

$$\begin{aligned} p_i^{n+1} =& 2p_i^n - p_i^{n-1} \\ &+ v_s^2(\Delta t_a)^2\left(\frac{\beta}{C_P}\frac{H_i^{n+1} - H_i^n}{\Delta t_a} + \frac{p_{i-1}^n - 2p_i^n + p_{i+1}^n}{(\Delta x)^2}\right) \end{aligned} \tag{B.5}$$

The resulting pressure field is then converted to a refractive index profile following the elasto-optic effect. This is then used in a 1D electromagnetic FDTD simulation with a plane wave. Here for simplicity it is assumed that there are no current sources and that all materials are non-magnetic such that the relative permeability is $\mu_r = 1$. This leave a homogeneous wave equation of the form $E_{xx}(\mathbf{r},t) - (1/c^2)E_{tt}(\mathbf{r},t) = 0$ which yields an update equation of the form

$$E_i^{m+1} = 2E_i^m - E_i^{m-1} + \left(\frac{c_i^m \Delta t_o}{\Delta x}\right)^2 (p_{i-1}^m - 2p_i^m + p_{i+1}^m) \tag{B.6}$$

where $c_i^m = c/n(z,t)|_{z=i\Delta x, t=m\Delta t_o}$ is the local speed of optical propagation. Two plane waves are sent such that $E_1^m = E_0\cos(2\pi\nu m\Delta t_o)$ with one wave subject to the full index profile and the other subject to a continuous medium. The two waves can then be subtracted from each other with any remaining signal being a result of reflection from the interface. After all significant interactions with the interface have occurred, then the maximum

value is used to determine the intensity reflectivity for the given wavelength and acoustic time such that $R(t, \nu) = \max\{|E_1^{end}/E_0|^2\}$.

Appendix C

The Multi-layer Optical Scattering Model

computational method [111]

The scattering coefficients are now defined through a recursive algorithm presented in [131]

$$a_n = a_n^{L+1} = \frac{[H_n^a(m_L x_L)/m_L + n/x_L]\psi_n(x_L) - \psi_{n-1}(x_L)}{[H_n^a(m_L x_L)/m_L + n/x_L]\zeta_n(x_L) - \zeta_{n-1}(x_L)} \tag{C.1a}$$

$$b_n = b_n^{L+1} = \frac{[m_L H_n^b(m_L x_L) + n/x_L]\psi_n(x_L) - \psi_{n-1}(x_L)}{[m_L H_n^b(m_L x_L) + n/x_L]\zeta_n(x_L) - \zeta_{n-1}(x_L)} \tag{C.1b}$$

Where the determinants H_n^a and H_n^b are defined as

$$H_n^a(m_1 x_1) = D_n^{(1)}(m_1 x_1) \tag{C.2a}$$

$$H_n^a(m_\ell x_\ell) = \frac{G_2^a D_n^{(1)}(m_\ell x_\ell) - Q_n^{(\ell)} G_1^a D_n^{(3)}(m_\ell x_\ell)}{G_2^a - Q_n^{(\ell)} G_1^a} \; ; \; \ell = 2, ..., L \tag{C.2b}$$

$$H_n^b(m_1 x_1) = D_n^{(1)}(m_1 x_1) \tag{C.3a}$$

$$H_n^b(m_\ell x_\ell) = \frac{G_2^b D_n^{(1)}(m_\ell x_\ell) - Q_n^{(\ell)} G_1^b D_n^{(3)}(m_\ell x_\ell)}{G_2^b - Q_n^{(\ell)} G_1^b} \; ; \; \ell = 2, ..., L \tag{C.3b}$$

and

$$D_n^{(1)}(z) = \psi_n'(z)/\psi_n(z) \tag{C.4}$$

$$D_n^{(3)}(z) = \zeta_n'(z)/\zeta_n(z) \tag{C.5}$$

$$Q_n^{(\ell)} = \left(\frac{\psi_n(m_\ell x_{\ell-1})}{\zeta_n(m_\ell x_{\ell-1})}\right)\left(\frac{\psi_n(m_\ell x_\ell)}{\zeta_n(m_\ell x_\ell)}\right)^{-1} \tag{C.6}$$

$$G_1^a = m_\ell H_n^a(m_{\ell-1} x_{\ell-1}) - m_{\ell-1} D_n^{(1)}(m_\ell x_{\ell-1}) \tag{C.7a}$$

$$G_2^a = m_\ell H_n^a(m_{\ell-1} x_{\ell-1}) - m_{\ell-1} D_n^{(3)}(m_\ell x_{\ell-1}) \tag{C.7b}$$

$$G_1^b = m_{\ell-1} H_n^b(m_{\ell-1} x_{\ell-1}) - m_\ell D_n^{(1)}(m_\ell x_{\ell-1}) \tag{C.8a}$$

$$G_2^b = m_{\ell-1} H_n^b(m_{\ell-1} x_{\ell-1}) - m_\ell D_n^{(3)}(m_\ell x_{\ell-1}) \tag{C.8b}$$

However, direct computation of these terms is challenging due to numerical stability surrounding components approaching poles and zeros. Several efforts have provided reasonably stable algorithms. Computation of the logarithmic derivatives of the Riccati-Bessel functions were previously discovered for $D_n^{(1)}$ [110] and $D_n^{(3)}$ [108]. For $D_n^{(1)}$ a downward recurence is used following

$$D^{(1)}_{N_{max}}(z) = 0 + i0 \tag{C.9a}$$

$$D^{(1)}_{n-1}(z) = \frac{n}{z} - \frac{1}{D^{(1)}_n(z) + n/z} \; ; \; n = N_{max}, ..., 1 \tag{C.9b}$$

Where the total number of terms N_{max} is appropriately selected in terms of the size parameter as $\max(N_{stop}, |m_\ell e_\ell|, |m_\ell x_{\ell-1}|) + 15$; $\ell = 1, ..., L$ where N_{stop} is found as

$$N_{stop} = \begin{cases} x_L + 4x_L^{1/3} + 1, & 0.02 \leq x_L < 8 \\ x_L + 4.05x_L^{1/3} + 2, & 8 \leq x_L < 4200 \\ x_L + 4x_L^{1/3} + 2, & 4200 \leq x_L < 20000 \end{cases} \tag{C.10}$$

$D^{(3)}_n(z)$ can be found through

$$\psi_0(z)\zeta_0(z) = \frac{1}{2}\left[1 - (\cos 2\mathrm{Re}\{z\} + i \sin 2\mathrm{Re}\{z\}) \exp(-2\mathrm{Im}\{z\})\right] \tag{C.11a}$$

$$D^{(3)}_0(z) = i \tag{C.11b}$$

$$\psi_n(z)\zeta_n(z) = \psi_{n-1}(z)\zeta_{n-1}(z)\left[\frac{n}{z} - D^{(1)}_{n-1}(z)\right]\left[\frac{n}{z} - D^{(3)}_{n-1}(z)\right] \tag{C.12a}$$

$$D^{(3)}_n(z) = D^{(1)}_n(z) + \frac{i}{\psi_n(z)\zeta_n(z)} \; ; \; n = 1, ..., N_{max} \tag{C.12b}$$

The $Q^{(\ell)}_n$ ratio can be calculated through [131]

$$Q^{(\ell)}_0 = \exp(-2[b_2 - b_1]) \frac{\exp(-i2a_1) - \exp(-2b_1)}{\exp(-i2a_2) - \exp(-2b_2)} \tag{C.13a}$$

$$Q^{(\ell)}_n = Q^{(1)}_{n-1}\left(\frac{x_{\ell-1}}{x_\ell}\right)^2 \frac{[z_2 D^{(1)}_n(z_2) + n]}{[z_1 D^{(1)}_n(z_1) + n]} \frac{[n - z_2 D^{(3)}_{n-1}(z_2)]}{[n - z_1 D^{(3)}_{n-1}(z_1)]} \; ; \tag{C.13b}$$

$$n = 1, ..., N_{max}$$

where $z_1 = m_\ell x_{\ell-1} = a_1 + ib_1$ and $z_2 = m_\ell x_\ell = a_2 + ib_2$.